Technical University of Munich

Department of Physics

–

Chair of Molecular Nanoscience &
Chemical Physics of Interfaces (E20)

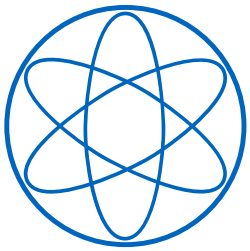

Bonding, Reactivity and Chemical Transformations of Adsorbed Organic and Metal-Organic Species

Dissertation

Peter Sebastian Deimel

Technische Universität München

Physik-Department

–

Lehrstuhl für Molekulare Nanowissenschaften &
Chemische Physik von Grenzflächen (E20)

Bonding, Reactivity and Chemical Transformations of Adsorbed Organic and Metal-Organic Species

Peter Sebastian Deimel

Vollständiger Abdruck der von der Fakultät für Physik der Technischen Universität München zur Erlangung des akademischen Grades eines

Doktors der Naturwissenschaften (Dr. rer. nat.)

genehmigten Dissertation.

Vorsitzender:		Prof. Dr. Martin Zacharias
Prüfer der Dissertation:	1.	Prof. Dr. Johannes V. Barth
	2.	Prof. Dr. Ulrich K. Heiz

Die Dissertation wurde am 20.02.2019 bei der Technischen Universität München eingereicht und durch die Fakultät für Physik am 10.05.2019 angenommen.

Abstract

In the presented work, by means of state-of-the-art surface science investigations in ultra-high vacuum, prototypical organic and metal-organic species are adsorbed on well-defined single-crystal metal supports and their structural and electronic properties are characterized at the sub-molecular level. In all considered cases, the influence that the supporting metal substrates exert on the adsorbed molecular species reflect the wealth of physical and chemical interfacial phenomena and stress the significance of such investigations for the fields of heterogeneous catalysis, the bottom-up synthesis of nano-scaled surface-supported structures and the functionalization of surfaces.

Specifically, for the two technologically relevant phenol derivatives Bisphenol A and Diethylstilbestrol, the Cu(111) surface acts as template promoting a highly selective, surface-assisted covalent coupling reaction. The combination of X-ray photoelectron spectroscopy (XPS), temperature-programmed desorption (TPD) and scanning tunneling microscopy measurements reveals a three-step chemical transformation from monomers to disordered networks of branched polymers and confirms both the directing role of the hydroxyl group as well as the active role of the metal substrate.

In addition, for the metal-organic complex iron phthalocyanine (FePc) X-ray standing wave experiments supported by theoretical calculations indicate that a Ag(111) substrate can behave in a similar way as a molecular ligand, *via* redistribution of charge along the molecule-to-substrate bond. In particular, the coordination of water or ammonia to the iron center of FePc, in trans-position to the silver surface, distinctly increases the adsorption height of the central Fe atom. This structural manifestation of the "surface *trans*-effect" reflects that the coordination to incoming ligands can be influenced by and at the same time modify the bonding of the metal-organic complex to the surface.

Moreover, *via* exposure to ultraviolet light, two intrinsically different surfaces, namely Ag(111) and rutile TiO_2(110), are activated to trigger chemical reactions. Specifically, in the case of Ag(111) the light-stimulated dehalogenation of adsorbed brominated precursors is observed, while on TiO_2(110) the adsorbed glycine undergoes photodissociation and -desorption. The two proof-of-concept studies demonstrate the applicability of a custom-designed light source devised within this work.

Eventually, with the aim of suppressing and controlling the strong influence of the supporting metal substrate on molecular adsorbates observed in the aforementioned studies, a self-assembled monolayer (SAM) of 4-fluorothiophenol (4-FTP) is introduced as molecular spacer layer between metal-organic complexes (FePc and ruthenium tetraphenylporphyrin) and the underlying Ag(111) support. Here, the combination of XPS, TPD and low-energy electron diffraction measurements reveals the thermal evolution of the organic/SAM/metal-stacking. At low temperatures, the 4-FTP SAM serves to decouple both electronically and physically the molecular layer from the underlying metal support, whereas upon annealing SAM constituents are displaced from the surface by the metal-organic complexes, resulting in an inverted layer stacking.

Zusammenfassung

In der vorliegenden Arbeit werden mittels experimenteller Methoden der Oberflächenphysik im Ultrahochvakuum verschiedene organische und metallorganische Adsorbate auf einkristallinen Metalloberflächen untersucht. Die Metalloberfläche erfüllt hierbei für die adsorbierten Moleküle und die betrachteten Systeme ganz unterschiedliche Funktionen. Die sich in den vorgestellten Experimenten wiederspiegelnde Fülle an physikalischen und chemischen Phänomenen auf Oberflächen und an Grenzflächen betont dabei die Bedeutung der Oberflächenphysik für z.B. die heterogene Katalyse, die Bottom-up-Synthese von Nanostrukturen und die Funktionalisierung von Oberflächen.

In der ersten Untersuchung bildet die Cu(111)-Oberfläche die Unterlage für die selektive, oberflächengestützte Bildung einer kovalenten C-C Bindung zwischen Monomeren der technologisch relevanten Phenolderivate Bisphenol A (BPA) und Diethylstilbestrol (DES). Mittels Kombination von Röntgenphotoelektronenspektroskopie (XPS), Temperatur-programmierter Desorption (TPD) und Rastertunnelmikroskopie wird dabei sowohl für BPA als auch für DES die dreistufige chemische Umsetzung der Monomere zu ungeordneten, verzweigten Polymeren nachverfolgt. Hierbei bestätigt sich, dass sowohl die dirigierende Funktion der Hydroxylgruppen als auch die aktive Rolle des Metallsubstrates für die beobachtete Umwandlung ausschlaggebende Faktoren sind.

In der nächsten Untersuchung zeigen XSW-Messungen (engl.: “X-ray standing waves”) am metallorganischen Komplex Eisen(II)-Phthalocyanin (FePc), gestützt auf theoretische Berechnungen, dass sich die Ag(111)-Oberfläche ähnlich einem Liganden verhält. Insbesondere verursacht die Koordination von H_2O und NH_3 an das zentral koordinierte Eisen-Ion, *trans*-ständig zum Trägermedium Ag(111), eine Zunahme des Abstandes zwischen letzterem und dem Eisen-Ion. Die sich hierbei manifestierenden strukturellen Auswirkungen, die dem “surface *trans*-effect” zugeschrieben werden, legen nahe, dass sich sowohl die Bindung eines Liganden an das zentral koordinierte Metall-Ion, als auch die Bindung zwischen dem metallorganischen Komplex und der Metalloberfläche, wechselseitig beeinflussen. Insbesondere übt die Ag(111)-Oberfläche damit direkt Einfluss auf die chemischen Eigenschaften des darauf adsorbierten Metallkomplexes aus.

In einer anderen Untersuchung wird durch Beleuchtung mit ultraviolettem Licht in zwei “Proof of Concept” Experimenten sowohl die Ag(111)- als auch die TiO_2(110)-Oberfläche (Rutil) elektronisch angeregt. Im Falle von Ag(111) wird dabei mittels XPS eine lichtinduzierte Dehalogenierung des auf der Oberfläche adsorbierten, bromierten Precursor-Moleküls beobachtet. Auf der TiO_2-Oberfläche adsorbiertes Glycin hingegen desorbiert bei Beleuchtung mit ultraviolettem Licht in Bruchstücken von der Oberfläche. Die beiden Experimente bestätigen damit die Praxistauglichkeit der in dieser Arbeit entworfenen LED-basierten Lichtquelle und motivieren weitere Untersuchungen.

In Anbetracht des starken Einflusses der Metalloberflächen auf die Adsorbate wird in einer weiteren Untersuchung, mit dem Ziel der Entkoppelung zweier metallorganischer Komplexe (FePc und Ruthenium-Tetraphenylporphyrin) von der Ag(111)-Oberfläche, eine auf

letzterer aufgebrachte selbstorganisierende Monoschicht (SAM) aus 4-Fluorothiophenol (4-FTP) als molekulare Deckschicht eingesetzt. Mittels Kombination aus XPS, TPD und der Beugung niederenergetischer Elektronen an Oberflächen (LEED) wird die temperaturabhängige Entwicklung des Metallkomplex/SAM/Ag(111)-Schichtaufbaus nachvollzogen. Bei niedrigen Temperaturen ist die Entkoppelung der Komplexe von der Oberfläche möglich. Mit zunehmender Temperatur bricht der Schichtaufbau jedoch zusammen, wobei die Metallkomplexe die SAM von der Oberfläche verdrängen und sich der Schichtaufbau zwischen Metallkomplexen und SAM umkehrt.

Contents

List of Figures

List of Tables

1 Introduction

Surface science aims at the fundamental understanding of chemical and physical phenomena occurring at surfaces and interfaces. To obtain such insight, very often a drastic simplification of the investigated systems as well as the ultimate control of their structure and composition is required. To this end, surface science investigations are commonly performed in an ultra-high vacuum (UHV) environment under model conditions. Although this approach inherently complicates a direct linking to many complex "real-world" systems, it is principally this strategy of reducing the complexity of real systems into elementary representations that enables to gain a comprehensive understanding of their physical and chemical behaviour at the atomic or molecular level. The denomination "surface science" may, however, appear imprecise and vague to a non-specialist person, partly related to the fact that surface science itself is an extremely broad, far-reaching and interdisciplinary field and that surfaces are ubiquitous in nature as well as in technology. Thus, to obtain a clearer perception of what this field of science does actually imply, to delineate the opportunities and prospects for surface scientists and also, more specifically, to motivate the present work, one should start by answering the following questions:

Why is it important to understand surfaces and where do they matter?

A first exemplary answer is offered by life sciences. When it comes to issues of biocompatibility, of biological response to a material, of synthesis of complex biological surfaces, tissue engineering, molecular- and bio recognition, and, more fundamentally, when one aims to understand how key biological reactions take place and can be described, it is mostly interfaces and surfaces that play the central role and are the scene of action [1, 2]. Even more, the formation of structure and function in biology itself requires the confinement by functionalized boundary layers, which, in the most banal case, allow the build-up of the electrochemical gradients that enable life [3]. In the context of biomimetics and bio(medical) surface science [1, 2], it is thus the characterization as well as the functional reproduction of these highly specialized and precisely functioning biological surfaces, devised by nature, that represents both an exciting challenge and a key field for expanding the classical surface science, with a potentially tremendous impact in pharmacology and medicine, just to mention biosensors, medical implants and templates for tissue growth. The controlled fabrication of novel bioengineered surfaces could, e.g., be achieved in a bottom-up approach by self-assembly [4]. In this case, self-assembled monolayers (SAMs) of deliberately tailored organic compounds could allow to endow surfaces

with well-defined chemical and structural properties, a method that is referred to as "surface functionalization". From the point of view of the classical UHV-based surface science approach, however, the major difficulties here lie in the complex 3D topographies, the role of the aqueous environment (hydration) and the dynamic properties that are, altogether, essential for the bio-specific functioning in biological environments [1], demanding for purposeful and systematic investigation under simplified conditions. As an introductory step, in chapter 6 of this work a simple self-assembled monolayer is used as spatial decoupling layer between prototypical, bio-inspired metal-organic complexes and the subjacent metal single crystal, providing important insights on the structure, stability and "permeability" of such a layered system under UHV conditions.

Secondly, an industrially important field that demands for a comprehensive understanding of the physical and chemical properties of surfaces is heterogeneous catalysis. Here, recent publications show that the systematic exploration of factors that decisively influence catalytic properties, particularly the atomic structure and surface composition, by means of a surface science approach offers enormous potential to devise and improve novel catalysts [5–9]. In addition, the desire to approach realistic catalytic conditions also comes along with continuous advances in instrumentation, which led for instance to the development of (near-)ambient pressure X-ray photoelectron spectroscopy [6, 10–12] and high-pressure scanning tunneling microscopy [10, 12]; this emphasizes the relevance of classical surface science techniques for *operando* detection of intermediate species during catalytic reactions. In the context of heterogeneous catalysis, notably the field of photocatalysis appears highly appealing to current research, motivated by the abundance of sunlight that can be exploited to drive chemical conversions. An example for this are promising studies on the photo-induced water-splitting capability of metal-organic compounds [13–15], which boost efforts directed to further reveal and verify the underlying processes by means of surface science techniques. Along this line, in the present work a UHV-compatible LED-based re-entrant light source was devised (c.f. section 3.3), with the aim of providing our UHV-setup with high intensity visible and ultraviolet light. The successful application of this device is verified by two proof-of-concept experiments in chapter 7.

Another topical field of surface science aims to elucidate processes intervening in the surface-supported bottom-up synthesis of novel low-dimensional architectures from simple molecular precursors, exploiting the self-assembly and hierarchical organization of suitable organic building blocks, as well as the structural and catalytic properties of the supporting substrates. The obtained synthesis routes for nano-scaled structures hold promise for application in future nano devices. One example is given by the highly flexible graphdiyne nanowires reported by Klappenberger et al. [16], in principle allowing to store data at an unprecedented storage density and thermal stability by means of *cis-trans* switching of molecular *sub*-units along nanowires adsorbed on a metal support. A second example is the surface-confined, atomically precise formation of graphene nanoribbons, which

have already been successfully implemented in nanoscale field-effect transistors [17, 18]. Specifically, these two special examples emphasize that the surface-assisted bottom-up approach can be a promising strategy to promote the downsizing of electronic devices and sensors. In this context, a successful mechanism to covalently link molecular precursors in a highly selective manner is the so-called surface-assisted Ullmann coupling [19]. However, the latter is prone to leave halogen byproducts coadsorbed on the surface. In the search of alternatives, the hydroxy-directed C-C coupling was first reported by Li et al. [20], and here it will be explored in detail in chapter 4 of this thesis, whereby we will demonstrate the occurrence of a characteristic pattern of sequential reactions for two prototypical phenol derivatives.

With respect to the above-stated questions, and as already reflected in the examples of heterogeneous catalysis and the surface-supported bottom-up synthesis of nanoscale architectures, solid surfaces still offer a wealth of yet unexplored, and often unexpected chemical phenomena and reaction pathways for adsorbed species, which may be new to traditional, and especially solution based chemistry. One example is the "surface *trans*-effect" [21, 22], the structural implications of which are investigated in chapter 5 of the present work. The elucidation of such novel or unprecedented phenomena often opens up new perspectives for applications, improves the fundamental understanding of surfaces and stimulates implementation in devices.

Thus, motivated by the examples and fields of research mentioned above, and in the framework of UHV-based surface science, this thesis embodies relevant examples of the very different roles that a surface can play for molecular adsorbates. In chapter 4, a Cu(111) surface acts as template for promoting a highly selective, surface-assisted hydroxy-directed covalent coupling reaction. Here the nature of the support plays a decisive role in the sequential reaction steps [20]. A multi-technique approach provides detailed information regarding the chemical and structural evolution of the adsorbed phenol derivatives (Bisphenol A and Diethylstilbestrol) to branched molecular chains. Furthermore, in chapter 5 X-ray standing wave experiments supported by theoretical calculations demonstrate that a Ag(111) surface behaves in a similar way as a molecular ligand with respect to adsorbed metal-organic complexes. In particular, the coordination of small molecular adducts such as water or ammonia to the metal center of the metal complex (here: iron phthalocyanine), in *trans*-position to the surface, can be influenced by, and at the same time modify, the bonding of the metal-organic complex to the surface. This specific case thus exemplifies how the metal surface can influence the electronic and chemical properties of adsorbate species, which should not be neglected in the development of real devices. For example, the metal support can have a substantial effect on the reactivity of adsorbed species [23] and the photoexcitation of adsorbate molecules can be heavily affected or even quenched by the substrate. In the attempt to "turn off" this often detrimental influence of the metal substrate, in chapter 6 a self-assembled monolayer of 4-fluorothiophenol is introduced as spatial decoupling layer between pro-

totypical metal-organic complexes (iron phthalocyanine and ruthenium tetraphenylporphyrin) and the Ag(111) support, and the structural, chemical and thermal evolution of the organic/SAM/metal-stacking is investigated. Specifically, in the already considered context of biomimetics it is envisaged that such self-assembled monolayers should not merely be regarded to act as inert supports, promoting the decoupling of the metal-organic complexes from the substrate, but instead, could also be functionalized for the design of biologically relevant surfaces [2]. Finally, *via* exposure to UV light in chapter 7, two intrinsically different surfaces, Ag(111) and rutile TiO_2(110), are electronically activated, triggering chemical reactions like the dehalogenation of a brominated precursor (on Ag(111)) or even the removal of the adsorbed molecular species (glycine on TiO_2(110)), and demonstrating the applicability of the home-built LED-based light source which is described in section 3.3.

The presentation of the experimental studies (chapters 4 to 7) is preceded by a concise introduction to the employed experimental techniques and methodology (chapters 2 and 3) and concluded by a brief summary and outlook (chapter 8).

2 Experimental Methods

In this chapter, the fundamental principles and the theoretical background of the experimental techniques employed in this work are described. X-ray photoelectron spectroscopy (XPS) allows for an element-specific investigation of the chemical state of the considered organic and metal-organic adsorbates and surfaces and, in the form of temperature-programmed XPS (TP-XPS), it is utilized to reveal thermally triggered chemical transformations. Latter can result from surface-assisted chemical reactions, the desorption of molecular species and fragments, or changes in adsorbate morphology. Especially in combination with TP-XPS, temperature-programmed desorption (TPD), which allows monitoring the desorption of adsorbate species, their fragments and reaction products, is a powerful tool to unravel chemical reactions taking place on surfaces. Furthermore, low-energy electron diffraction (LEED) is used to reveal the self assembly and long-range ordering of the deposited molecules, as well as corresponding transformations in adsorbate structure, and to assess the quality of the single-crystal supports. Finally, the synchrotron-based normal incidence X-ray standing waves (NIXSW) technique provides an elegant way to determine the height of adsorbate atoms above the respective single-crystal surface. All of the applied experimental techniques rely on the detection of either electrons or smallest amounts of desorbing molecular species and thus require an ultra-high vacuum (UHV) environment.

2.1 Ultra-High Vacuum and Surface Science

Surface science aims at the fundamental understanding on the atomic level of physical and chemical phenomena that take place on surfaces, and thus, is of paramount importance in various fields of science and technology. For instance, as many studies show [9, 24–26], novel heterogeneous catalysts may even be devised in a surface-science approach by revealing the role of their atomic structure. In the same manner, atomic-scale studies on molecular adsorbates on surfaces, revealing their fundamental physical and chemical properties in the adsorbed state, as well as possible surface supported chemical transformations, are highly relevant, both for the creation of functional systems by self-assembly [27] and the discovery of formerly unknown surface-supported reaction pathways. However, such investigations require the probed system to be entirely pure and free of contaminants, which can only be achieved in an ultra-high vacuum (UHV) environment. In this regard, using the kinetic theory of gases and the Hertz-Knudsen equation, we need to consider

the flux F of molecules impinging on a surface (Ref. [28], page 19):

$$F = \frac{p}{\sqrt{2\pi m k_B T}} \ . \tag{2.1}$$

Here, p is the pressure, m the mass of the molecule, k_B the Boltzmann constant and T the temperature. Considering a UHV system at a pressure of 1×10^{-9} mbar, latter of which shall be entirely due to the major residual gas CO, and a temperature of 300 K, each surface will be subject to a corresponding molecular flux of $\sim 3 \times 10^{11}\,\mathrm{s^{-1}\,cm^{-2}}$. Assuming that each CO molecule that hits the surface will stay adsorbed (i.e., implying a sticking coefficient of unity), and a surface atom density of $1 \times 10^{15}\,\mathrm{cm^{-2}}$, it will take roughly 60 min until the number of adsorbed molecules equals the number of atoms in the first atomic layer of the surface. In this case, one monolayer of CO is adsorbed. In practice, as controlled experimental conditions require the investigated systems to stay clean for the entire period of the performed measurements, pressures far below 1×10^{-9} mbar are highly desired. This becomes particularly important when dealing with reactive species and surfaces and cryogenic sample temperatures, as in these cases the sticking probability for residual gas species is maximized. In the context of surface science and UHV, a unit of the gas exposure to a surface is introduced (Ref. [29], page 30): 1 langmuir (1 L) corresponds to an exposure of 1.33×10^{-6} mbar for 1 s. Again considering Eq. (2.1) for CO and a surface atom density of $1 \times 10^{15}\,\mathrm{cm^{-2}}$, an exposure of 1 L implies that a number of CO molecules as high as 40 % of the number of surface atoms have impinged on the surface.

In addition, beside keeping the system free of contaminants, UHV is also technical prerequisite for experimental methods that rely on the detection of electrons. In fact, as electrons strongly interact with matter, a large residual gas pressure in the experimental chamber can effectively prevent them from reaching the electron detector.

2.2 X-ray Photoelectron Spectroscopy

Through the detection of photoemitted electrons, X-ray photoelectron spectroscopy (XPS) provides insight into the electronic, stoichiometric and chemical properties of surfaces and adsorbate overlayers on surfaces.

2.2.1 Physical Principles

According to the photoelectric effect, which was first explained by A. Einstein in 1905 [30], the absorption of a photon can provide an electron with enough energy to leave matter. The kinetic energy E_{kin} of the photoemitted electron is then given by the following relation (Ref. [31], page 268):

$$E_{kin} = h\nu - E_b^F - \Phi_{det} \ . \tag{2.2}$$

Here, $h\nu$ is the incident photon energy, E_b^F is the binding energy of the electron with respect to the Fermi level and Φ_{det} is the work function of the electron detector. With the work function of the detector and the exciting photon energy fixed, detection of E_{kin} by means of an electron analyzer gives direct access to the binding energy of the photoemitted electron. As each element features a unique set of electron binding energies, characteristic of the probed elemental species and with absolute peak positions indicative of its chemical environment, XPS allows for both the determination of elemental compositions and an in-depth chemical analysis. For this reason, XPS is also commonly referred to as electron spectroscopy for chemical analysis (ESCA).

Based on the detection of photoemitted electrons, however, the information gathered with XPS is limited by the inelastic mean free path (IMFP) of electrons in matter. For kinetic energies ranging from 10 to 1000 eV, the IMFP in metals varies between 3 and 20 Å [32]. As a consequence, XPS only probes the surface region, i.e. the first few atomic layers of a sample. Due to this inherent surface sensitivity, which can also be regarded as an advantage, XPS is the method of choice for the study of thin films, molecular adsorbates on surfaces and surface-supported reactions. Owing to the strong interaction of electrons with matter, a large number of inelastically scattered and secondary electrons will contribute a featureless background to the recorded XP spectra, and the element-specific core-level lines are superimposed onto this background.

Considering the direct experimental access to E_b^F *via* Eq. (2.2), several effects need to be taken into account which affect the binding energy of the detected photoelectrons and also determine the appearence and shape of the corresponding peaks in the XP spectrum. In this regard, one discriminates between initial- and final-state effects. An initial-state effect that strongly influences the measured binding energy is the so-called chemical shift: the exact binding energy of core-level electrons varies with the chemical environment of the considered atomic species. This comprises the nature of the chemical bonding, the bonding partners, the associated oxidation state and, eventually, defines the resulting net charge on the atom [33]. For example, an increase of the oxidation state implies the donation of valence electrons to a bonding partner. As a result, less electrons remain to shield the positively charged nucleus, and the associated increase in the Coulomb interaction between nucleus and inner electrons increases the respective core-level binding energies. In this context, an example for titanium going through different oxidation states, which has been monitored by XPS, is given by Duncan et al. [23].

Among the final-state effects, atomic and extra-atomic electron relaxation [33] characterize the relaxation of the electronic system immediately after core-hole creation upon photoemission. The energy gain within this relaxation generally leads to an increase in the kinetic energy of the photoemitted electrons, in turn lowering the measured binding energy. Furthermore, spin-orbit coupling between the remaining unpaired spin after core-hole creation and the orbital angular momentum leads to a splitting of core-level lines for orbital quantum numbers $l > 0$. The corresponding intensity ratio for the spin-orbit

split peaks is given by the ratio of the associated degeneracies [33]. In addition, multiplet splitting may occur if the spin of an upaired core-level electron remaining in the formerly closed shell interacts with unpaired electrons in the valence shell. Finally, upon photoemission, the outgoing electron may also promote electronically excited final states. In this case, both discrete satellite peaks and peak broadening towards higher binding energy can occur. For example, excitation of electrons into bound states below, or unbound states above the vacuum level, leads to so-called shake-up or shake-off satellites, respectively. In the case of metals, excitation of electron-hole pairs around the Fermi level may result in an asymmetry of core-level peaks towards higher binding energy, whereas the excitation of plasmons may result in a progression of equally spaced plasmon-loss satellites as shown in Ref. [34].

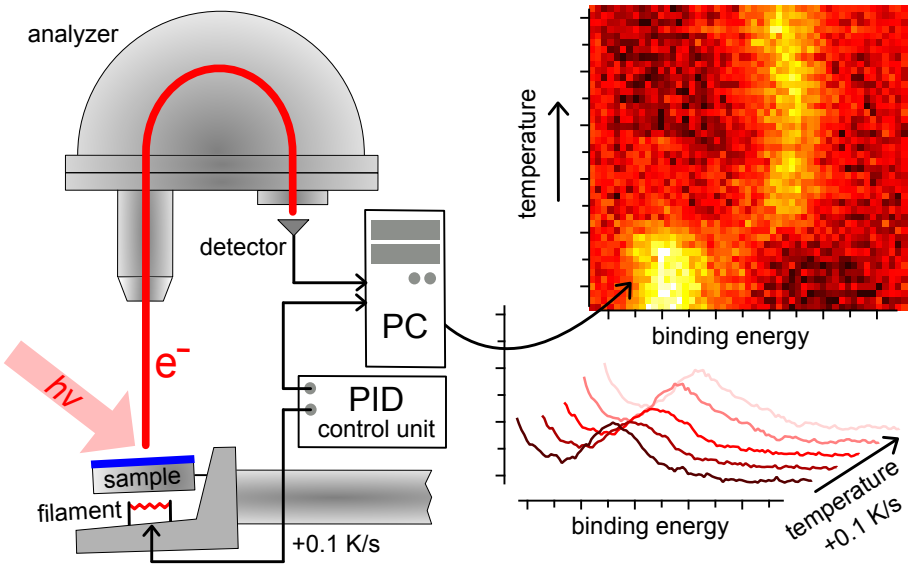

Figure 2.1: Schematic of the principle of temperature-programmed XPS (TP-XPS): recording XP spectra while the sample is heated at a constant rate allows to resolve temperature induced chemical changes of surfaces and adsorbate species (here: the blue-coloured film on the sample).

2.2.2 Temperature-Programmed XPS

Very often, chemical transformations and reactions on surfaces are triggered by increasing temperatures. While the standard XPS method is usually applied with the sample at a constant temperature, Fig. 2.1 shows how the technique can be upgraded in order to monitor the thermal evolution of a system. By means of a proportional-integral-derivative controller (PID controller) the investigated sample is heated at a constant heating rate

(e.g. 0.1 K/s). Simultaneously, subsequent XP-spectra are recorded and finally arranged in form of a two-dimensional colormap, providing direct access to temperature induced changes in binding energy. Limited by the intensity of the detected electrons, TP-XPS requires to find a compromise between a sufficiently slow heating-rate, a good signal intensity and acceptable energy resolution. The latter two factors can be controlled by the incoming X-ray intensity and the choice of analyzer slit-, pass energy- and lens mode settings.

2.3 Temperature-Programmed Desorption

The temperature-programmed desorption (TPD) method is a major tool to investigate the bonding interaction between adsorbates and the supporting surfaces, simply by monitoring desorption. In addition, utilizing the superior mass resolution of a quadrupole mass spectrometer, TPD is the technique of choice for identifying desorbing species and reaction products. Latter makes TPD a powerful technique to complement TP-XPS analyses, when investigating surface supported chemical modifications.

2.3.1 Physical Principles

According to the Polanyi-Wigner equation, the desorption rate dN/dt for an adsorbate species can be written as [35]

$$-\frac{dN}{dt} = \nu_d N^x exp(-\frac{E_d}{RT}) \ . \tag{2.3}$$

Here, ν_d is a pre-exponential frequency factor, N the surface concentration of the adsorbate, x the order of the desorption process, E_d the activation energy for desorption per mole of adsorbate, and R the ideal gas constant. The desorption rate depends exponentially on the temperature T, clearly becoming higher at increasing temperature. Note that the order of desorption, the pre-exponential factor and the activation energy can, in practice, depend on the surface concentration N, while at least the pre-exponential factor may, additionally, vary with temperature [36]. In the case of modern TPD experiments, the desorption rate dN/dt in Eq. (2.3) is measured by means of a quadrupole mass spectrometer that faces the probed sample at very short distance. Here, given a sufficient pumping speed and a sufficiently low heating ramp, the detected mass signal is a proportional measure for the desorption rate [35, 36]. Considering the nature of the desorption process itself, one usually distinguishes between first- and second-order desorption [37, 38]: second-order desorption ($x = 2$) implies desorption upon recombination (e.g., $H_{adsorbed} + H_{adsorbed} \rightarrow H_2$) and, thus, the desorption rate depends on the probability of adsorbed species coming close to each other; for the first-order or direct desorption ($x = 1$), the desorption rate is instead directly proportional to N. As a result, first- and

second-order processes may easily be distinguished by means of TPD experiments starting with different initial surface concentrations N_0. More precisely, following D. P. Woodruff and T. A. Delchar (Ref. [38], pages 363 to 364), the condition for the desorption peak maximum in the case of $x = 1$ is given by

$$\frac{E_d}{RT_{max}^2} = \nu_d \frac{dt}{dT} exp(-\frac{E_d}{RT_{max}}) \ , \tag{2.4}$$

whereas for $x = 2$ the following equation holds:

$$\frac{E_d}{RT_{max}^2} = N_0 \nu_d \frac{dt}{dT} exp(-\frac{E_d}{RT_{max}}) \ . \tag{2.5}$$

Note that dT/dt is the heating rate of the TPD experiment. From Eq. (2.4) and (2.5) it is evident that, for first-order desorption, T_{max} is independent of the surface concentration N, while for a second-order desorption process the maximum of desorption shifts to lower temperature with increasing N_0. However, this simple consideration does not take into account that, as already mentioned above, ν_d and E_d may also be dependent on N, and ν_d may additionally depend on T. Furthermore, desorption events can be correlated to, or can be a direct product of surface supported chemical reactions. An example are covalent coupling reactions like the cyclodehydrogenation of tetraphenylporphyrin derivatives [39], which is accompanied by the desorption of H_2. In this specific case, the desorption of H_2 clearly occurs *via* the recombination of hydrogen. Nevertheless, the desorption kinetics of this process may reflect the chemical reaction that leads to dehydrogenation, which, however, may not necessarily be of second order. In general, an unambiguous and correct determination of kinetic parameters from TPD experiments, even in the case of simple surface supported reactions, is far from trivial. An extensive overview and discussion, as well as an experimental test of the used experimental approaches and analysis methods to extract both kinetic parameters and the order of desorption from TPD spectra is provided by L. K. Ono and B. Roldan Cuenya in Ref. [40].

2.3.2 2D-TPD

TPD spectra may not be recorded for single mass-to-charge ratios (m/z) only, but, if mass resolution and signal intensity allow, for a whole mass range. An example of such a two-dimensional TPD (2D-TPD) spectrum is shown in Fig. 2.2. In this specific case, the species under investigation should have the molecular formula $C_9H_7NO_4$, with a total mass of 193 amu. However, the desorption spectrum recorded from a Ag(111) surface starts with the desorption of mass-to-charge ratio 149 (cf. feature 1 in Fig. 2.2), peaking at a temperature of ∼260 K. Only shortly after, peaking at a temperature around 320 K, a second molecular species desorbs, with its largest mass at 193 (cf. feature 3 in Fig. 2.2). This parent ion nicely corresponds to the singly ionized $C_9H_7NO_4$-species, whereas the

species of mass-to-charge ratio 149 can be identified as $C_8H_7NO_2$, a similar molecule with the -$COOH$ group replaced by -H, which can be a decay product of the former. Notably, as the supposed decay product leaves the surface at lower temperatures than the pristine $C_9H_7NO_4$-species, the TPD experiment suggests that the powder from which the molecule has been deposited onto the Ag(111) surface was contaminated with the undesired $C_8H_7NO_2$. As nicely illustrated by this example, recording 2D-TPD spectra

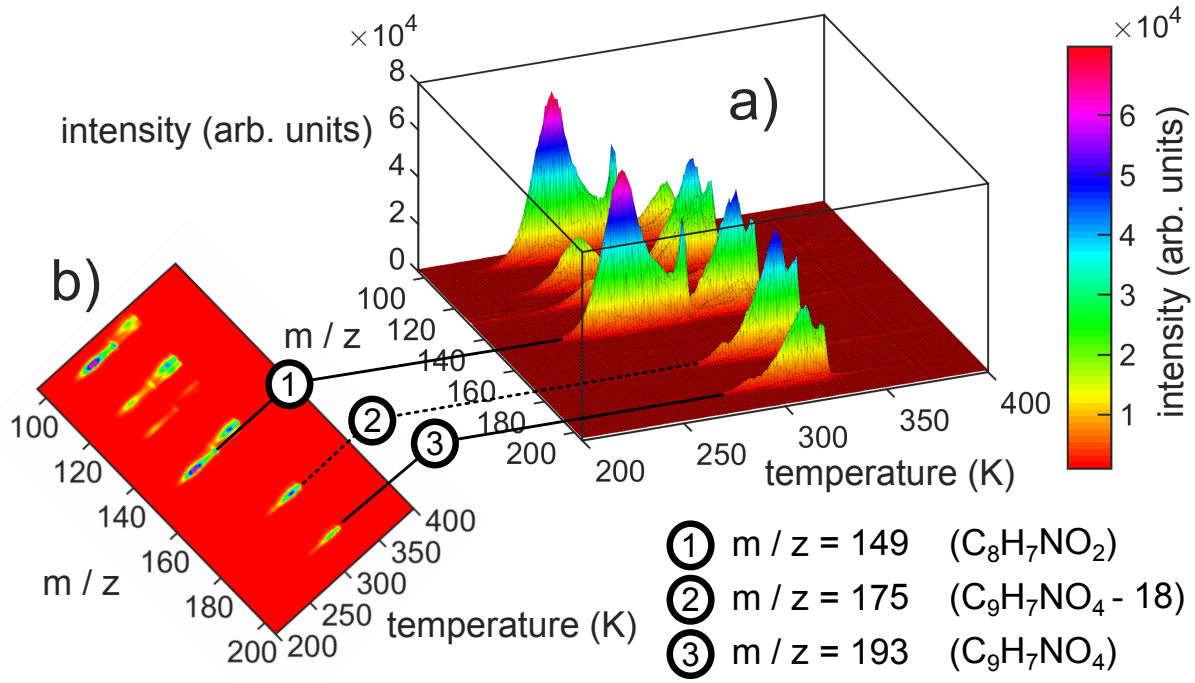

Figure 2.2: Experimental illustration of collecting TPD spectra in a two-dimensional fashion (2D-TPD): a) side- and b) topview of the two-dimensional colormap plot for a TPD experiment of $C_9H_7NO_4$ and $C_8H_7NO_2$ adsorbed on Ag(111). Features 1 and 3 are the identified parent ion masses of both $C_9H_7NO_4$ and $C_8H_7NO_2$, whereas feature 2 is a fragment of 3, likely corresponding to $C_9H_7NO_4$ minus one H_2O molecule of mass 18. The TPD experiment was performed at a heating rate of 0.5 K/s.

over the full range of accessible masses allows for the unambiguous identification of desorbing molecular species, especially because each species shows its singly ionized parent ion, followed by a characteristic fragmentation pattern towards lower masses. For identification, the fragmentation pattern can be compared to reference databases [41, 42]. In this regard, 2D-TPD is of particular use and provides a simple and fast means to assess the purity of investigated molecules.

2.4 Low-Energy Electron Diffraction

Low-energy electron diffraction (LEED) exploits the elastic scattering of electrons from two-dimensional periodic structures and, thus, is a standard tool to investigate the structure and to assess the quality of single-crystal surfaces, in particular, allowing to reveal periodic arrangements of adsorbate overlayers. As shown in Fig. 2.3a, by means of an electron gun, electrons are emitted and accelerated towards the probed sample. Meeting the Laue-condition for elastic scattering (Ref. [38], page 24)

$$\mathbf{k_f} - \mathbf{k_i} = \mathbf{G} \ , \tag{2.6}$$

with $\mathbf{k_i}$ and $\mathbf{k_f}$ the momentum vectors of incident and backscattered electrons, respectively, and $\mathbf{G}$ a reciprocal lattice vector, the backscattered electrons constructively interfere to form a periodic diffraction pattern which is monitored on a fluorescent screen. While Eq. (2.6) holds for generic particles (electrons, neutrons, photons, etc.), in the special case of LEED, due to the short inelastic mean free path of electrons, elastic backscattering occurs predominantly from the first few atomic layers of the sample. As a result, in a simplified picture, only the momentum parallel to the surface needs to be conserved to meet the Laue-condition, turning the reciprocal lattice points along the surface normal into reciprocal lattice rods [29, 37, 38]. The Laue-condition in Eq. (2.6) thus simplifies to

$$\mathbf{k_{f,\parallel}} - \mathbf{k_{i,\parallel}} = \mathbf{G_\parallel} \ . \tag{2.7}$$

In reality, however, scattering from the first few atomic layers will always superimpose a large intensity modulation on the lattice rods, which can be exploitded for structure analysis by recording LEED-IV curves [29, 37]. In the considered simplified case of scattering from the two-dimensional reciprocal lattice of the surface only, the cases under which the Laue-condition is fulfilled is illustrated by the construction of an Ewald sphere (or circle) in Fig. 2.3b. Having the incident momentum vector $\mathbf{k_i}$ pointing onto the origin of the reciprocal lattice, for each intersection between the circle of radius $|\mathbf{k_i}|$ around the origin of $\mathbf{k_i}$ (which gives all possible final vectors $\mathbf{k_f}$) and the reciprocal lattice rods, constructive interference occurs and a diffraction spot will appear. In a standard LEED experiment, as depicted in Fig. 2.3a and b, $\mathbf{k_i}$ impinges normal to the surface, with $\mathbf{k_{i,\parallel}}$ equal to 0, and, as a result, $\mathbf{k_{f,\parallel}}$ equal to $\mathbf{G_\parallel}$. The LEED pattern for a surface of hexagonal symmetry is shown schematically in Fig. 2.3c. Here, as $\mathbf{k_{f,\parallel}}$ equals $\mathbf{G_\parallel}$, the labelling of the diffraction spots follows the unit vectors of the reciprocal surface lattice. As an example, Fig. 2.3d shows the LEED pattern for terephthalic acid molecules on a Ag(111) surface at 90 K. At an incident electron energy of 100 eV, the hexagonal pattern of the Ag(111) support is nicely visible, with the $(0,0)$- and $(-1,0)$-spots enclosed in the red rectangles. Note that, as the sample is inclined by $\sim 7°$ in our experimental setup, the $(0,0)$ reflection does not appear in the center, but right to the electron gun. In general, the angle θ_{bs} under

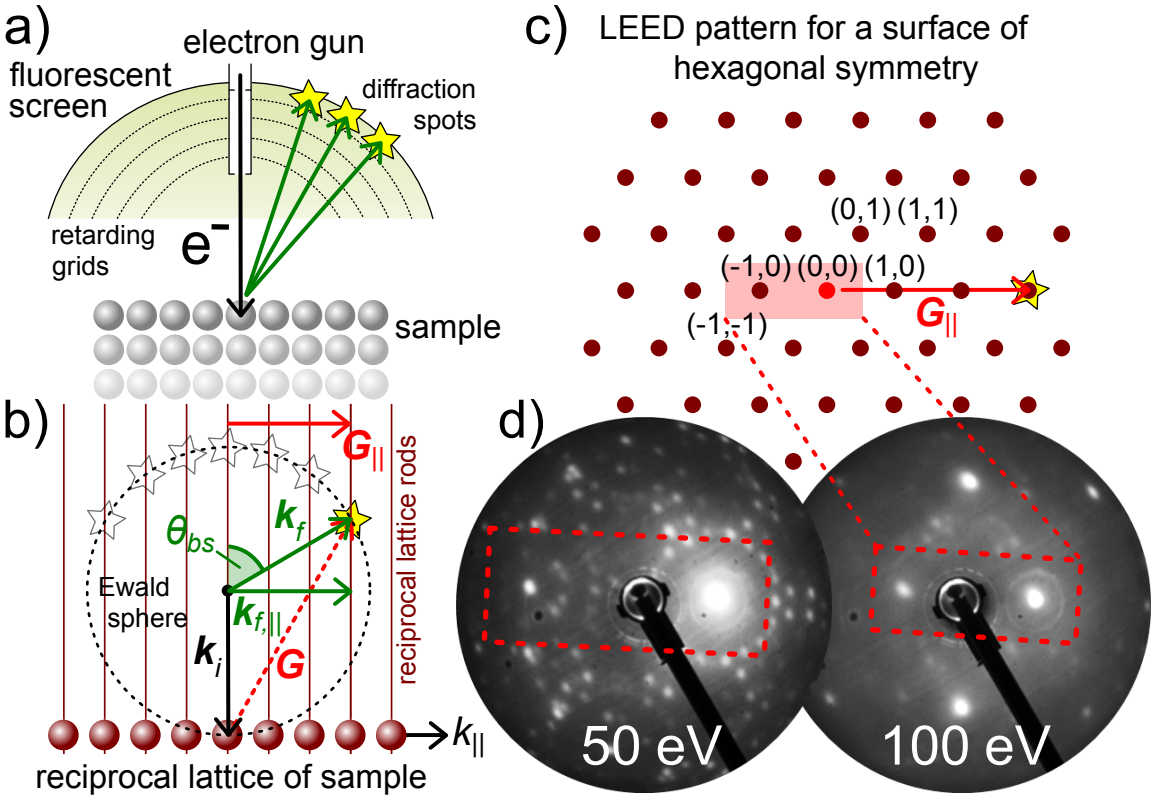

Figure 2.3: Schematics on the principle of low-energy electron diffraction (LEED): a) Simplified sketch of a LEED experiment in which electrons are accelerated towards a periodic sample and the elastically backscattered electrons are detected by means of a fluorescent screen. b) Illustration of the conditions for constructive interference from a two-dimensional lattice by construction of an Ewald sphere in reciprocal space. c) Exemplified LEED pattern for a two-dimensional system of hexagonal symmetry. d) LEED pattern for terephthalic acid on the close-packed Ag(111) surface at 90 K for incident electron energies of 50 eV and 100 eV, respectively.

which the backscattered electrons are detected on the fluorescent screen with respect to the surface normal is given by

$$sin(\theta_{bs}) = \frac{|\mathbf{k_f}_{,\parallel}|}{|\mathbf{k_f}|} \ . \tag{2.8}$$

As a decrease in the incident electron energy E also implies a decrease of the elastically scattered electron momentum $|\mathbf{k_f}|$, for a fixed $|\mathbf{k_f}_{,\parallel}|$ the scattering angle θ_{bs} will increase accordingly. Thus, following the decrease in electron energy in Fig. 2.3d, from 100 eV to 50 eV, the $(0,0)$- and $(-1,0)$-spots move away from each other. Furthermore, in the considered case of terephthalic acid on Ag(111), a set of additional spots starts to appear in between the hexagonal Ag(111) reciprocal space pattern, which is caused by the periodic overlayer of the molecules. The latter has larger unit cell dimensions as compared to the underlying Ag(111) lattice and, thus, shows more closely spaced spots in reciprocal space.

2.5 X-ray Standing Waves

The X-ray standing waves (XSW) technique [43, 44] is a synchrotron-based structural method that allows to study the adsorption structure of molecules on well-defined single crystal surfaces. Specifically, normal incidence X-ray standing waves (NIXSW) gives direct experimental access to the height of atomic species above the bulk terminated surface of a single crystal support.

2.5.1 Physical Principles

For a typical XSW measurement (cf. Fig. 2.4), the supporting single crystal is exposed to X-ray photons that fulfill the Bragg condition for specific lattice planes (i.e. the scatterer planes), leading to the generation of a standing wave field inside the crystal. The spatial positions of maximum field intensity of this standing wave are given by planes parallel to the corresponding scatterer planes, with periodicity equal to the scatterer-plane spacing d_{hkl}. Importantly, the standing wave reaches out the crystal and, by tuning the incident photon energy $h\nu$ (or the incident angle θ_i) across the region of maximum reflectivity, i.e. from situation (a) to (b) in Fig. 2.4, the phase of the standing wave is shifted by π. Latter implies a shift of the maximum field intensity by $d_{hkl}/2$ relative to the scatterer planes. Thus, when shifting the standing wave through the crystal, also the atoms of adsorbed species face a maximum or minimum field intensity – and thus a maximum or minimum of X-ray absorption – that is dependent on both the phase of the standing wave and their position relative to the extended scatterer planes. The X-ray absorption of the adsorbate atoms as a function of the incident photon energy (or the incident angle θ_i) can then be monitored by means of photoemission (cf. section 2.2), and the obtained absorption profiles in Fig. 2.4c bear information about the average position (coherent position, D)

and the distribution or disorder around that positon (coherent fraction, f_{coh}) relative to the scatterer planes.

2.5.2 Normal Incidence X-ray Standing Waves

In contrast to XSW experiments performed at inclinded photon incidence, in the case of incident X-rays impinging normal to the scatterer planes (cf. Fig. 2.4, NIXSW) the angular range in which maximum reflectivity occurs, i.e. the width of the the so-called Darwin- or reflectivity curve, becomes comparatively broad and, thus, less sensitive to the exact incidence angle [45]. The reason for this behavior can be illustrated by the expression for the width of the Darwin curve $\Delta\theta$ in terms of the incident angle θ_i as described by Woodruff et al. [45]:

$$\Delta\theta = \frac{2(|P|\Gamma\sqrt{F_H F_{\overline{H}}})}{sin(2\theta_i)} \ . \tag{2.9}$$

Here, P represents a polarization factor, F_H and $F_{\overline{H}}$ are geometrical structure factors for the considered Bragg reflection associated with the reciprocal lattice vectors $\mathbf{H}$ and $-\mathbf{H}$, θ_i is the incident angle of the photon beam with respect to the scatterer planes and Γ is a factor given by (cf. Ref. [45])

$$\Gamma = \frac{e^2\lambda^2}{4\pi^2\varepsilon_0 mVc^2} \ . \tag{2.10}$$

In the latter expression, e and m are the charge and electron mass, respectively, λ is the wavelength of the incident light, ε_o the vacuum permittivity, c the speed of light and V the unit cell volume. As becomes immediately clear from Eq. (2.9), for θ_i approaching 90°, the angular width $\Delta\theta$ of the Darwin curve becomes infinitely large, in reality approaching widths of up to 1° [45]. Accordingly, the requirements of the NIXSW technique on the quality of the crystal, the control of the incidence angle and the collimation and monochromaticity of the incident photon beam become less demanding and, thus, the standing wave measurements become feasible even for the usually less perfect metal single crystals [45]. However, note that, in the fixed normal incidence geometry of NIXSW, shifting the standing wave through the crystal can only be achieved by tuning the energy of the incident X-ray beam. Furthermore, in the special case of the scatterer planes matching the surface plane of the crystal, as shown in Fig. 2.4, the coherent position D becomes the physically meaningful average height above the bulk-terminated surface. Here, considering the computed absorption profiles in Fig. 2.4c which assume a coherent fraction f_{coh} of unity, the four different coherent positions from $0.25\,\mathrm{d_{hkl}}$ to $1\,\mathrm{d_{hkl}}$ are clearly distinguishable and, thus, allow for a qualitative estimate on the investigated system, even without further analysis. For quantitative analysis, the relative absorption profiles (I_{abs} vs. $\Delta h\nu$, the offset from the nominal Bragg condition) can be fitted according

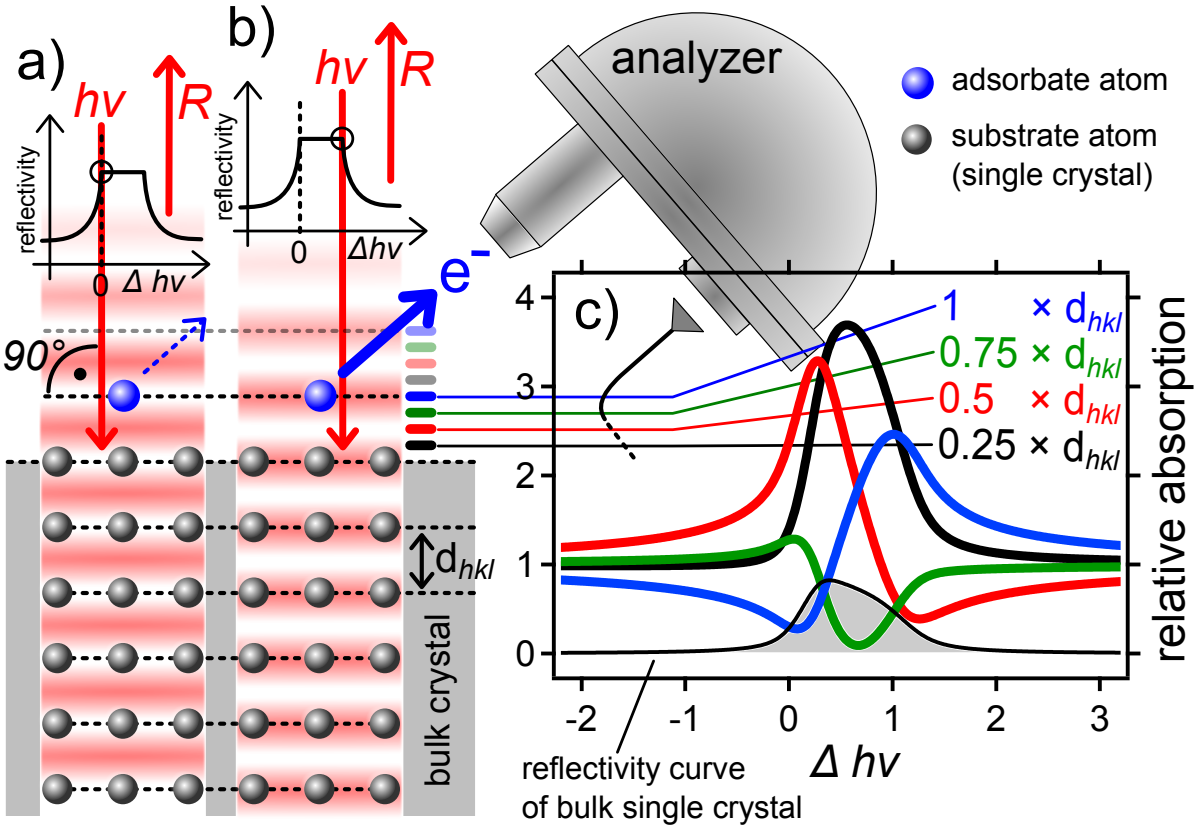

Figure 2.4: Schematic of the principle of the normal incidence X-ray standing waves method (NIXSW), inspired by illustrations in Refs. [44–46]: a) At the onset of the Darwin reflectivity curve, close to the nominal Bragg condition ($\Delta h\nu = 0$), the photon beam impinging at normal incidence ($\theta_i = 90°$) to the scatterer planes creates a standing wave field inside the crystal. In situation a), the planes of maximum field intensity are located in the midst of the neighboring scatterer planes (dashed lines within the bulk crystal, separated by d_{hkl}). b) Tuning the incident photon energy across the Darwin curve, to the opposite end of the region of maximum reflectivity, the maxima of the standing wave are shifted onto the scatterer planes by $d_{hkl}/2$. As the standing wave reaches out the crystal, adsorbate atoms (blue spheres) face maximum (b)) or minimum (a)) field intensity and, accordingly, show enhanced or weakened photoemission yield, depending on their height above the surface and the phase of the standing wave. c) As a result, while shifting the incident photon energy across the reflectivity curve of the single crystal, the relative absorption profile (I_{abs} vs. $\Delta h\nu$) measured by means of photoelectron spectroscopy directly reflects the height of adsorbate atoms above the next nearest scatterer plane.

to the equation [44]

$$I_{abs} = \left[1 + R\ C + 2\ f_{coh}\ \sqrt{R}\ \sqrt{C}\ cos\left(\Phi - \frac{2\pi D}{d_{hkl}}\right)\right]\ , \tag{2.11}$$

where C is defined as

$$C = \frac{1 + \frac{1}{2}\beta(3cos^2(\theta_p) - 1) + (\delta + \gamma cos^2(\theta_p))sin(\theta_p)cos(\phi)}{1 + \frac{1}{2}\beta(3cos^2(\theta_p) - 1) - (\delta + \gamma cos^2(\theta_p))sin(\theta_p)cos(\phi)}\ . \tag{2.12}$$

In Eq. (2.11), R is the measured reflectivity from the single crystal support (cf. Fig. 2.4c, bottom), f_{coh} the coherent fraction, Φ the phase difference between incident and reflected waves, d_{hkl} the spacing of the scatterer planes and D the coherent position. In addition, the term C, given by Eq. (2.12), accounts for non-dipole effects in the photoemission process as described in Ref. [47]. Latter depend on the experimental geometry, i.e. the angle ϕ between photon beam direction and the projection of the photoemission direction onto the plane perpendicular to the photon polarization, the angle θ_p between photoemission direction and photon polarization vector, as well as the core-level specific asymmetry factors β, γ and δ. For the evaluation of C, calculated asymmetry factors can be obtained from tables listed in Refs. [48, 49]. Finally, upon fitting the experimental absorption profiles (cf. Fig. 2.4c), the term D/d_{hkl} in Eq. (2.11) will only take values between 0 and 1. Accordingly, D/d_{hkl} provides the height above the next nearest scatterer plane in units of d_{hkl}, and to evaluate physically meaningful adsorption heights the atomic and molecular dimensions of adsorbate and surface need to be taken into account. Nonetheless, as a remarkable number of studies on metalloporphyrins [50, 51] and -phthalocyanines [52, 53] nicely demonstrate, the (NI)XSW technique provides valuable insights on the adsorption of molecular overlayers and, specifically, on the interactions between these molecular adsorbates and the supporting substrate. Furthermore, the obtained structural parameters represent an excellent benchmark to test and improve the predictions of theoretical models, as will be demonstrated in chapter 5 of this thesis.

3 Instrumentation

By ensuring ultra-clean and well-controlled experimental conditions (cf. section 2.1), as well as the technical prerequisites for the experimental tools described in chapter 2, a ultra-high vacuum vessel provides the basis for each of the presented investigations. To maintain the UHV regime, usually the vacuum chamber is continuously pumped by means of a combination of turbomolecular-, titanium sublimation- and ion pumps. The various measuring devices such as, e.g., electron analyzers, LEED optics, mass spectrometers, pressure gauges, as well as ancillary facilities such as gas inlets for sputtering and gas dosing, sputter guns, X-ray and light sources, evaporators for molecule and/or metal deposition, etc., are vacuum-tightly mounted onto this chamber. The centerpiece of each setup is the so-called manipulator, which – by bearing the sample – allows to maneuver it within the chamber, enabling the precise positioning required for the various experimental methods.

3.1 On-Campus UHV Chamber

A sketch of the major UHV setup used throughout this thesis, at the TUM campus in Garching (E20 chair), is given in Fig. 3.1. This custom-made chamber comprises a SPECS Phoibos 100 CCD hemispherical analyzer (1) combined with a pixelfly camera by PCO. For recording XP spectra, the software package SpecsLab2 (version 2.74-r24090) by SPECS is used. X-rays are generated by means of a twin anode X-ray source (2), providing non-monochromatized Al- and Mg-$K\alpha$ radiation with photon energies of 1486.6 eV and 1253.6 eV, respectively. The angle ε between X-ray source and entrance axis of the analyzer is smaller than 90°. Latter allows to perform XPS in normal electron emission (NE) geometry. The sample (3) is mounted on a four degree-of-freedom manipulator (4) that allows for polar angle rotation around the manipulator axis z and translation along the x-, y- and z-coordinates. Furthermore, by means of liquid nitrogen flow through the manipulator, the sample can be brought down to a minimum temperature of around 85 K. For sample heating, a filament is placed directly behind the single crystal sample. Temperature and heating rate are controlled by the combination of a K-type thermocouple junction in direct contact with the single-crystal samples and a proportional-integral-derivative (PID) controller (Schlichting Physikalische Instrumente HS 130). For most of the experiments the sample manipulator is actively cooled by liquid nitrogen flow, both to allow for sample cooling and to reduce the residual gas pressure, therefore continuous

counter-heating is often required. Finally, as the chamber was originally designed to let in synchrotron radiation impinging onto the sample along the z-axis, the manipulator design is such that each sample will have a forward tilt β of about 7°. Due to this, both the electron analyzer (1) as well as the mass spectrometer (11) will be tilted accordingly to face the sample along its surface normal. On up to three ports, home-built ribbon- and molecular evaporators (5) can be mounted for thin-film deposition. The molecules are evaporated from quartz-glass crucibles (outside diameter 4.9 mm, wall thickness 0.5 mm, height 9 mm, purchased from Gaßner Glastechnik GmbH, Munich) which are heated inside boron nitride crucibles. The preparation of a clean surface is performed with the help

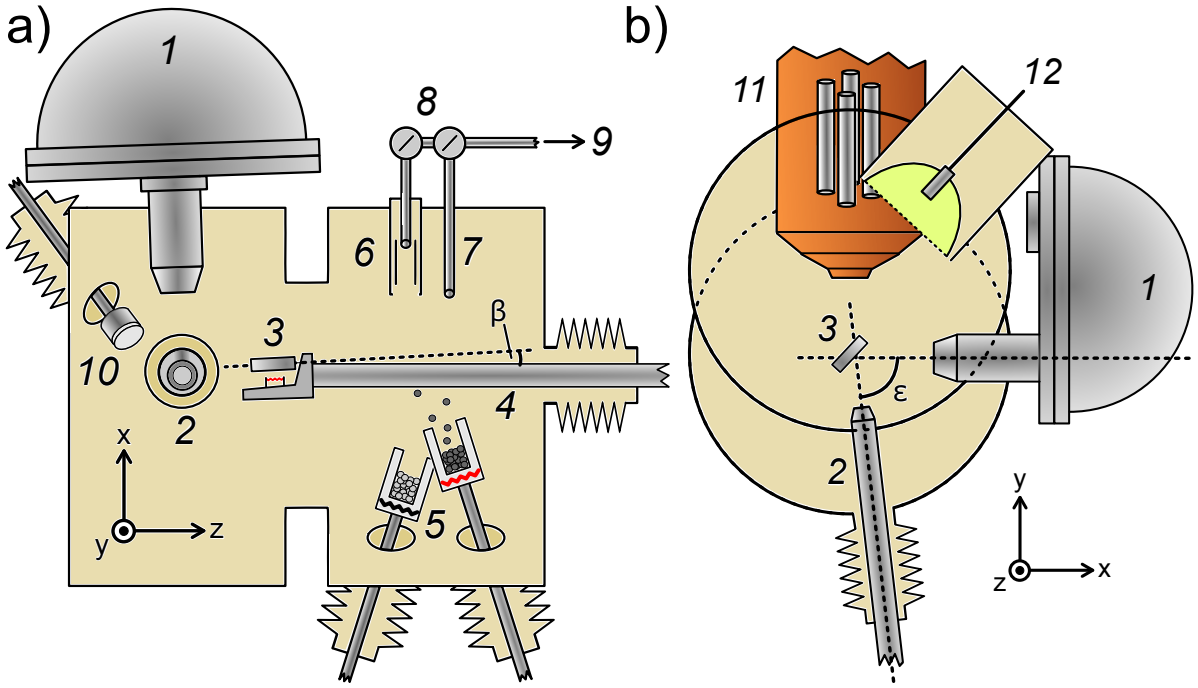

Figure 3.1: Schematic sketch of the UHV chamber, mounted on campus at the chair E20: a) top- and b) front view, along the axis of the manipulator (z-axis), of the chamber. The numbered components are described in the text.

of a sputter gun from Varian (model 981-2043) (6). For controlled deposition of molecules from the gas phase, the sample is placed in front of a home-built microcapillary-/needle doser (7). Both the sputter gun and the needle doser are supplied with gases by a gas-dosing system (GDS) (9). Latter is a separately pumped UHV compartment, where a number of precision leak valves allow to use different gases in parallel. Sputter gun and needle doser are separated from the main chamber *via* two distinct valves (8). The valve towards the needle doser can be controlled pneumatically and enables, in combination with a Baratron manometer (by MKS) measuring the absolute pressure in the GDS, to

expose the sample to predefined amounts of gases. A home-built re-entrant window (10), described in section 3.3, forms the basis of a re-entrant light source to expose the sample to visible and UV light delivered by suitable light-emitting diodes (LEDs). TPD measurements are realized with a quadrupole mass spectrometer (11) that is described in Ref. [54] and mounted inside a copper Feulner-cap. Specifically, as for monitoring H_2 desorption with TPD the residual H_2 pressure needs to be reduced to a minimum, surfaces within the liquid nitrogen cooled copper-cap are additionally covered by a freshly deposited titanium getter film to accomplish both cryo-tapping and efficient trapping of background H_2 and H [54]. Furthermore, for all TPD measurements the samples are positioned very close ($\sim$1 mm) to the entrance aperture of the Feulner-cap, which has a diameter of 8 mm and, thus, is slightly smaller than the probed single crystals which usually have 10 mm diameter. An additional cold trap that is cooled by liquid nitrogen flow and similarly covered by freshly deposited titanium films from a titanium sublimation pump (TSP) further aids to maintain low background pressures by cryo-trapping and trapping of H_2. Finally, the BDL800IR-LMX-ISH LEED spectrometer (12) by OCI Vacuum Microengineering Inc. is mounted for surface structure determination. The base pressure of the described chamber normally is in the low 10^{-10} mbar but, by means of liquid nitrogen cooling can easily be brought down to the low 10^{-11} mbar during operation.

3.2 Endstation of the I09 Beamline at DLS

For the synchrotron radiation measurements of chapter 5, the endstation at the I09 beamline of the Diamond Light Source (DLS) was utilized. The UHV chamber is equipped with a VG Scienta EW4000 HAXPES hemispherical electron analyzer with a maximum angular acceptance of $\pm 30°$ and also provides the standard tools for sample sputtering, gas dosing (by backfilling the chamber) and sample annealing, and free ports for inserting evaporators. The sample, mounted on Omicron type sample plates, is maneuvered by means of a 5-axis manipulator that allows for polar (around the manipulator axis) and azimuthal (around the surface normal of the sample) rotation and linear translation along the x-, y- and z-coordinates. In contrast to the on-campus chamber described in section 3.1, no thermocouple can be attached directly to the sample. Thus, heating is realized by applying the heating power according to a calibrated reference-table. In a similar manner, as described in section 3.1, the sample can be cooled by liquid Helium flow. For the presented NIXSW measurements in chapter 5, the experimental chamber was oriented such that the incident photon beam and the entrance axis of the hemispherical analyzer form an angle of either 60° or 90°, and the base pressure in the chamber was $\sim 5 \times 10^{-10}$ mbar. In addition to the photoemission yield measurement, Darwin reflectivity curves are recorded by monitoring the fluorescence yield from the Bragg-reflected light in the reverse direction to the incident photon beam, along the fringes of the port through which the synchrotron light enters the chamber.

3.3 Design of a Versatile LED-Based Re-Entrant Light Source

Considering recent investigations on the photo-induced water splitting of titanyl phthalocyanine (TiOPc) [15] and oxotitanium tetraphenylporphyrin (TiOTPP) [14] as well as the reported light-induced C-Br dissociation on a Au(111) surface [55], to expand the surface science toolbox for photochemistry is highly appealing, especially when considering the relevance of photochemical processes in nature and the abundance of sunlight. For the study of such light-induced processes, light emitting diodes (LEDs) nowadays offer a powerful, affordable and easy to handle alternative to both tunable lasers and deuterium-, halogen- and xenon lamps. Usually regarded to be at disadvantage when compared to collimated and focused laser beams, LEDs emit light over a broad angular range and, thus, are intrinsically well suited to evenly expose extended surfaces to light. In addition to the utile small footprints and the low costs, LEDs also offer narrow bandwidth light and, thus, do not require the use of a monochromator. Finally, the wavelengths accessible to LEDs cover almost the entire visible range from 400 - 700 nm and even go down to ultraviolet (UV) wavelengths of 265 nm, rendering light emitting diodes a versatile tool for photochemical investigations. To exploit them in a UHV setup, such as that described in section 3.1, one faces the general problem of focusing the highly divergent LED light onto the sample, the latter usually being few tens of centimeters distant from the designated entrance window mounted on the chamber. In the presented work, a simple LED-based re-entrant light source was devised, circumventing this problem by simply bringing the light emitting diode as close as possible to the sample. In addition, since comparable re-entrant windows, commercially available at the time of the development of this light source, costed more than 4000 € (allectra, VACOM, etc.), the re-entrant window was to be custom-built. Eventually, as a striking advantage over the commercial models, this newly devised re-entrant window allows for the easy exchange of the window glass. Together with the setup of the light source allowing the replacement of the LED, this renders the designed tool extremely versatile. Two proof-of-concept studies, showing the first successful application of the devised light source, are presented in chapter 7.

3.3.1 Setup and Design

The basis for the custom-built light source is formed by the re-entrant window depicted in Fig. 3.2a. At the end of a stainless steel tube (1) of 18 mm outer diameter and 1 mm wall thickness, on the head section of the re-entrant window, a plane, circular window glass (5) of 20 mm diameter can be mounted. In the present work, a borosilicate window glass of 3 mm thickness is utilized. The UHV-tight seal between window glass and stainless steel tube is realized by means of a single perfluoroelastomer (G75B / FFKM 79) O-ring (4) of 16 mm inner diameter and either 1 mm or 1.04 mm thickness (purchased from C. Otto

Gehrckens GmbH & Co. KG, with item numbers A4N2341229 and A4N2076420, respectively). This O-ring is embedded in a $z = 0.7\,\text{mm}$ deep and $y = 1.1\,\text{mm}$ wide circular groove (3) with a mean diameter of 17 mm. The glass window is evenly pressed against

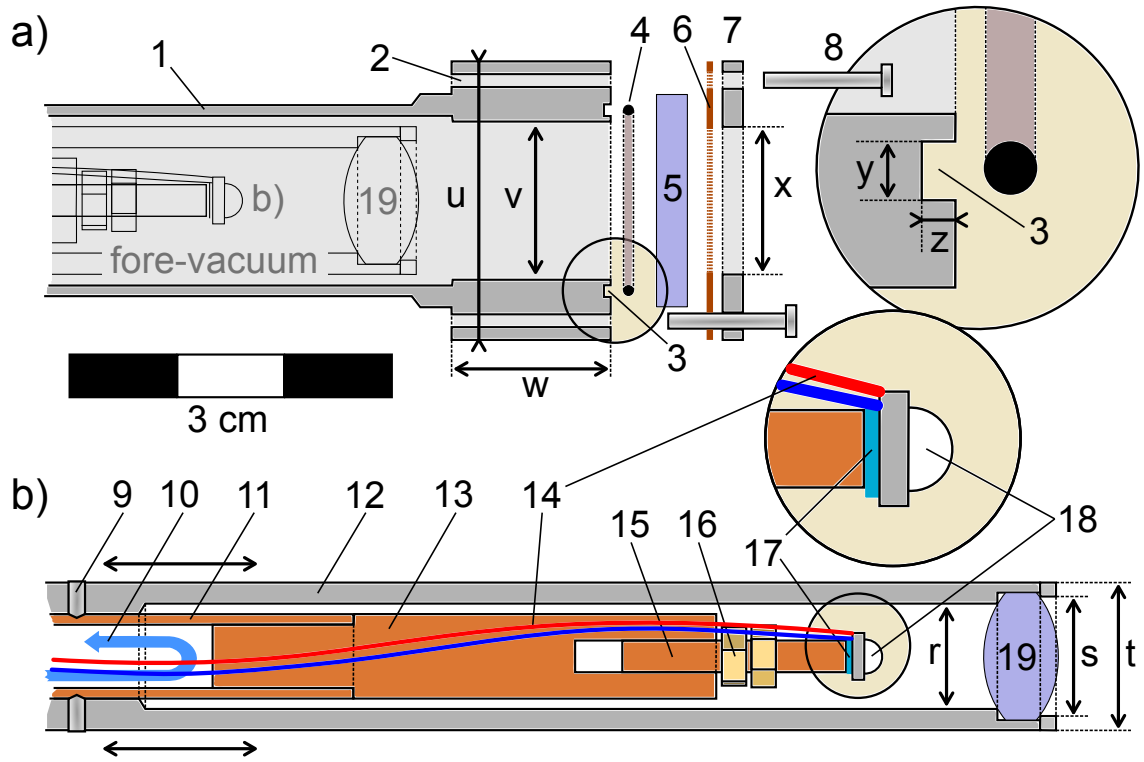

Figure 3.2: Schematic model of the versatile LED-based re-entrant light source devised in this work: a) Re-entrant window, housing the LED-based light source shown in b). b) Light source containing the light emitting diode (18), which is mounted onto an exchangeable copper socket (15) by thermal adhesive. The illustration is true to scale according to the depicted scale-bar. The numbered components are described in the text.

the embedded O-ring *via* a 2 mm thick stainless steel cover plate (7) with a circular aperture of $x = 14\,\text{mm}$ diameter by means of two $M1.6$ screws (8) that go into the respective threaded holes (2). As a protective layer between the fragile window glass (5) and the cover plate (7), a piece of Kapton foil (6) is used. The outer diameter u of the $w = 15\,\text{mm}$ long head section of the re-entrant window amounts to 26.2 mm, allowing the device to be inserted into any standard DN40 CF (ConFlat) chamber port. The inner diameter v of the head section is, constrained by the dimensions of the O-ring groove, slightly reduced from 16 mm, the inner diameter of the stainless steel tube (1), to 14.9 mm. Even though the perfluoroelastomer O-ring seals to the low $10^{-10}\,\text{mbar}$ and lower, during operation in UHV the volume behind the window is pumped by a membrane pump (cf.

"fore-vacuum" in Fig. 3.2a) to avoid leaking of small gases such as hydrogen or helium. Finally, the re-entrant window can be safely baked at temperatures up to 150 °C (higher baking temperatures were not tested so far).

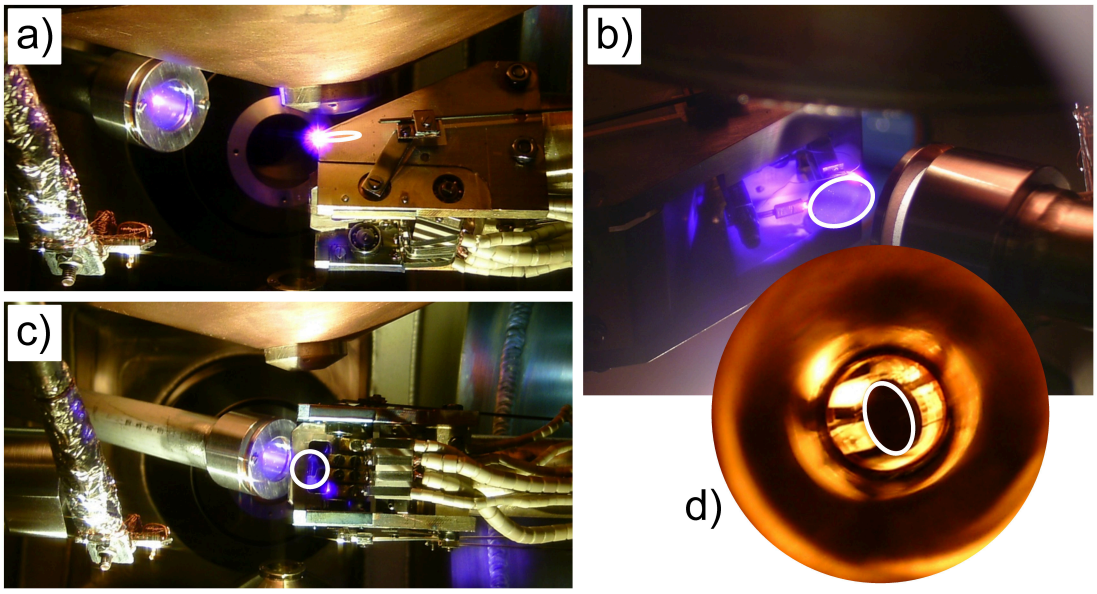

Figure 3.3: Images of possible application scenarios for the re-entrant light source with the position of the exposed sample highlighted by the solid-line white circles: a) Illumination of the sample positioned in front of the mass-spectrometer aperture (described in section 3.1) to monitor light-induced desorption. b) and c) Illumination of the sample surface with the light source very close, viewed out of two different perspectives. d) View through the re-entrant window, facing the sample. In a), b) and c) a 365 - 370 nm LED is utilized.

The light source depicted in Fig. 3.2b, with a maximum outer diameter of $t = 14$ mm, is designed to be inserted into the re-entrant window described in Fig. 3.2a. Type LZ1 light emitting diodes (18) (LED Engin, Inc.) with a square base of side length 4.4 mm are glued onto ∼20 mm long copper rods of 3 mm diameter (15), latter being of similar dimension as the thermal contact pad of the LED. To provide a good thermal contact (17) between the LED and the supporting copper rod, the two-component Arctic Silver thermal adhesive (Arctic Silver Incorporated) is applied. Furthermore, the LED-bearing rod (15) is mounted, by means of an $M3$ thread and screw nuts (16), onto a solid copper rod of 8 mm outer diameter (13), allowing facile exchange of the LED as well as ensuring good thermal contact. The 8 mm copper rod (13) is, in turn, vacuum-tightly integrated inside a copper tube (11) of similar outer diameter and 1 mm wall thickness by means of an $M7$ fine thread. Water or air flow through this copper tube (11), indicated by the blue arrow (10) in Fig. 3.2b, provides the cooling needed for the steady operation of the LED.

To reduce the angular spread of the emitted light, a fused silica double-convex lens (19) (DCX-UV 12 X 12 UNCTD, item number 48034, purchased from Edmund Optics Inc.), hosted inside a brass housing (12), can be shifted in front of the LED and fixed on the copper tube (11) by headless screws (9). The inner diameter r and the aperture s of the brass housing amount to ∼10 mm and ∼11.3 mm, respectively. Finally, to provide the LED with electric current, flexible wires (14) are soldered directly to the contacts at the back of the LED base plate. Finally, concluding the description of the devised re-entrant light source, some of the possible application scenarios are illustrated in Fig. 3.3.

3.3.2 Power Density Curve of UV-LED

For UV light exposure, LZ1-00UV00 high-power LEDs (LED Engin, Inc.) with a wavelength of 365 - 370 nm were used. In order to determine the corresponding power density (in mW/cm^2) of the UV light emitted from the re-entrant light source at given distances z from the stainless steel cover plate (7), in line of sight of the re-entrant window (cf. Fig. 3.4), a self-made bolometer was applied. As the light needs to pass through both the fused silica double-convex lens (19) and the borosilicate glass (5), the corresponding light intensity will be attenuated accordingly. The bolometer, sketched in Fig. 3.4b, consists of a 5 mm thick quadratic copper block of side length $y = 3$ cm (4). For light absorption, the light exposed side of the copper block (the absorber) is coated by commercial camera varnish (3) (Tetenal Europe GmbH, item number 105202). In order to reach the absorber, which is shielded inside a metal housing (2), the light has to pass a quadratic aperture of side length $x = 1$ cm, corresponding to an entrance area of 1 cm^2, placed at a distance z from the stainless steel cover plate (7) of the re-entrant light source. The absorber is in thermal contact with a heat reservoir at 15 °C (T_2) and is actively heated (P_{heat}) to a constant temperature T_1, higher than T_2. Thus, at thermal equilibrium, the difference in the power P_{heat} needed to keep the absorber at the constant temperature T_1 in the presence or absence of light exposure, directly provides the incident power density P_{light} per cm^2. The results of the performed power density measurements for two 365 - 370 nm LEDs, recorded with the water-cooled light source at ambient conditions, are shown in Fig. 3.4c. In both cases, the LZ1-00UV00 LEDs have been operated at a current of 0.7 A. At this current, the emitted power density, at a reasonable distance of $z = 5$ cm, still amounts to ∼100 - 130 mW/cm^2, which is roughly 10 % of the 1200 mW radiant flux specified in the manufacturer information for the operation at 0.7 A. Note also that, as the light absorption by the black absorber will be less than 100 %, the measured power density of Fig. 3.4c only provides a lower limit for the emitted power density. Finally, considering the slightly reduced intensity of LED 2 in Fig. 3.4c, one should be aware that for the applied UV LEDs some progressive degradation has been identified after prolonged operation. While LED 1 was used as purchased, LED 2 has already been used for at least ∼110 min at fore-vacuum conditions. The reason for this degradation, so far, remains unclear but could, in principle, stem from either a still insufficient cooling of

the LED or from the operation of the LED under fore-vacuum conditions (which could be as well detrimental for the cooling of the LED). Thus, possible solutions to prevent such degradation could involve both the reduction of the applied current as well as operation of the light source in noble gas atmosphere instead of fore-vacuum.

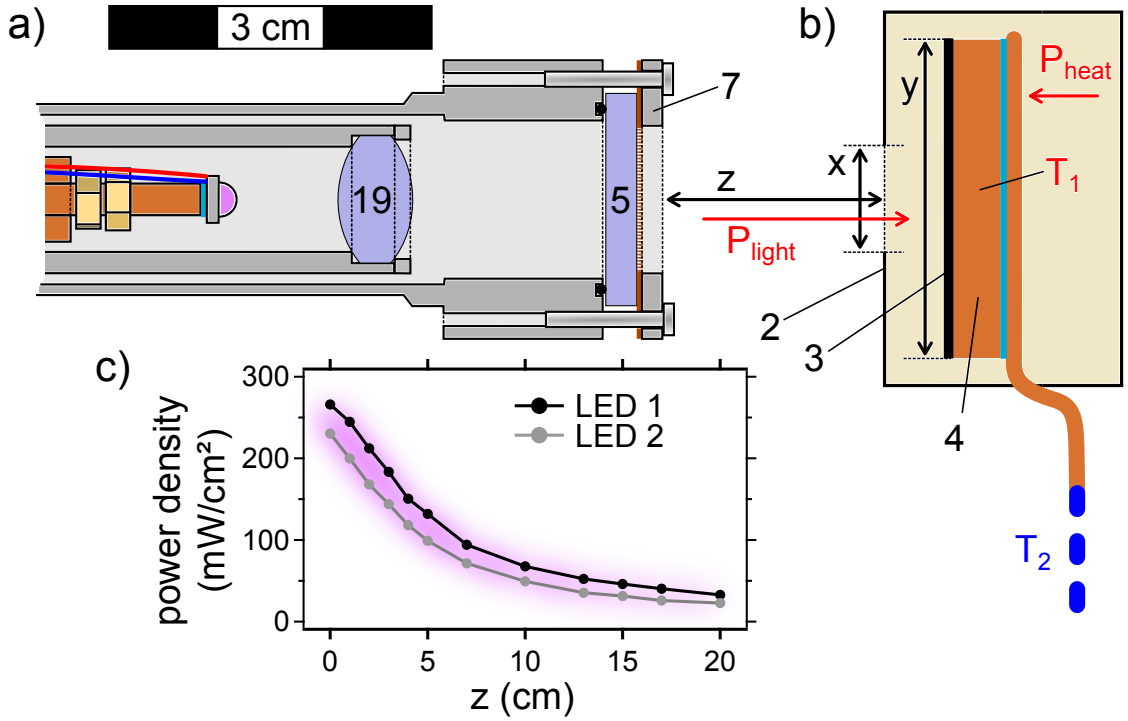

Figure 3.4: Schematic of the setup for power density characterization of the ultraviolet light emitted from the devised re-entrant light source: a) Light source equipped with a 365 - 370 nm LED (LZ1-00UV00) inside the re-entrant window (cf. Fig. 3.2). b) Sketch of the self-made bolometer to estimate the power density emitted from the re-entrant light source at given distances z. c) Determined power density (in mW/cm^2) as a function of the distance z from the re-entrant window for two 365 - 370 nm LEDs. The illustrations are true to scale according to the depicted scale-bar. The numbered components are described in the text.

4 On-Surface Polymerization Reactions – a Model Spectroscopy Study

---

This chapter includes content that has been published in

P. S. Deimel, K. Stoiber, L. Jiang, J. A. Lloyd, S. C. Oh, S. Fischer, Ö. Sağlam, H. Schlichting, A. C. Papageorgiou, J. V. Barth, F. Allegretti, and J. Reichert, **"Bisphenol A and Diethylstilbestrol on Cu(111): On-Surface Polymerization Initiated by Hydroxy-Directed *Ortho* C-H Bond Activation,"** The Journal of Physical Chemistry C, vol. **123**, no. 2, pp. 1354–1361, 2018. Reproduced with permission. Copyright (2019) American Chemical Society.

Scanning tunneling microscopy measurements and images have been made by

L. Jiang, J. A. Lloyd, S. C. Oh, S. Fischer, Ö. Sağlam, A. C. Papageorgiou and J. Reichert

Quantitative analysis of temperature-programmed desorption data has been performed by

K. Stoiber and H. Schlichting

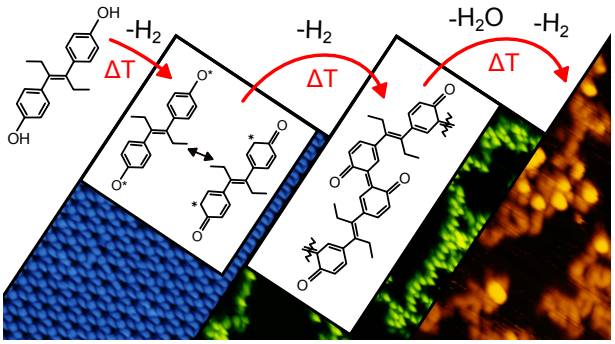

The combination of scanning tunneling microscopy (STM), X-ray photoelectron spectroscopy (XPS), temperature-programmed XPS (TP-XPS) and temperature-programmed desorption (TPD) measurements is employed to shed light on the complex thermal evolution of Bisphenol A (BPA) and Diethylstilbestrol (DES) on Cu(111) and provides clear evidence for hydroxy-directed on-surface polymerization, originating from *ortho* C-H bond activation. Both these technologically highly relevant molecules follow a common pattern

of sequential chemical transformations, as highlighted by TPD and XPS results, eventually yielding disordered networks of branched polymers, which are observed by STM. The presented findings *via* an original methodological approach contribute to the store of knowledge in surface-supported, covalent coupling reactions, stressing the impact of directing group, role of the chosen substrate and nature of the selected molecules.

4.1 Introduction

The exploitation of covalent coupling and polymerization reactions on surfaces is a promising strategy for the bottom-up fabrication of sophisticated and robust low-dimensional networks [56–63] with potential application in, e.g., nanoelectronics, catalysis and gas sensing [64–66]. In particular, the selective creation of reactive sites by the surface-assisted thermal dissociation of halogen-carbon bonds has been recognized as a key ingredient to control on-surface polymerization processes in a hierarchical fashion [67–70]. In the specific case of these surface-assisted Ullmann coupling reactions [19], however, the chemisorbed halogen species remains on the surface upon dissociation and may influence or even hinder the formation of expanded covalent networks [55, 71, 72]. In this regard, condensation reactions such as boronic acid self-condensation [73–75] and imine (Schiff-base) formation [76–78] have been shown to offer viable alternative routes to form covalent networks by on-surface synthesis, while preventing co-adsorption of undesired byproducts.

Motivated by the prominence of graphene-inspired low-dimensional materials, C-C covalent coupling represents a further byproduct-free alternative to Ullmann coupling reactions and has emerged as one of the most explored routes for polymerization [62, 79]. In this realm, a strategy to induce highly selective C-C coupling without resorting to halogenated precursors could, e.g., involve the use of anisotropic supports as proposed in Refs. [80, 81]. There, the surface anisotropy of Au(110) and Cu(110) surfaces was exploited to guide the alignment of individual reactants, thus providing a 1-D constraint to steer the selective C-H bond activation in linear alkanes and arenes. Alternatively, in the effort to circumvent the poor selectivity and relative inertness of the C-H bonds, Li et al. [20] demonstrated that control over the C-H activation at a specific site can be achieved by the combined use of a directing hydroxyl group and an appropriate substrate to catalyze the C-C coupling reaction. Specifically, stepwise *diselective ortho* C-H bond activation was shown on a Au(111) surface for two model hydroxyphenyl compounds, eventually leading to formation of two-dimensional porous networks of covalently linked molecules. Phenoxyl radicals formed on the surfaces (cf. Fig. 4.1a and b) were shown to undergo *enol-keto* tautomerism (cf. Fig. 4.1b and c), with the unpaired electron located at either the oxygen atom (*enol* tautomer) or an *ortho*-carbon atom (*keto* tautomer). Density functional theory (DFT) suggests that an adatom approaching this *ortho*-carbon can stabilize the *keto*-form intermediate, favoring the first *ortho-ortho* C-C bond formation with a neighboring molecule (cf. Fig. 4.1d). Subsequently, steric hindrance of the second *ortho* dehydrogenation causes an adatom to first bind to the oxygen atom of the obtained product, whereby it can either attack the α-carbon, leading to deoxygenation, or the second *ortho*-carbon, leading to dehydrogenation. According to DFT, on Au(111) the activation barrier for this second C-H activation is lower than for the C-O bond cleavage, and the preference for the second *ortho* dehydrogenation reaction and subsequent *ortho-ortho* coupling thus results in the formation of porous networks with symmetric

binding motifs. Conversely, on Ag(111) *monoselective ortho* C-H bond activation was favored, with deoxygenation being preferred over the second *ortho* C-H bond scission, as suggested by DFT. Upon detachment of the oxygen atom, further *ortho* C-H bond activation and *ortho-ortho* coupling is hampered, and remarkably different topography and binding motifs of the covalently linked networks are then observed on this surface compared to Au(111) [20]. This hydroxy-directed C-C coupling mechanism represents a promising tool for the design of ever more complex and highly stable covalent architectures. In the present work, we demonstrate the sequential nature of the process by directly monitoring the products of the competitive dehydrogenation and deoxygenation reactions, and we further explore the role of the directing group, the selected substrate and the molecular modules. This was realized by investigating the chemical and structural evolution of two model compounds, Diethylstilbestrol (DES) and Bisphenol A (BPA), on an atomically well-defined Cu(111) support under UHV conditions. The self-assembly of BPA on Ag(111) and Cu(111) has been studied before [82, 83], and a stepwise thermally induced deprotonation of the BPA molecules was found to occur on copper [83]. Here we focus on the comparison of the on-surface chemistry of these two industrially relevant, closely related compounds.

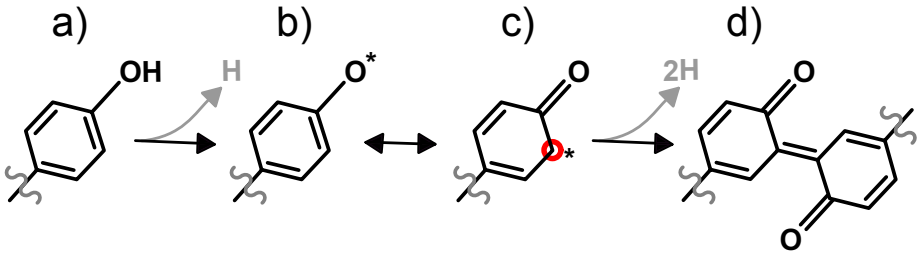

Figure 4.1: Sequence of reaction steps leading to *ortho-ortho* coupling between two hydroxyphenyl compounds, according to Li et al. [20]: on metal surfaces, after annealing to sufficiently high temperatures, the phenol group (a) loses hydrogen to form a phenoxyl radical (b). The latter may exist in both the *enol-* (b) and *keto*-form (c). In the *keto*-form (c), with the unpaired electron located on the *ortho*-carbon (highlighted by the red circle), surface-assisted C-H bond activation at the *ortho*-carbon is followed by dehydrogenation and (*ortho-ortho*) C-C bond formation between neighboring molecules (d).

The chemical structure of DES and BPA is illustrated in Fig. 4.2, with both molecules featuring two terminal hydroxyl groups, each connected to an aromatic ring. The phenol rings are linked by a diethylstilbene and dimethylmethane bridge in DES and BPA, respectively. Having rather similar structure, these molecules are both widely used chemicals and suspected to cause a variety of adverse health effects. Besides interfering with the hormone system as so-called endocrine disruptors [84–86], they are believed to cause transgenerational damage by hyper- and hypomethylation of DNA and alteration of the epige-

netic code [87, 88]. DES was administered to pregnant women between 1940 and 1971 as a synthetic nonsteroidal estrogen, but in 1971 it was first argued to be teratogenic [89, 90]. As a consequence, DES is not used in pharmacy since 1991, whereas, rather surprisingly, the exposure of BPA to humans is still very high since it is still employed in the production of manifold plastic products and coatings [91]. With this background, it is of special interest to shed light on the similarities as well as the differences of the chemical reactivity of DES and BPA, which is tackled here through a detailed atomistic study of a three-step reaction pathway from monomers to conjugated polymers on the Cu(111) surface upon thermal treatment.

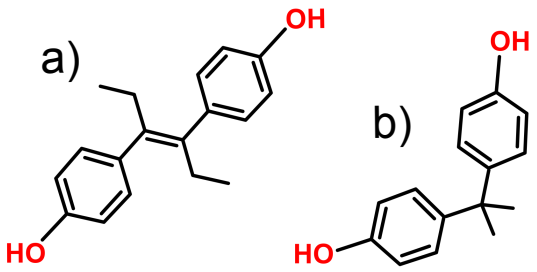

Figure 4.2: Chemical structure of a) Diethylstilbestrol (DES) and b) Bisphenol A (BPA). The terminal hydroxyl groups are highlighted in red.

4.2 Experimental Details

Our study was conducted in two different experimental chambers hosted at the Technical University of Munich. The custom-made UHV chamber described in section 3.1 was used for XPS, TP-XPS, TPD and LEED measurements. A second custom-designed UHV chamber with a base pressure of $\sim 4 \times 10^{-10}$ mbar was utilized to investigate the topography and the structural evolution of adsorbed DES and BPA films by means of STM. The STM set-up comprises a preparation chamber and an analysis chamber hosting a SPECS Aarhus type variable temperature STM. Furthermore, chemically etched tungsten (W) tips were used, and the voltage given in the tunneling conditions (cf. caption of Fig. 4.3) refers to the sample bias. The obtained topographic images were processed by WSxM [92]. All STM measurements and the corresponding image processing have been carried out by L. Jiang, J. A. Lloyd, S. C. Oh, S. Fischer, Ö. Sağlam, A. C. Papageorgiou and J. Reichert.

The XPS measurements were carried out using non-monochromatized *Al-K*α emission (photon energy: 1486.6 eV). All TP-XPS measurements were performed in normal electron emission (NE) geometry and with the large area (LA) lens mode of the Phoibos 100

analyzer. Here, the LA lens mode is used to increase signal intensity by an increased acceptance area in order to decrease the acquisition time of each individual XP spectrum while ramping linearly the temperature. The standard XP spectra, in contrast, have been acquired in the more usual medium area (MA) lens mode. In both XPS and TP-XPS measurements a pass energy of 15 eV, open exit slit and entrance slit 5 were used. The binding energy of all XP spectra was calibrated against the Cu $2p_{3/2}$ core level of the Cu(111) substrate at a binding energy of 932.67 eV [93]. To generate the O 1*s* TP-XPS contour plots (presented in Fig. 4.4a and b), the same linear background was subtracted from all O 1*s* spectra, followed by their normalization to both ends of the spectra. To obtain the plots of the corresponding O 1*s* and C 1*s* intensities as a function of temperature (presented in Fig. 4.6), the individual core-level spectra were fitted with Gaussians on a linear background after averaging two subsequent XP spectra. Here, for fitting the O 1*s* signals, one Gaussian peak covers the energy region of the high binding energy O 1*s* components (cf. peaks 1 and 3 in Fig. 4.4a and b); the other Gaussian peak is constrained to the low binding energy regime (cf. peak 2 in Fig. 4.4a and b). Finally, the intensities were determined by integrating the area under the obtained Gaussian fits. The TPD measurements were performed with the quadrupole mass spectrometer described in section 3.1, and with the distance between the Feulner-cap [54] aperture and the Cu(111) sample adjusted as close as possible (∼1 mm). Specifically, in order to minimize the pressure in the ionizer region, the inner surface of the Feulner-cap serves to pump residual gases (e.g. background H_2 and H) *via* deposition of a reactive titanium getter film and cryogenic trapping by liquid nitrogen cooling. In addition, during all experiments, the combination of a cold trap operated with liquid nitrogen flow and a titanium sublimation pump reduced the chamber background pressure to the mid/low 10^{-11} mbar range. Furthermore, as the manipulator was steadily cooled *via* liquid nitrogen flow, counter-heating the sample was necessary to reach sample temperatures above ∼85 K. LEED patterns were recorded without counter-heating and the sample at ∼85 K.
Clean Cu(111) surfaces were prepared by sputtering commercial Cu(111) single crystals (Surface Preparation Laboratory, the Netherlands) for 30 min with either Ne^+ or Ar^+ ions at room temperature (RT). The surface order was restored by annealing the crystal to 770 K - 800 K for 5 - 10 minutes. Diethylstilbestrol (Sigma Aldrich, purity 99 %) was deposited by means of a home-built molecular beam evaporator at about 335 K, with the Cu(111) crystal kept at 200 K (XPS-TPD chamber) or 300 K (STM chamber). Prior to the first deposition, the DES powder was outgassed to a maximum temperature of 360 K for 5 minutes. Bisphenol A (Sigma Aldrich, >99 %) was evaporated at 340 K, in a similar manner as the DES, and with the substrate kept at 200 K (XPS-TPD chamber) or 300 K (STM chamber). Prior to the first deposition, the BPA was outgassed to a maximum temperature of 350 K for 10 minutes.

4.3 Results and Discussion

After deposition onto the Cu(111) surface at 200 K and subsequent mild annealing up to ∼380 K, both DES and BPA readily self-assemble into well-ordered molecular overlayers, as it was recently reported also for biphenols [94]. Our STM measurements reveal densely packed hexagonal superstructures (cf. Fig. 4.3, bottom left), described elsewhere [83, 95]. The LEED pattern of DES, displayed in Fig. 4.3 (top left), nicely corresponds to the respective STM image and can be described by a commensurate superstructure with the matrix $\begin{pmatrix} 6 & 3 \\ 3 & 6 \end{pmatrix}$. The associated rhombic primitive cell includes a 60° angle, has a side length of 13.3 Å (assuming a Cu(111) surface lattice constant of 2.56 Å) and incorporates three DES molecules. A hexagonal structure is also observed for BPA after annealing slightly above RT (cf. Fig. 4.3, bottom left), which consists of trimeric motifs [83]. Faint diffraction spots in the LEED pattern indicate the formation of a long-range ordered overlayer, which is – however – rapidly disrupted by the electron beam. Upon heating to higher temperatures (DES: 460 K; BPA: 470 K), the periodic overlayers irreversibly convert into branched, polymer-like chains with clearly identifiable molecular features that are imaged as distinct protrusions (cf. Fig. 4.3, bottom), suggesting the covalent linking of individual molecules. Finally, at even higher temperatures (e.g., 540 K for DES and 730 K for BPA), the formerly sharp molecular features are smeared out, indicative of further chemical modification of the molecular chains. Importantly, even though DES and BPA have a different chemical structure, the temperature induced chain formation and evolution is remarkably similar, thus pointing to a common reaction mechanism.

In order to shed light on the three-step chemical evolution on Cu(111) described above, we performed XPS and TP-XPS measurements whose results are illustrated in Fig. 4.4 and Fig. 4.5. When DES is deposited onto the Cu(111) surface at 200 K, a dominant O 1*s* feature is observed at a binding energy of 533.1 eV (Fig. 4.4a, peak 1): this component is ascribed to the terminal hydroxyl groups [20, 97–99] and thus clearly indicates that both hydroxyl species remain intact at this temperature. However, after heating above 300 K, the peak labelled 1 has almost completely vanished and is replaced by a new feature at 530.9 eV (Fig. 4.4a, peak 2). This new component is attributed to deprotonated hydroxyl groups with a binding energy characteristic of a carbonyl species lying close to the Cu surface [83, 97, 100–102]. From the evaluation of the O 1*s* core-level intensity in Fig. 4.6a, it is inferred that the chemical transformation (peak 1 → peak 2) starts well below 300 K and is completed at 350 K. Further annealing above 500 K changes again the O 1*s* fingerprint, re-establishing a higher binding energy component located at ∼533.6 eV (cf. Fig. 4.4a), referred to as peak 3, which progressively replaces the carbonyl-related peak 2. A detailed fitting analysis of the corresponding O 1*s* core-level spectra is presented in Fig. 4.4c, which clarifies the evolution of the three above-mentioned peaks.

Fig. 4.6a shows that the second process, related to the transformation of peak 2 to peak 3, terminates with the complete disappearance of oxygen at temperatures higher

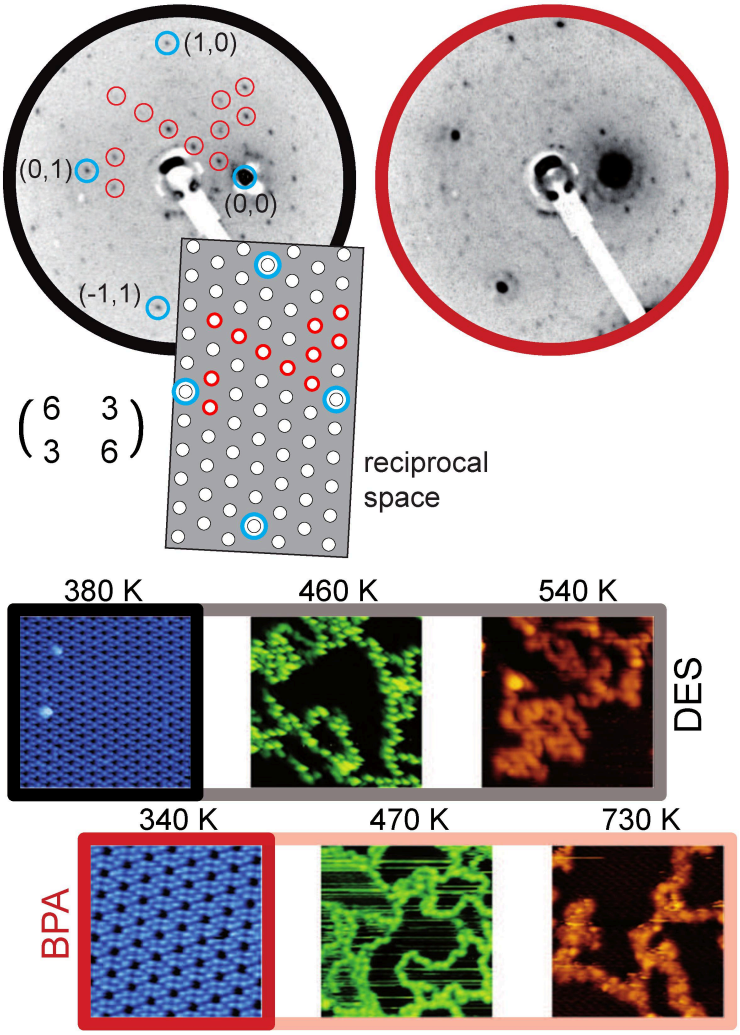

Figure 4.3: Top: LEED pattern of DES/Cu(111) (left, black edging) and BPA/Cu(111) (right, red edging) after annealing to 380 K and 340 K for 5 min, respectively. Both images are taken at E_p=70 eV and T_{sample}≈85 K. For DES the reciprocal lattice pattern, generated with LEEDpat 4.2 [96], is shown: it corresponds to a commensurate superstructure with the matrix $\begin{pmatrix} 6 & 3 \\ 3 & 6 \end{pmatrix}$. Encircled diffraction spots (red: superstructure; blue: integer spots) underline the correspondence between the experimental and simulated pattern. Bottom: STM images in the same scale (185 × 185 Å^2), showing the thermal evolution of submonolayer coverages of DES [black outline, blue (0.10 nA, 1.50 V, ∼150 K): annealed at 380 K for 15 min, green (0.12 nA, 1.25 V, ∼150 K): annealed at 460 K for 10 min, orange (0.12 nA, 2.02 V, ∼170 K): annealed at 540 K for 10 min] and BPA [red outline, blue (0.10 nA, 1.50 V, ∼220 K): annealed at 340 K for 10 min, green (0.11 nA, 1.25 V, ∼295 K): annealed at 470 K for 10 min, orange (0.12 nA, 1.25 V, ∼295 K): annealed at 730 K for 5 min] on Cu(111).

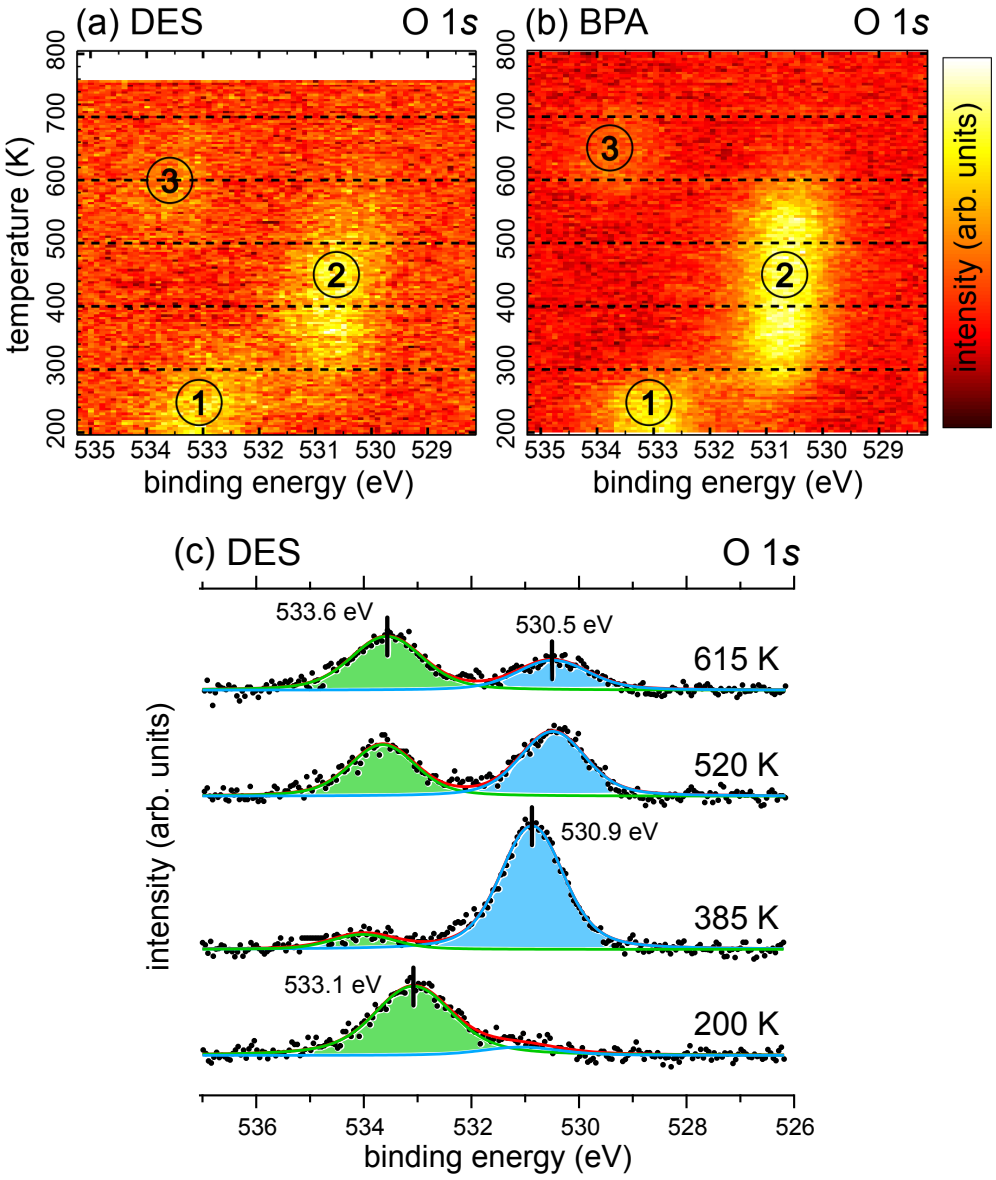

Figure 4.4: O 1*s* (TP-)XP spectra for DES and BPA on Cu(111). Top: O 1*s* TP-XPS contour plots for (a) DES/Cu(111) and (b) BPA/Cu(111). For both molecules, the observed O 1*s* features are labelled 1, 2 and 3. A linear heating rate of 0.1 K s^{-1} was applied. Bottom: (c) O 1*s* core-level spectra including fitting analysis and relevant peak positions for DES/Cu(111) after deposition of DES at 200 K and subsequent annealing steps to 385 K (for 5 min), 520 K (for 10 min) and 615 K (for 10 min). The XP spectra in (c) were performed with the sample kept at 200 K, and, for background correction, a polynomial background was extracted from the clean Cu(111) spectrum and subtracted from the raw data.

than 650 K. The total carbon intensity extracted from the C 1*s* TP-XPS in Fig. 4.5a is also shown in Fig. 4.6a and, in contrast, reveals that the molecular backbone remains mostly intact and adsorbed on the surface up to 750 K; this implies that the progressive loss of oxygen signal is to be attributed to deoxygenation rather than to molecular desorption or disintegration. Notably, the chemical evolution of BPA/Cu(111) appears to be very similar (cf. Fig. 4.4b), with the same succession of components 1, 2 and 3 as for DES. The only clearly apparent difference is that the uptake of peak 3 begins, concomitantly with the overall loss of oxygen, at significantly higher temperatures than for DES (above 550 K, see Fig. 4.6b).

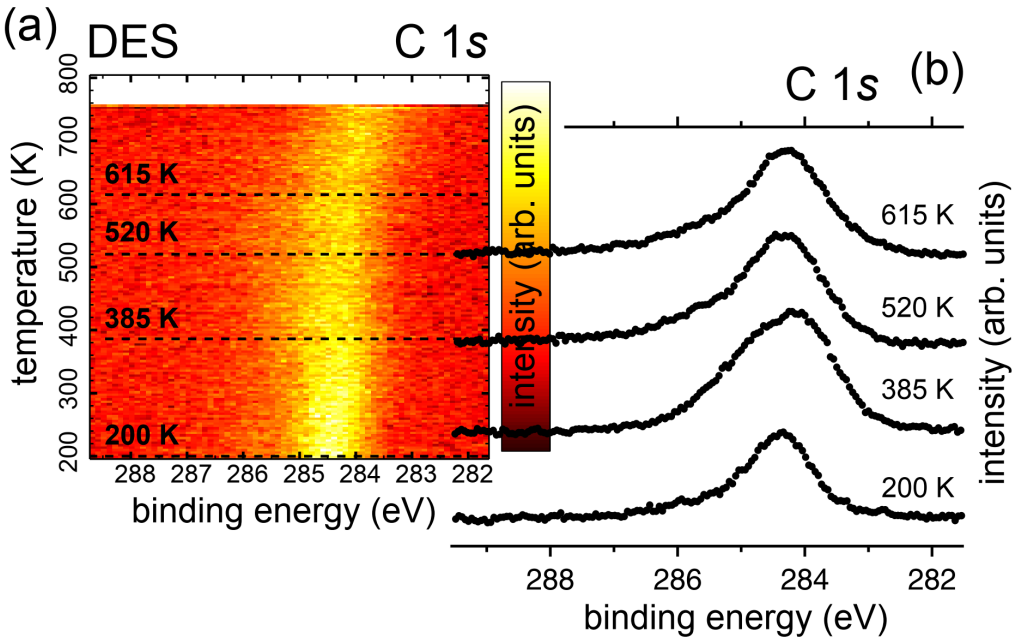

Figure 4.5: (a) C 1*s* TP-XPS contour plot of DES/Cu(111) recorded at a heating rate of 0.1 K s^{-1}, next to (b) the corresponding C 1*s* core-level spectra (recorded at 200 K sample temperature, after deposition of DES at 200 K and subsequent annealing steps to 385 K for 5 min, 520 K for 10 min and 615 K for 10 min). To generate the TP-XPS contour plot, the individual C 1*s* spectra were normalized to both ends after averaging over a set of adjacent spectra.

To correlate unambiguously the chemical changes identified by XPS (Fig. 4.4 and 4.6) to the structural evolution of the DES and BPA overlayers observed in STM (Fig. 4.3) we performed complementary TPD experiments. Fig. 4.7 displays the corresponding spectra for desorbing H_2, H_2O, CO, CO_2 and O_2 molecules (thick lines) and various other masses (thin lines), together with the sequence of STM structures observed at the indicated temperatures. The H_2 mass spectra comprise three major desorption events for

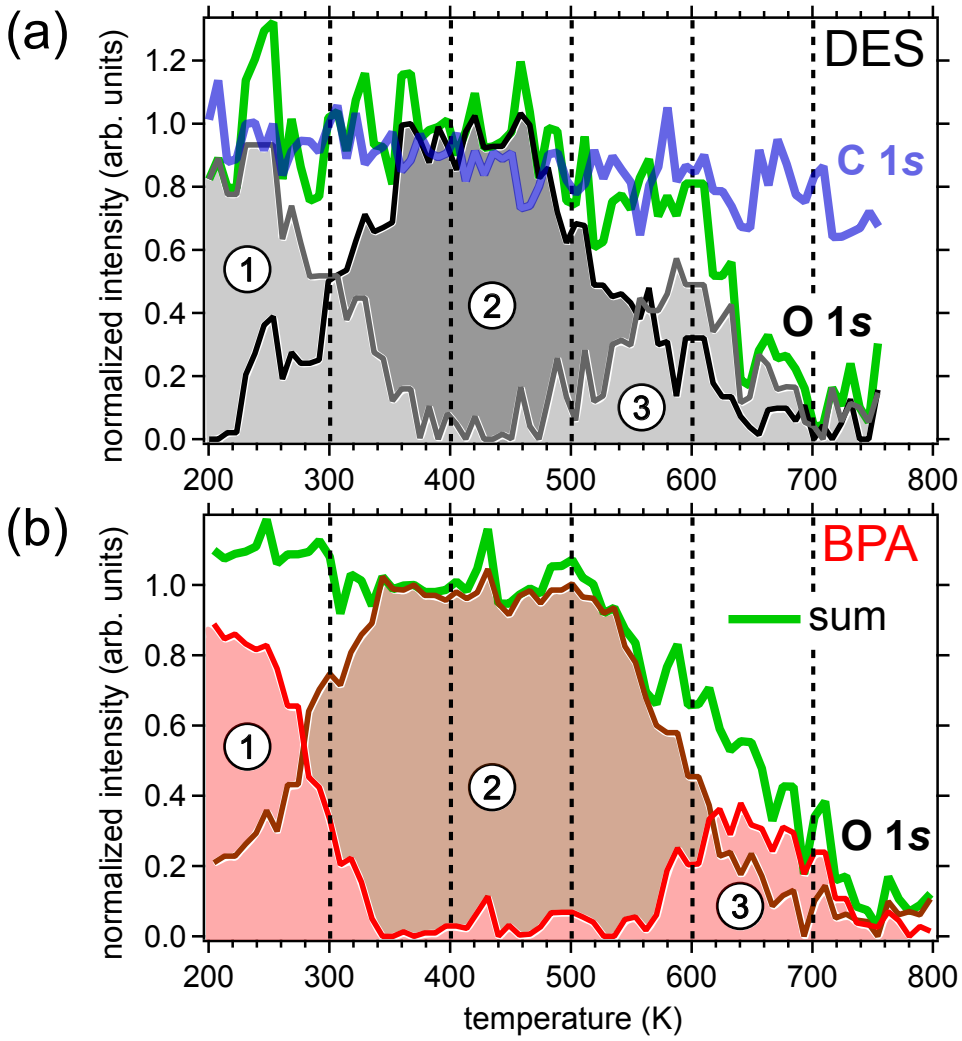

Figure 4.6: Integrated intensity of the individual O 1*s* components (labelled 1, 2 and 3 in the TP-XPS contour plots of Fig. 4.4) as a function of temperature: (a) DES/Cu(111); (b) BPA/Cu(111). To evaluate the O 1*s* intensities, the XP spectra were fitted with two Gaussians on a linear background, whereby one of the Gaussian functions covers the binding energy region of peak 1 and 3, and the other is constrained to the binding energy regime of feature 2. The intensities are then determined by integrating the area under the Gaussian fits. The sum of the O 1*s* intensities is displayed in green. For DES, the C 1*s* integrated intensities from the TP-XPS plot of Fig. 4.5a are also shown (blue line).

both molecules. The first feature peaks at about 320 K, in both cases, and is related to the deprotonation of the hydroxyl groups. This is evidenced by the transition from component 1 to component 2 in the XPS data of Fig. 4.4. We thus infer that the chemisorbed hydrogen, originating from deprotonation, desorbs from the surface as H_2 at ∼320 K. This provides good agreement with previous studies of hydrogen on Cu(111) [103] after heating rate recalibration [104]. The corresponding STM insets, taken after prolonged annealing to temperatures just above this first H_2-desorption feature, show the hexagonal structures described above, which are thus assigned to completely deprotonated hydroxyl species.
The second H_2-desorption feature at ∼430 K, in contrast to the first peak at 320 K, does not come along with any visible change in the O 1*s* core level (cf. Fig. 4.4 and 4.6). Nevertheless, the corresponding STM images after annealing to 460 - 470 K show that, both for DES and BPA, the transition from well-ordered overlayer into branched molecular chains has already taken place. Moreover, in the C 1*s* XP spectra (Fig. 4.5b) a distinct change of the line shape is detected between annealing to 385 K and 520 K. As the TPD spectra – apart from the desorption of molecules detected as fragments (cf. m/z ratios from 41 to 83 in Fig. 4.7) – do not show any desorption of O_2, CO, CO_2 or H_2O, we infer that this second reaction step does not involve any chemical change of the carbonyl species. Instead, we propose the H_2 desorption to stem from a hydroxy-directed *ortho-ortho* coupling, as described by Li et al. [20] and in section 4.1.
Finally, the third H_2 peak, centered at ∼500 K for DES and ∼600 K for BPA, comes along with the desorption of water. In the respective temperature regions, the O 1*s* signatures change again (cf. Fig. 4.4), with the carbonyl species being replaced by a new, weaker feature at a binding energy of 533.6 eV. While the H_2O desorption can account for the global loss of O 1*s* intensity, it is noteworthy that no O_2 desorption takes place at this stage. Furthermore, the almost unchanged C 1*s* intensity (cf. Fig. 4.5a and Fig. 4.6a) and the absence of desorbing high mass fragments in Fig. 4.7 indicate that no molecular desorption occurs in parallel with the water and dihydrogen desorption for DES. Also note that CO desorption, signaling degradation of the adsorbed species, takes place only above 600 K. The origin of the chemical shift in the O 1*s* spectra in this third reaction step is not immediately evident, and its rationalization will be discussed below.

The combination of XPS, TPD and STM data allows us to elucidate in detail the sequence of chemical transformations that DES and BPA undergo on the Cu(111) surface, leading from adsorbed monomers to conjugated polymers. The XPS measurements give evidence of a first deprotonation reaction, involving O-H bond cleavage, which starts at about 250 K. A 1:1 intensity ratio for the OH to carbonyl O 1*s* component is reached at ∼280 K for BPA, and at ∼300 K for DES (cf. Fig. 4.6). With the help of the TP-XPS data in Fig. 4.6, the corresponding activation energy (OH → carbonyl) was estimated to be ∼0.12 eV [104, 105] and is in good agreement with typical values (0.1 - 0.2 eV) for O-H bond breaking on surfaces [106–108]. The detached hydrogen atoms remain

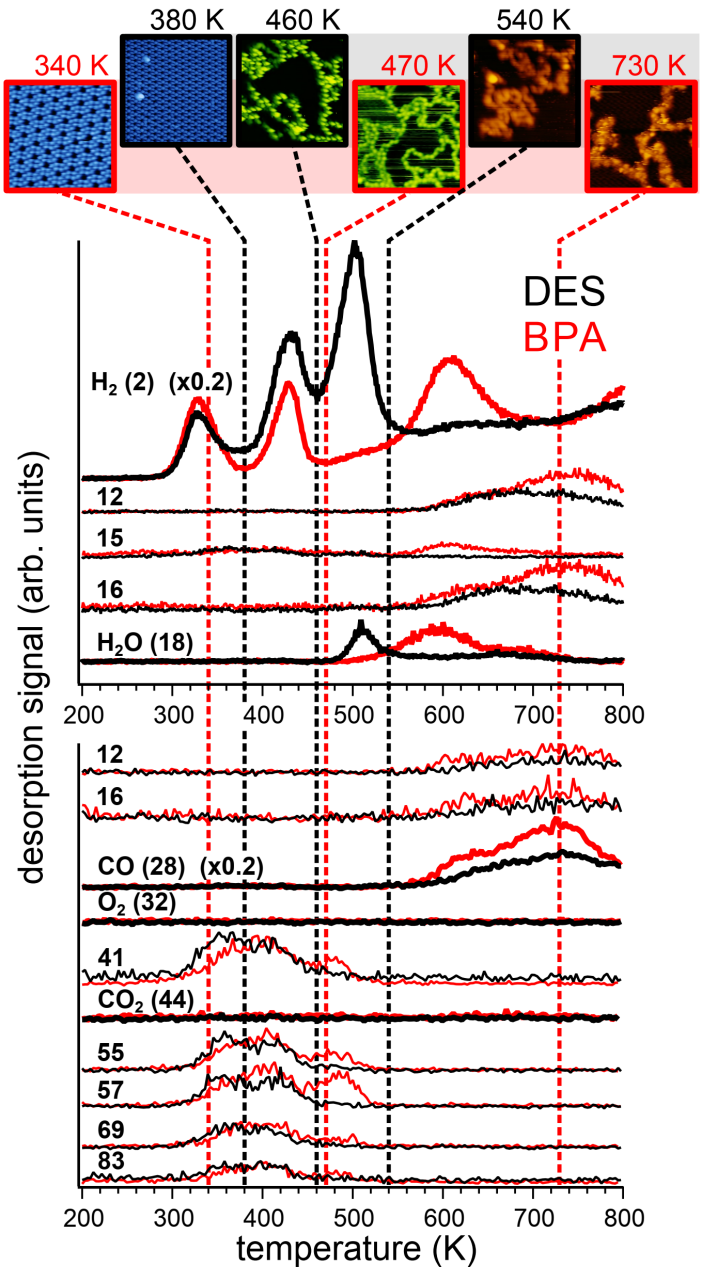

Figure 4.7: TPD measurements of DES/Cu(111) (black) and BPA/Cu(111) (red), at $0.5\,\mathrm{K\,s^{-1}}$ heating rate and after molecular deposition onto Cu(111) held at 200 K. H_2 (m/z=2) and CO (m/z=28) signals are scaled down by a factor 0.2 and the curves (labelled by their mass-to-charge (m/z) ratio) are vertically stacked for clarity. Quantitative comparison of the intensities of top and bottom TPD curves is not possible, as different mass spectrometer electronics were used to cover two different mass ranges. To facilitate data interpretation, the STM images of Fig. 4.3 are shown in the insets.

initially chemisorbed on the surface, from which they desorb at approximately 320 K upon recombination into dihydrogen. For both BPA and DES, analysis using the Arrhenius rate law provides a hydrogen desorption energy close to (or slightly lower than) 1 eV [104, 105]. This compares reasonably with a previous study of chemisorbed hydrogen on Cu(111), where values in the range 0.7 - 0.9 eV were determined [103]. The ordered overlayer structures observed in STM and LEED after annealing to 380 K and 340 K are, therefore, attributed to the deprotonated DES and BPA molecules (Fig. 4.8, step I), respectively. Based on Ref. [20] we propose that in this temperature regime the generated phenoxyl species undergo *enol-keto* tautomerization, which lowers the activation energy for C-H bond scission of an adjacent C atom in *ortho* position. The resulting C-H activation leads, subsequently, to *ortho-ortho* coupling between neighboring molecules (Fig. 4.8, step II) and desorption of dihydrogen as indicated by H_2-TPD (peak at ∼430 K for both BPA and DES). This proposed pathway is supported by the absence of desorption of any O-containing molecular fragments as well as of chemical shifts in the O 1*s* core level between 400 and 500 K, implying that oxygen is not directly involved in the coupling reaction. Evidence for the polymerization is additionally provided by the corresponding STM micrographs, where chain-like structures with clearly identifiable molecular features are imaged.

As to the third peak in the H_2-TPD, the chemical structure at the beginning of the desorption event is obviously not well defined (see STM images, Fig. 4.3), which renders the interpretation more complicated. Nonetheless, we can speculate about dominant reaction scenarios compatible with our experimental findings. Notably, the different structure of the DES and BPA precursor molecules (and more specifically, the different moiety bridging between the phenol groups) seems to play a role, as reflected in the different onset of the chemical transformations highlighted by the TPD and XPS data. Therefore, we need to treat the two cases separately. Starting from DES, we note that at about 510 K H_2 desorption is accompanied by the release of water. At the same time, we observe in XPS that the carbonyl O 1*s* component 2 is progressively replaced by a new component, 3, at higher binding energy (cf. Fig. 4.4). Notably, as shown in Fig. 4.4c, the two components initially reach a 1:1 intensity ratio, whereas at higher temperature the carbonyl O 1*s* component loses further intensity. A possible rationale for these observations is the formation of a C-O-C linkage between a carbonyl oxygen and an ethyl from the bridge group of an adjacent species (Fig. 4.8, red ellipse). This would indeed explain the relatively high binding energy (∼533.6 eV) of the new O 1*s* component, close to that reported for ethers [109, 110], as well as the desorption of H_2. One could further speculate that some abstracted hydrogen may trigger deoxygenation processes by preceding nucleophilic addition to the carbonyl oxygen, which is compatible with both the loss of O 1*s* intensity in XPS and the absence of desorbing O_2 in TPD. Additional dihydrogen desorption might also originate from C-C bond formation within the disordered polymers. This picture is, inevitably, oversimplified. As observed in the STM images, a clear atomistic descrip-

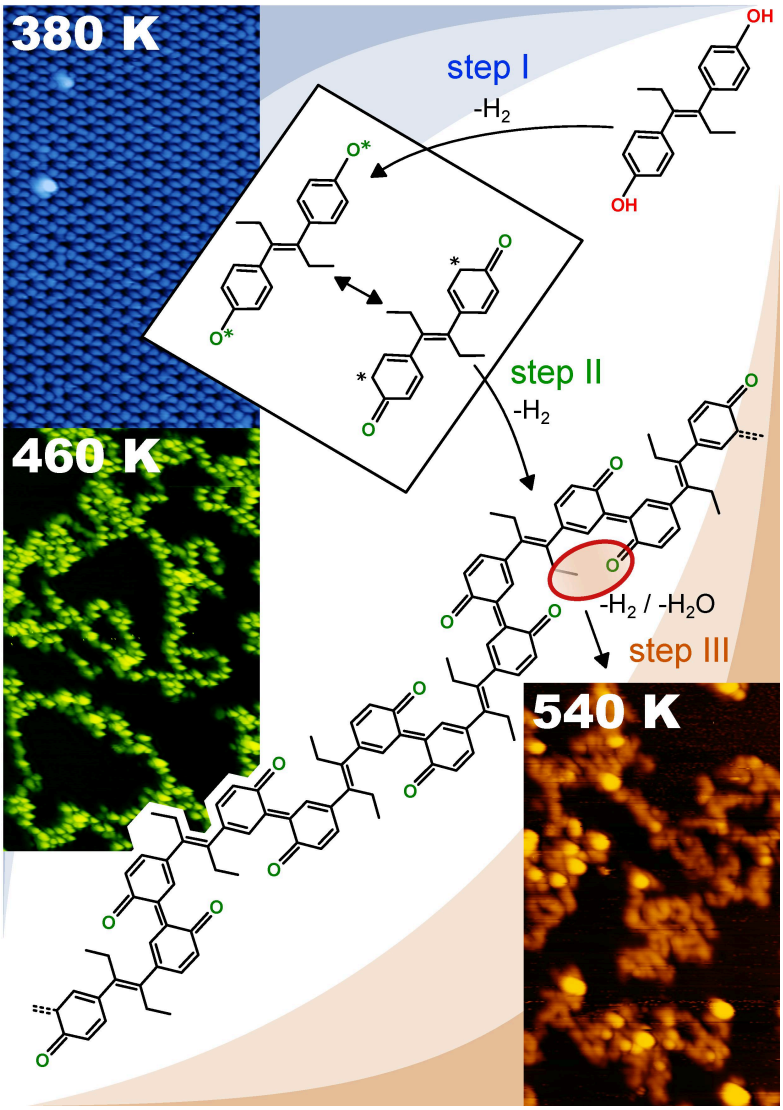

Figure 4.8: Proposed sequence of thermally activated chemical reactions of DES on Cu(111): tentative (simplified) structural models along with the corresponding STM images from Fig. 4.3 (due to the system's complexity, no structural model is presented for the outcome of step III).

tion is not possible, also considering that the non-planarity of the molecules hampers sub-molecular resolution in scanning probe microscopy studies; moreover, many different reactions are likely to happen simultaneously, resulting in a blurring out of the molecular appearance and loss of regularity. Nonetheless, the proposed pathway provides a rationale for the main findings in the XPS and TPD data (e.g. the appearance and persistence of component 3 in the O 1*s* XP spectrum, and the simultaneous desorption of H_2 and H_2O). In addition, the approximately 100 K higher temperature required for the third reaction step of BPA can be intuitively explained in terms of its different molecular structure, which does not easily allow formation of a C-O-C linkage (cf. Fig. 4.9), thus resulting in a retarded and generally weaker component 3 in XPS. Overall, we can exclude that the third H_2 peak in Fig. 4.7 arises from a second *ortho-ortho* coupling reaction, as proposed on Au(111) by Li et al. [20] to explain the formation of porous networks from phenol derivatives. Instead, only *monoselective* C-C coupling takes place on Cu(111) (similarly to Ag(111) [20]), followed by C-O-C formation and, further, oxygen removal.

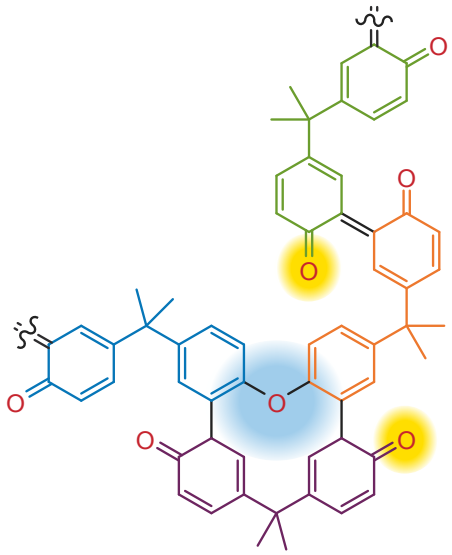

Figure 4.9: Tentative structural model of a BPA-derived polymer fragment featuring a C-O-C linkage, highlighted in blue. In yellow, other potential functional groups for such linkages are indicated, showing that further reaction in this configuration might be hindered. The BPA monomers are drawn with different colors.

4.4 Conclusion

Our analysis, combining real-space imaging with spectroscopic methods, enables us to disentangle the sequence of surface-assisted reactions that the BPA and DES molecules

undergo on the Cu(111) surface. Remarkably, despite being usually regarded differently concerning their toxicity (DES is a known teratogen, BPA is an industrial chemical), both molecules appear to follow a very similar reaction pattern. We find that the initial deprotonation of the phenols is followed by *enol-keto* tautomerization mediated *monoselective ortho* C-H activation. After a first polymerization step (C-C coupling), the molecules presumably form C-O-C bridges and deoxygenate upon further heating, leaving a network of branched, polymer-like chains on the Cu(111) surface.

From a methodological point of view, the combination of TPD with the chemically specific TP-XPS technique provides in-depth insight into the occurrence of surface-assisted chemical reactions, by monitoring both volatile desorbing products as well as the chemical identity of products that remain adsorbed on the surface. Combined with real-space imaging (e.g. STM), this information enables an advanced description of on-surface reactions on a sub-molecular scale. This approach can therefore be very valuable for the understanding and the control of the formation of sophisticated organic nanostructures at surfaces.

5 Iron Phthalocyanine on Ag(111) – the Surface as *Trans*-Ligand

This chapter includes content that has been published in

P. S. Deimel, R. M. Bababrik, B. Wang, P. J. Blowey, L. A. Rochford, P. K. Thakur, T.-L. Lee, M.-L. Bocquet, J. V. Barth, D. P. Woodruff, D. A. Duncan, and F. Allegretti, **"Direct quantitative identification of the "surface *trans*-effect"**," Chemical Science, vol. **7**, no. 9, pp. 5647–5656, 2016 – published by The Royal Society of Chemistry; this article is licensed under a Creative Commons Attribution 3.0 Unported Licence. Reproduced by permission of The Royal Society of Chemistry.

Theoretical calculations and corresponding images have been made by

R. M. Bababrik, B. Wang and M.-L. Bocquet

The strong parallels between coordination chemistry and adsorption on metal surfaces, with molecules and ligands forming local bonds to individual atoms within a metal surface, have been established over many years of study. The recently proposed "surface *trans*-effect" (STE) appears to be a further manifestation of this analogous behaviour, but so far, the true nature of the modified molecule-metal surface bonding has not been fully clarified. The STE could play an important role in determining the reactivities of surface-supported metal-organic complexes, influencing the design of systems for future applications. However, the current understanding of this effect is incomplete and lacks reliable structural parameters with which to benchmark theoretical calculations. In this chapter, using X-ray standing waves, we demonstrate that the ligation of ammonia and water to iron phthalocyanine (FePc) on Ag(111) distinctly increases the adsorption height of the central Fe atom. Moreover, we show that dispersion corrected density functional theory calculations can accurately model this structural effect. Importantly, the calculated charge redistribution in the FePc/H_2O electronic structure induced by adsorption is shown to involve accumulation of charge along the σ-bonding direction between the surface, the Fe atom and the water molecule, in a similar way as the redistribution caused by ammonia. This apparent σ-donor nature of the observed STE on Ag(111) involves bonding to the delocalised metal surface electrons rather than local bonding to one or more surface atoms, thus implying that this is a true surface *trans*-effect.

5.1 Introduction

The wealth of research of the last four decades into the adsorption of molecules and molecular ligands on metal surfaces [111–123] has demonstrated the strong similarity between the behaviour of these molecule-metal interactions and those found in metal coordination compounds. In particular, the local bonding of molecules to metal substrates has been found to commonly reflect the local atomic, rather than the delocalised metallic character of the surface [119, 120, 124]. Recently, spectroscopic measurements on the adsorption of planar metallo-complexes on metal surfaces [21, 22] have been interpreted as evidence for one further example of this analogue behaviour, namely the well-known *trans*-effect in metal coordination chemistry. Here we aim to provide quantitative structural measurements that clearly demonstrate that this surface induced *trans*-effect does indeed occur in one such system, but, contrary to expectations of a local atomic effect, the results of complementary density functional theory (DFT) calculations by R. M. Bababrik, B. Wang and M.-L. Bocquet show that this is a true surface effect. Specifically, we show that although the charge redistribution associated with the effect mimics that of bonding to a single atom in a coordination compound, the molecule bonds not to a single localised surface atom, but rather to the metal surface as a whole.

The study of metal-organic complexes on metal surfaces, and the way in which the substrate influences their interaction with ligand species, is an important field of research which is motivated by the desire to design future catalysts and molecule-based devices [21, 23, 125–137]. Of particular relevance are metal-supported porphyrins and phthalocyanines [128, 129], a class of molecules with a tetrapyrrole macrocycle that can act as a chemical cavity. Into this cavity a wide variety of metal cations can be coordinated, providing these molecules with diverse functional properties for a broad range of applications in, e.g., highly selective heterogeneous catalysts [23, 130, 131], molecular magnets [132, 133], molecular motors [134], spintronics [135, 136] and gas sensors [21, 137]. Despite the large body of work, however, the physical understanding and control of the processes that occur at the interface with metal supports are not yet fully developed. So far, most studies conducted on these organic/metal interfaces have provided qualitative information, most prominently using scanning tunnelling microscopy (STM) (e.g. Refs. [21, 134, 138, 139]) and X-ray photoelectron spectroscopy (XPS) (e.g. Refs. [21–23, 131, 139]). Theoretical calculations have also been performed, but comparisons of STM images with simulated images obtained from DFT calculations do not provide unique structural solutions despite being widely exploited for this purpose. The long-standing controversy concerning the structure of the Ag(111)/p(4x4)-O phase illustrates this problem [140, 141]. Moreover, DFT calculations indicate that chemical shifts in the photoelectron binding energy of core-level orbitals do not provide a unique indicator of adsorption sites and coordination environment [142]. By contrast, quantitative structural measurements can provide a relatively unambiguous benchmark against which theoretical predictions can be tested [122, 143].

One particular phenomenon that has been reported recently in this field is a significant electronic or chemical change in adsorbed metallo-porphyrin (MP) and metallo-phthalocyanine (MPc) based species after the addition of small molecular ligands to the metal centre [22]. This phenomenon has been referred to as surface *trans*-effect, in analogy with the traditional *trans*-effect in coordination chemistry [144–146]. The influence of this phenomenon can have repercussions across a wide variety of fields that utilise such supported metal-organic complexes [132, 147–150]. Of particular note is the influence it has on gas sensors: e.g. in the utilisation of iron phthalocyanine supported on graphene, exposure to nitric oxide apparently results in partial electron-doping of the graphene layer, manifesting as a decrease in the conductance of the system [151]. The surface *trans*-effect may also be the cause of the muted reactivity typically observed for MPs and MPcs on metal substrates [23], where the interaction between the molecules and the surface appears to prevent reaction pathways that are available to the molecule when dissolved in a solvent.

The prototypical system, when MP and MPc molecules are adsorbed on a metallic substrate, typically has the central molecular macrocycle orientated (approximately) parallel to the substrate plane [152, 153]. It is this adsorption geometry that leaves the centrally coordinated metal ion close to the substrate, but also free to interact with potential ligand molecules at the position *trans* to (i.e. opposite to) the substrate. Flechtner et al. [21] reported that, when cobalt tetraphenylporphyrin (Co-TPP) was adsorbed onto Ag(111), a significant difference in Co $2p$ photoelectron binding energy was observed in XPS between single-layer and multilayer samples. However, this energy difference was greatly reduced following exposure to NO. This experimental finding was tentatively ascribed to a weakening of the interaction between the metal centre of the porphyrin and the substrate, caused by the ligation of NO at the position *trans* to the substrate. This was interpreted as being, at least phenomenologically, similar to the traditional *trans*-effect, in which a ligand with an intense *trans*-effect, either through being a strong σ-donor or π-acceptor, weakens the ligand-metal bond that is *trans* to it. In Fig. 5.1, a phenomenon associated with the traditional *trans*-effect is illustrated by a hypothetical scheme. Specifically, a ligand with an intense *trans*-effect, NO, replaces an NH_3 molecule (cf. Fig. 5.1a and b), weakening the NH_3-metal bond that is *trans* / opposite to it, and thus promoting the replacement of this ammonia molecule by a second ligand (cf. Fig. 5.1b and c). A consequence of this is that an intense *trans*-effect ligand induces a longer metal-ligand bond length at the *trans* position (cf. Fig. 5.1b), whereas a milder *trans*-effect ligand results in a shorter metal-ligand bond at the *trans* position (cf. Fig. 5.1c). Similarly, when dealing with octahedral coordination, as in the case of molecular ligation to phthalocyanines and porphyrins, if molecular ammonia is replaced by molecular water, a ligand with an even milder *trans*-effect than ammonia, this replacement will lead to a shortening of the bond length of the remaining ammonia molecule that is *trans* to it (cf. Fig. 5.2a and b). In the proposed surface *trans*-effect, the surface plays the role of one of the ligands, not

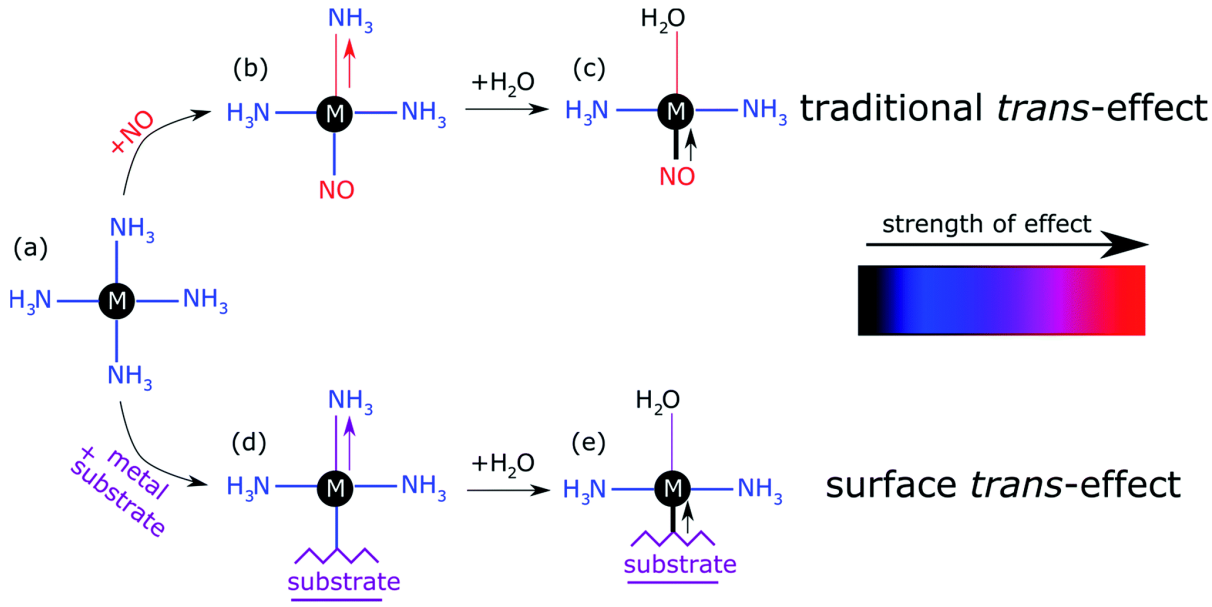

Figure 5.1: Schematic illustration of the traditional *trans*-effect and the surface *trans*-effect for a hypothetical system, assuming that the intensity of the effect increases from $H_2O < NH_3 <$ metal substrate $< NO$ (indicated with the colour scheme). Specifically, a general case of (a → b → c) the traditional *trans*-effect is illustrated, where a ligand with a moderately intense *trans*-effect is replaced, sequentially, by a ligand with (a → b) a more intense and (b → c) a less intense *trans*-effect; the associated change in M-ligand bond length is highlighted by the arrows. Also shown is a hypothetical case of (a → d → e) the surface *trans*-effect, where a ligand with a moderately intense *trans*-effect is replaced, sequentially, by a metal substrate with (a → d) a more intense *trans*-effect and a ligand with (d → e) a less intense *trans*-effect; the associated changes in M-ligand bond length and M-substrate adsorption height (respectively) are indicated. A comparable, more realistic case of the surface *trans*-effect is shown in Fig. 5.2c and d for an octahedral complex.

only inducing a *trans*- (or *trans*-like-) effect, as shown in Fig. 5.1d and Fig. 5.2c, but also experiencing a *trans*- (or *trans*-like-) effect, as shown in Fig. 5.1e and Fig. 5.2d. This

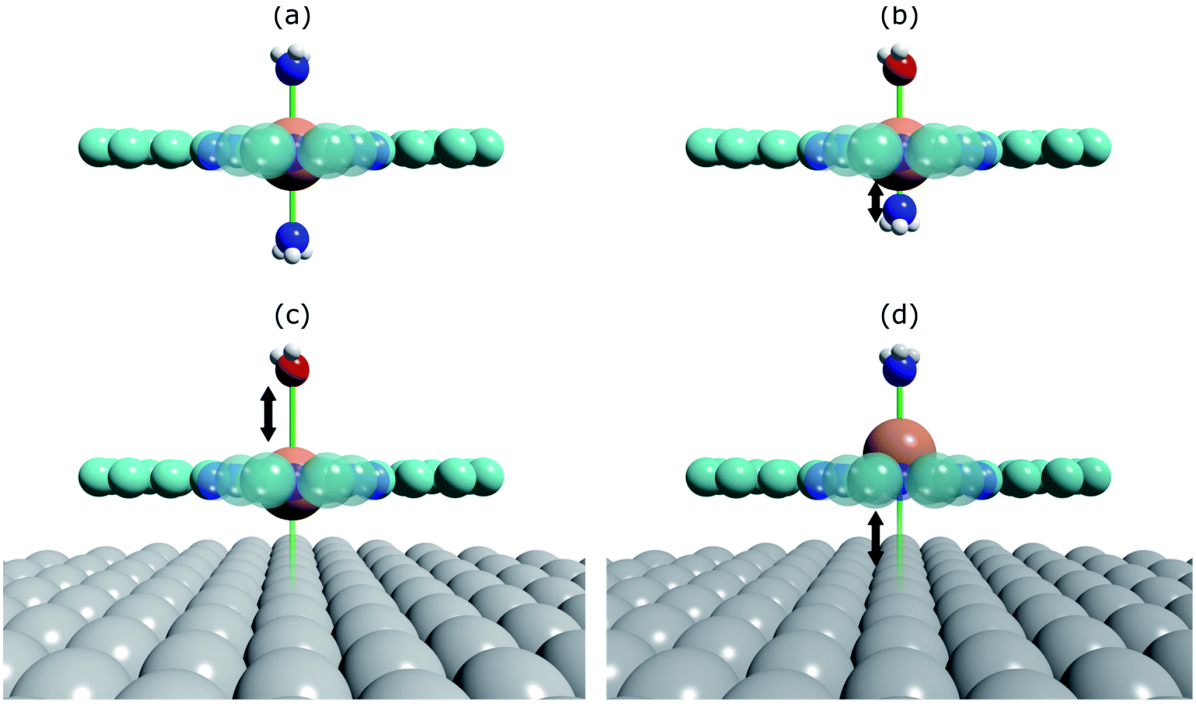

Figure 5.2: Schematic view of the (surface) *trans*-effect for an octahedral complex of (a) (NH_3)–FePc–(NH_3), where two ammonia molecules are *trans* to each other, (b) (H_2O)–FePc–(NH_3), where the ammonia molecule is *trans* to a water molecule, (c) (H_2O)–FePc–Ag(111), where water is *trans* to the Ag(111) surface, and (d) (NH_3)–FePc–Ag(111), where ammonia is *trans* to the Ag(111) surface. Assuming the order of the intensity of the *trans*-effect goes: $H_2O < NH_3 <$ Ag(111), then the traditional *trans*-effect would suggest a shorter Fe–(NH_3) bond when ammonia is *trans* to a water molecule, than when it is *trans* to another ammonia molecule. Similarly, a longer Fe–(H_2O) bond would be expected when water is *trans* to the Ag(111) surface than to ammonia. Finally, this would also imply a larger adsorption height of the Fe centre when the Ag(111) surface is *trans* to ammonia than to water.

interpretation was tested by Hieringer et al. [22], who probed the interaction of Fe-TPP, Co-TPP and ZnTPP with NO on the Ag(111) surface, using ultraviolet photoelectron spectroscopy, XPS and STM, and qualitatively comparing the shifts in the Co $2p$ XPS binding energy with those obtained from DFT calculations. These DFT calculations predicted a significant structural displacement of the metal ion by >0.6/0.7 Å for Co and >0.4/0.7 Å for Fe (PBE / PBE+vdW). Since the original work of Flechtner et al. several other groups have observed various electronic and chemical effects that have all been at-

tributed to this "surface *trans*-effect" [23, 129, 132, 147–150, 154]. However, prior to our study, there have been no experimental investigations of the predicted structural changes, nor has there been a quantitative comparison of theoretical predictions to experimental results.

Here we present the results of such a quantitative experimental test of DFT predictions, utilising normal incidence X-ray standing waves (NIXSW) (cf. section 2.5) to measure the displacement of iron phthalocyanine (FePc - shown schematically in Fig. 5.4a), adsorbed on a Ag(111) single-crystal surface, before and after ligation of ammonia and water. The choice of the system was inspired by the results of a previously published investigation, predicting a 0.9 Å displacement of the iron centres of FePc on the Au(111) surface upon ligation of ammonia, by means of DFT calculations that did not include dispersion forces, and reporting experimentally observed electronic changes supportive of the "surface *trans*-effect" [155].

5.2 Experimental Details

The XSW measurements were performed at the I09 beamline at the Diamond Light Source (cf. section 3.2). The intensity and width of the (111) Bragg reflection of the Ag crystal was measured at normal incidence ($h\nu \approx 2640\,\mathrm{eV}$ at a Ag(111) sample temperature of $\sim$60 K). The Darwin reflectivity curve was used to define the energy scale with respect to the Bragg energy, the energy broadening due to imperfections in the monochromator (Si(111) double-crystal) and the mosaicity of the single crystal substrate (which was found to be negligible). The experimental chamber was orientated with either a 60° or 90° angle between the incident photon beam and the centre of the detector. The integrated intensities of the Fe 2*p*, N 1*s* and C 1*s* photoemission peaks were used to monitor the relative X-ray absorption of the Fe, N and C atoms, respectively. Both instrumental geometries led to similar values for the NIXSW fitting parameters once non-dipolar effects in the angular dependence of the photoemission were taken into account (cf. section 2.5.2). Specifically, the forward-backward asymmetry parameter Q was calculated theoretically using the average angle acquired on the analyser ($\theta_p = 30°$ and $\theta_p = 18°$, respectively, as defined in Ref. [156]). To minimise radiation damage to the adsorbed molecules, the sample was held at $\sim$60 K, and the X-ray beam (defocused to approximately $300\times300\,\mu\mathrm{m}^2$) was stepped over the sample during each XSW measurement, such that each energy point in a single scan was acquired from a different position on the sample. The base pressure in the end station was $\sim5 \times 10^{-10}$ mbar, which necessitated re-preparation of the sample every $\sim$8 hours to limit the adsorption of residual water in the vacuum. A clean Ag(111) crystal was prepared by repeated cycles of Ar^+ sputtering and annealing to 800 K for 25 minutes. A multilayer of FePc was deposited by sublimation of FePc powder (Sigma Aldrich, 90 % pure by dye content, triply purified [157]) at 680 K onto the sample held at room temperature. The latter was then annealed to $\sim$600 K for 40 minutes, desorbing

the excess FePc and resulting in a low-energy electron diffraction pattern consistent with a saturated incommensurate single-layer described by a matrix of $\begin{pmatrix} 4.80 & -0.40 \\ 2.58 & 5.68 \end{pmatrix}$ [158] (cf. Fig. 5.3d and e). This Ag(111)/FePc system was subsequently exposed to ammonia or water by backfilling of the chamber to pressures of 10^{-8} mbar with the substrate held at 60 K. Due to the placement of the ion gauge near the turbomolecular pump, at a significant distance from the sample, an accurate measure of the exposure rate was not possible; however the coverage of all exposures was monitored by XPS measurements (cf. Fig. 5.3f) and indicated in all cases a coverage of ammonia or water greater than around 1 molecule per 3 silver surface atoms ($\sim$0.33 ML), which is much higher than that required to saturate each Fe atom ($\sim$0.04 ML). Between $\sim$0.33 ML and $\sim$3 ML, no trend was observed in the variation of the height of the FePc molecules, as a function of ammonia (or water) coverage. At each stage of the preparation, XPS was utilised to monitor any possible contaminants, and with the exception of the aforementioned adsorption of residual water in the vacuum and damage caused by the X-ray beam after lengthy exposure, none were observed. For the data reduction of the XSW measurements, in all cases a Voigt lineshape was used to model the photoemission peaks, except for the broad Fe $2p_{3/2}$ multiplet structure towards higher binding energy, which was modelled with a Gaussian lineshape (cf. peak 2 in the XP spectrum in Fig. 5.3a). The backgrounds of the Fe $2p_{3/2}$ spectra were fitted using a template background (measured over the same energy range on the clean Ag(111) substrate), whereas Shirley backgrounds were used for the N 1*s* and C 1*s* spectra. For the N 1*s* spectra two additional Gaussians were also introduced in the fitting to compensate for the underlying Ag plasmons. Exemplary fittings of the three relevant core levels are displayed in Fig. 5.3a-c for a pristine FePc monolayer, and in Fig. 5.3f, which compares N 1*s* spectra before and after adsorption of ammonia.

Extensive DFT calculations were carried out by R. M. Bababrik, B. Wang and M.-L. Bocquet, using the VASP package [161]. The PBE-GGA exchange-correlation potential [162] was used, and the electron-core interactions were treated in the projector augmented wave method [163, 164]. The van der Waals (vdW) interaction has been taken into account through the so-called DFT-D2 and -D3 semi-empirical methods *via* a pairwise force field [165, 166] or by using a non-local optB88-vdW (DFT-vdW) exchange-correlation functional [167, 168]. All the calculations were performed using a four-layer Ag slab embedded in 15 Å of vacuum space, ensuring 10 Å separation between adjacent supercells. Structures were optimised using energies calculated at a single **k** point (the Γ point of the Brillouin zone) with a kinetic cut-off energy of 400 eV. The coordinates of the uppermost Ag layer and the molecules were fully relaxed until the atomic forces were smaller than 0.01 eV/Å. Furthermore, the presented results using the DFT-D2 method take into account the van der Waals interaction of all the layers (DFT-D2-4L) in the pairwise interaction [165]. The charge redistribution maps (CRMs) shown in Fig. 5.5 were calculated by

$$\Delta\rho = \rho(A+B) - \rho(A) - \rho(B) \ , \tag{5.1}$$

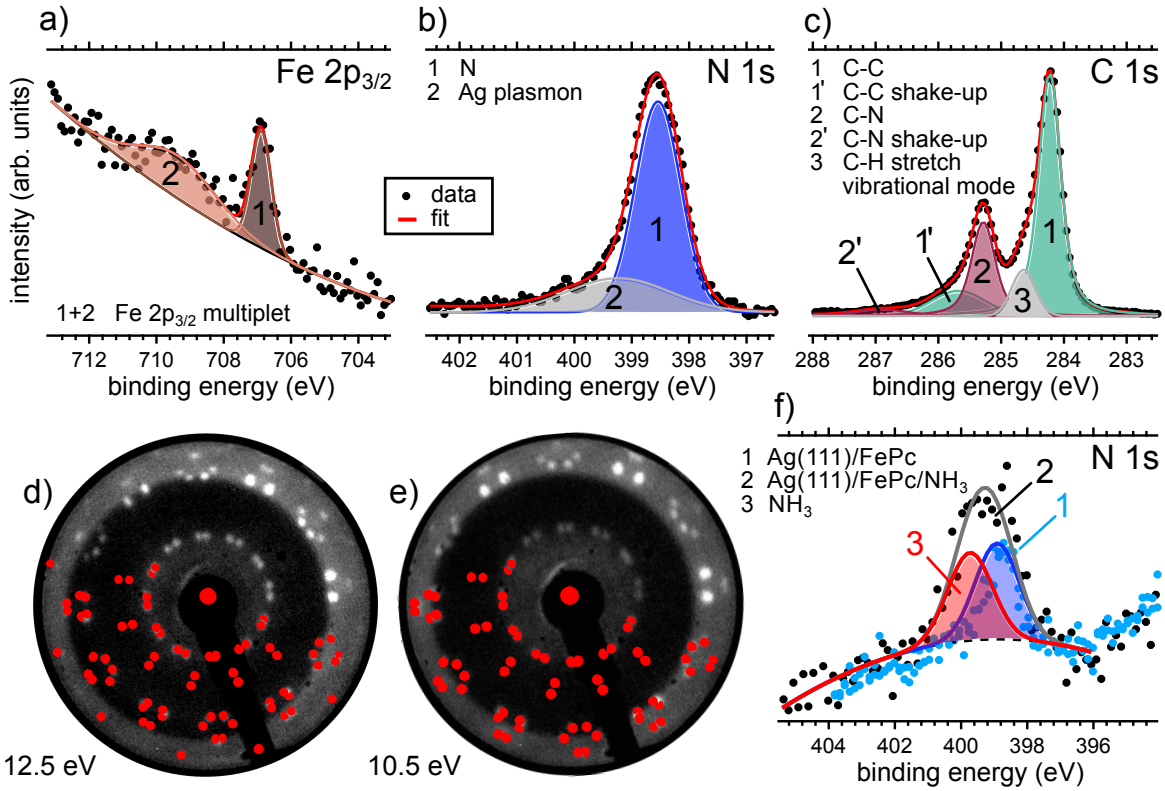

Figure 5.3: Exemplary XP spectra and LEED pattern of the FePc monolayer on Ag(111) (Ag(111)/FePc): a) Fe $2p_{3/2}$, b) N $1s$ and c) C $1s$ XP spectra measured from a FePc monolayer on Ag(111) at room temperature (RT) and with photon energies of $h\nu = 880\,\text{eV}$ (Fe $2p_{3/2}$), $h\nu = 550\,\text{eV}$ (N $1s$) and $h\nu = 435\,\text{eV}$ (C $1s$), respectively. Both the Fe $2p_{3/2}$ and the N $1s$ core levels partially overlap with bulk spectral features, specifically the tail of the Ag $3s$ feature (causing the descending background in the Fe $2p_{3/2}$ spectrum) and Ag plasmons (cf. peak 2 in the N $1s$ spectrum). The assignment of peaks in the C $1s$ spectrum follows that proposed by Papageorgiou et al. [159]. Here, the C $1s$ spectrum shows two main components, 1 and 2, which are related to the C atoms bonded to N (C–N) and the C atoms bonded only to C atoms (C–C). The N $1s$ spectrum contains only a single peak relating to all eight N atoms in the phthalocyanine molecule. The LEED pattern of the FePc monolayer on Ag(111) in d) and e), recorded at an electron energy (E_p) of 12.5 eV and 10.5 eV, respectively, corresponds to the saturated incommensurate single-layer ("superstructure I") described by Bobaru et al. [158]. The corresponding superimposed overlayer patterns (red dots in d) and e)) have been generated by means of the LEEDpat software utility [96]. f) N $1s$ XP spectra on Ag(111)/FePc, at ~60 K sample temperature and $h\nu \approx 2640\,\text{eV}$, before (1) and after (2) NH_3 exposure. Spectrum 2 corresponds to the lowest NH_3 exposure considered in the study and can be reproduced by fitting with an NH_3-component (3) at ~399.7 eV [160] of almost equal intensity as the N $1s$ feature ascribed to the FePc single-layer.

which is the electron density of the whole system $\rho(A+B)$ minus the electron density of each component, $\rho(A)$ and $\rho(B)$, with the atomic positions of A and B fixed in the optimized structure $(A+B)$. For example, [NH_3/FePc/Ag(111)] describes the total electron density for NH_3 on FePc on Ag(111), and [FePc/Ag(111)] and [NH_3] are representing the electron density of both FePc adsorbed on Ag(111) and NH_3, with their atoms fixed at the optimized adsorption positions for [NH_3/FePc/Ag(111)]. Thus, [NH_3/FePc/Ag(111)]-[FePc/Ag(111)]-[NH_3] simply displays the charge redistribution caused by the adsorption of NH_3 on FePc/Ag(111).

5.3 Results and Discussion

The XSW absorption profiles, monitored by Fe $2p_{3/2}$ photoemission from a single-layer of adsorbed FePc, both before and after exposure to ammonia or water, are displayed in Fig. 5.4b and show a clear shift of the maximum of the profile to lower photon energies following molecular uptake. This shift indicates that there is an increase in the coherent position, and thus in the height of the adsorbed Fe atom above the Ag(111) surface, caused by molecular ligation. Specifically, the results presented in Fig. 5.4b indicate that the Fe atom is at its lowest position prior to ligation, at its highest position when ligated to ammonia, and at an intermediate position when ligated to water. Quantitative analysis of the absorption profiles yields a change in the average height of the Fe atom by $+0.19\pm0.07$ Å after the adsorption of ammonia, and by $+0.07\pm0.04$ Å after the adsorption of water. Similar effects, though significantly smaller, were observed for the absorption profiles recorded for the carbon and nitrogen atoms, as shown schematically in Fig. 5.4c and detailed in Table 5.1a, indicating that there is a shift (but not a rigid one) of the whole molecule to greater heights above the surface. The corresponding coherent positions, coherent fractions and absolute heights are shown in Table 5.1b.

The atomic displacements predicted by DFT calculations are reported in Table 5.2. The results from the DFT-D2 calculations agree extremely well with the experimental XSW results. The DFT-D3 calculations significantly overestimated the effect of ammonia ligation, most notably to the Fe metal centre. The DFT-vdW calculations using optimised exchange energy also show results comparable to the experiments.

In contrast, theoretical calculations without van der Waals corrections predict a significantly larger displacement of the entire molecule than is experimentally observed. However, the qualitative trends, e.g. a smaller displacement due to water adsorption and a smaller displacement of the molecular backbone than of the Fe atom, are reproduced. Inclusion of van der Waals corrections into the calculations decreases the size of the displacement dramatically for both ligands, bringing the theory into excellent quantitative agreement with the experimental measurements.

The observed displacement of the Fe centre of FePc is qualitatively consistent with the results of the DFT calculations of Hieringer et al. [22]; the weakening of the metal centre

Table 5.1: Quantitative structural results for FePc on Ag(111) before and after ligation to NH_3 and H_2O: a) experimental displacements in the FePc height (in $\mathring{A}$) above the surface for the Fe, N and C atoms (C is split into C–C and C–N species as identified in Fig. 5.3c) upon ligation of NH_3 (Ag(111)/FePc/(NH_3)−Ag(111)/FePc) and H_2O (Ag(111)/FePc/(H_2O)−Ag(111)/FePc). The number in brackets is the uncertainty (standard error at two standard deviations) in the last decimal place. b) The corresponding experimentally determined coherent fractions (f_{coh}) and coherent positions (D), as well as the height of the various species above the bulk like termination of the Ag(111) surface. Note: d_{hkl} for Ag(111) is taken as 2.35 Å, and it is assumed that the molecule lies over one layer spacing above the surface (otherwise unphysical results are obtained for bond lengths).

a)

	Ag(111)/FePc/(NH_3)−Ag(111)/FePc				Ag(111)/FePc/(H_2O)−Ag(111)/FePc			
	Fe	N	C–N	C–C	Fe	N	C–N	C–C
XSW ($\mathring{A}$)	0.19(7)	0.13(7)	0.07(6)	0.06(6)	0.07(4)	0.08(9)	0.01(2)	−0.02(5)

b)

	Ag(111)/FePc			
	Fe	N	C–N	C–C
f_{coh}	0.9(1)	0.87(5)	0.9(1)	0.9(2)
D	0.11(1)	0.15(3)	0.20(2)	0.24(2)
$d_{hkl} + D \cdot d_{hkl}$ ($\mathring{A}$)	2.61(1)	2.71(7)	2.83(5)	2.92(5)

	Ag(111)/FePc/NH_3			
	Fe	N	C–N	C–C
f_{coh}	0.73(8)	0.9(3)	0.9(1)	0.95(11)
D	0.19(3)	0.21(1)	0.23(1)	0.27(1)
$d_{hkl} + D \cdot d_{hkl}$ ($\mathring{A}$)	2.80(7)	2.84(2)	2.90(3)	2.98(3)

	Ag(111)/FePc/H_2O			
	Fe	N	C–N	C–C
f_{coh}	0.75(7)	0.8(1)	0.9(1)	0.9(1)
D	0.14(2)	0.19(3)	0.21(1)	0.23(4)
$d_{hkl} + D \cdot d_{hkl}$ ($\mathring{A}$)	2.68(4)	2.79(6)	2.84(2)	2.90(1)

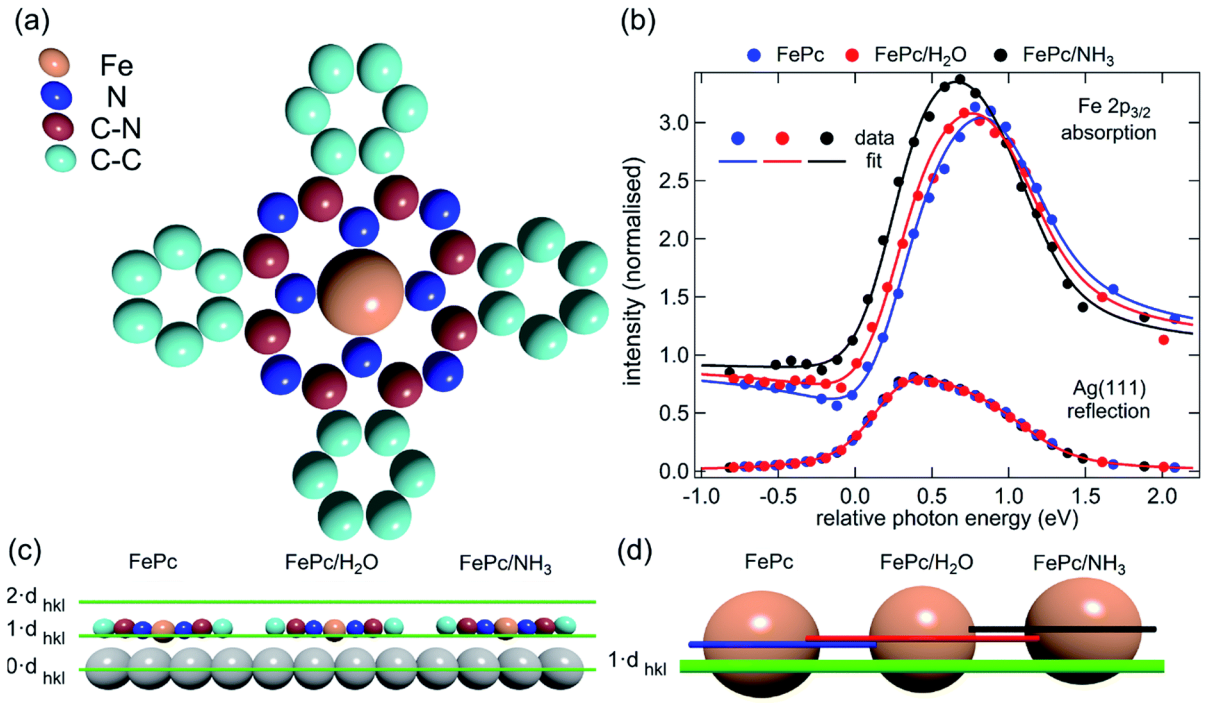

Figure 5.4: Experimental results from NIXSW measurements on FePc on Ag(111) before and after H_2O and NH_3 ligation: (a) Molecular structure of FePc. Note that the two different species of C, which could be chemically resolved in the XSW analysis according to the C 1*s* peaks in the XP spectrum in Fig. 5.3c, are assigned to C atoms bound to C and N atoms (C–N) and bound only to other C atoms (C–C). (b) Comparison of the Fe $2p_{3/2}$ X-ray absorption profiles before molecular ligation (FePc, blue), after water ligation (FePc/H_2O, red) and after ammonia ligation (FePc/NH_3, black). (c) A to scale schematic representation of the quantitative analysis of the XSW data detailed in Table 5.1. The atomic scattering plane at the surface termination ($0 \cdot d_{hkl}$), the first ($1 \cdot d_{hkl}$) and the second ($2 \cdot d_{hkl}$) extended planes above the surface are also indicated. Also shown (d) is a 4× magnification of the displacement of the Fe atoms, with horizontal lines indicating the centre of the Fe atoms above the first extended surface plane ($1 \cdot d_{hkl}$, green).

Table 5.2: Theoretical displacements for FePc on Ag(111) before and after ligation to NH_3 and H_2O: displacements (in $\AA$) above the surface (averaged over the molecule in an atop, bridge and hollow site) for the Fe, N and C atoms upon ligation of NH_3 (Ag(111)/FePc/(NH_3)–Ag(111)/FePc) and H_2O (Ag(111)/FePc/(H_2O)–Ag(111)/FePc).

	Ag(111)/FePc/(NH_3)−Ag(111)/FePc				Ag(111)/FePc/(H_2O)−Ag(111)/FePc			
	Fe	N	C–N	C–C	Fe	N	C–N	C–C
DFT ($\AA$)	1.10	0.82	0.78	0.51	0.15	0.06	0.05	0.01
DFT-D2 ($\AA$)	0.19	0.09	0.08	0.03	0.07	0.03	0.03	0.01
DFT-vdW ($\AA$)	0.22	0.12	0.11	0.06	0.04	0.02	0.02	0.02
DFT-D3 ($\AA$)	0.31	0.16	0.14	0.06	0.07	0.02	0.01	0.00

interaction with the metal substrate does indeed have a structural effect similar to that expected from the traditional *trans*-effect in coordination chemistry. It has long been established that adsorbates on metal surfaces follow rules comparable to those developed in coordination chemistry [119, 120, 169], so extending this analogous behaviour to metal-organic complexes adsorbed on metal surfaces may appear entirely reasonable. However, one should question the "surface *trans*-effect" terminology, because the comparison with metal coordination compounds effectively requires the surface to be considered not only as having an effect comparable to a ligand, but one whose interaction with the metal centre of the phthalocyanine has a specific directionality. In other words, to be physically a *trans*-effect the interaction cannot be mediated through long-range forces (e.g. induced dipoles or vdW forces), instead it must be induced through the sharing of an orbital of the metal centre by both the surface and the ligand *trans* to it, in order to satisfy either a σ-donor or a π-acceptor interpretation of the traditional *trans*-effect [144, 145]. The hybridisation of metal adatoms to metal surface atoms, when coadsorbed with molecules to form metal-organic coordination networks, has been proposed from theoretical calculations [170, 171]. However, it is not clear to what extent this is comparable to the interaction between the metal surface and the metal centres within adsorbed MP and MPc molecules. This raises the question: if it looks like the *trans*-effect, acts like the *trans*-effect, does it actually mean it is the *trans*-effect? In other words, is the term "surface *trans*-effect" merely a useful description of the observed phenomena in broad terms, or does it have actual physical meaning?

The overlayer studied here, a saturated single-layer of FePc on Ag(111), is known to be incommensurate with the underlying substrate (cf. Fig. 5.3d and e and Ref. [158]). However, the coherent fractions observed for the adsorbed molecule are relatively high (cf. Table 5.1b), indicating that the variation in the height of the molecules above the

surface is small, despite the local coordination of the Fe atom varying over an effective infinity of sites. If the Fe-substrate height were exactly the same throughout the incommensurate overlayer, the local Fe-Ag atomic distance would increase as the number of nearest neighbour Ag atoms increases (e.g. the distance is longer over a hollow site than over an atop site). This is qualitatively similar to what is observed for small molecular species when adsorbed in atop, bridge and hollow sites [119] on metal surfaces, an effect interpreted as following rules similar to those devised for coordination chemistry. However, this does not necessarily suggest that, if the interaction between the metal complex and the metal substrate follows the same general trend, then the $Fe_{ads} - Ag_{surf}$ interaction would also be comparable to that of the ligand to metal centre interaction in coordination chemistry. More generally, as there are effectively an infinite number of different local adsorption sites in the incommensurate layer, it is clear that most Fe atoms will not be directly above a Ag atom, so there will not be a silver atom in a site *trans* to the adsorbed molecular ligand; in contrast, the traditional *trans*-effect clearly suggests a strong directional influence. This implies that, if the "surface *trans*-effect" is indeed a *trans*-effect, the substrate to metal complex interaction cannot be mediated by direct interaction to the silver atoms. Instead, it must be the delocalised metal surface electrons that drive the effect.

To try to address these issues and encouraged by the good quantitative agreement between the theory and the experiment in reproducing the structural consequences of this "surface *trans*-effect", R. M. Bababrik, B. Wang and M.-L. Bocquet conducted calculations for a number of simple model structures. Specifically, calculations (DFT-D2) were performed on the traditional *trans*-effect systems (NH_3)-FePc-(NH_3), (H_2O)-FePc-(H_2O), (NH_3)-FePc-(H_2O) and (NH_3)-FePc-(NO). Comparing these calculations to the relevant Ag(111)/FePc calculations, the Ag substrate (for Fe sitting on top of a surface Ag atom) induces a bond length between the *trans*-ligand and the Fe atom of 2.12 Å (N-Fe) and 2.40 Å (O-Fe) for NH_3 and H_2O, respectively. These bond lengths are significantly longer than the bond lengths induced by H_2O (namely 1.99 Å (N-Fe) and 2.04 Å (O-Fe) for NH_3 and H_2O in *trans* position, respectively) and NH_3 (namely 2.03 Å (N-Fe) and 2.09 Å (O-Fe) for NH_3 and H_2O in *trans* position, respectively), but shorter than induced by NO (namely 2.16 Å (N-Fe) for NH_3 in trans position). This difference in bond length would place the silver surface as having a potential *trans*-effect somewhere between the weak (water, ammonia) and the strong (NO) ligands. When charge redistribution maps (CRMs) are compared (cf. Fig. 5.5), it can be seen that the effects on the Fe centre of introducing the Ag surface (cf. Fig. 5.5a) or an NH_3 ligand (cf. Fig. 5.5b) *trans* to a water molecule are remarkably similar. In both cases there is significant redistribution of charge into the σ-bonds that lie between the introduced species (Ag(111) / NH_3) and the Fe centre, while a smaller increase in charge density occurs between the O and Fe atoms. This is mostly manifest as an accumulation of charge density in the Fe d_{z^2} orbital and a comparable decrease in the Fe d_{xz} and d_{yz} orbitals. Introducing an NH_3

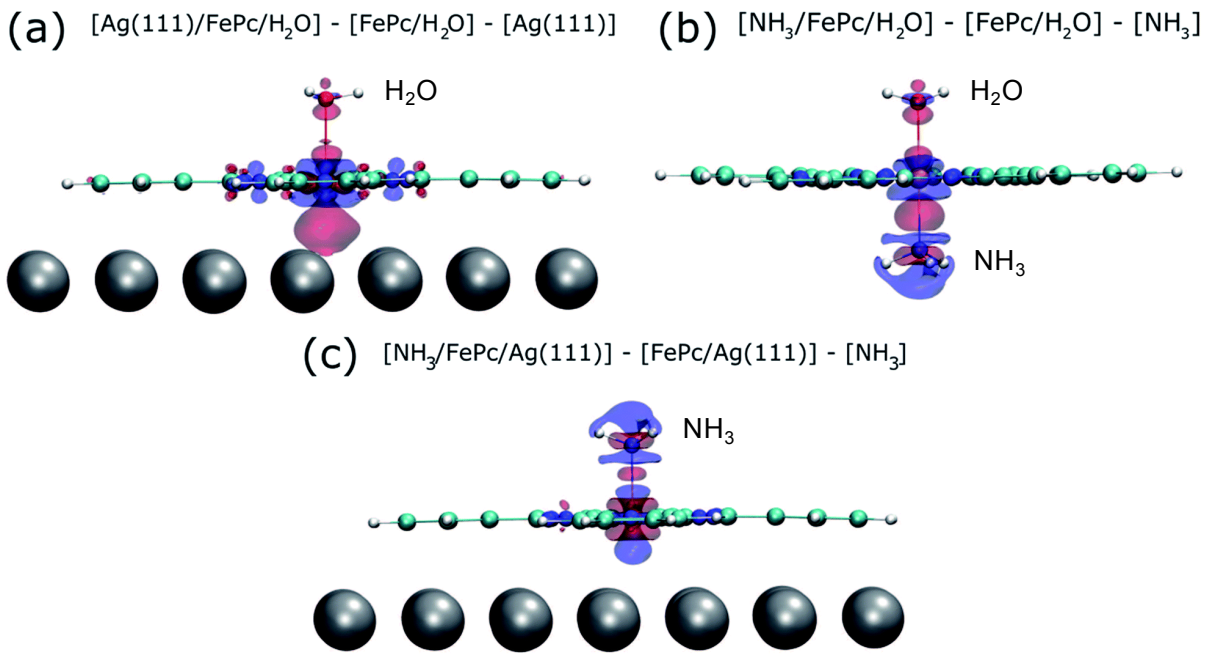

Figure 5.5: Charge redistribution map (CRM) illustrating the effect of adding Ag surface, NH_3 and H_2O *trans* to each other, showing an isosurface plot with ± 0.02 e $\mathring{A}^{-3}$ (red is an increase, blue a decrease in charge density). Shown is (a) the difference caused by adding the Ag(111) surface *trans* to a water molecule, (b) by adding ammonia *trans* to a water molecule and (c) by adding ammonia *trans* to the Ag(111) surface. In (a) and (c) the Fe atom is assumed to be sitting above a hollow site of the Ag(111) surface.

ligand (cf. Fig. 5.5c) *trans* to the Ag(111) substrate has an effect on the NH_3 species similar to when it is introduced *trans* to a water ligand (cf. Fig. 5.5b). However, Fig. 5.5c shows that the opposite effect occurs at the Fe metal centre (charge depletion in d_{z^2} and accumulation in d_{xz} and d_{yz}) when compared to the behaviour seen in both Fig. 5.5a and Fig. 5.5b. This might result from the Ag(111) having a stronger *trans*-effect than the NH_3 ligand, indicated by the longer *trans*-ligand to Fe bond length for Ag, as discussed previously. The CRMs including Ag(111) shown in Fig. 5.5 are calculated for the Fe centre above a hollow site, but similar calculations (not shown here) for an atop and a bridge site show the same effect, further indicating that it is the interaction with the delocalised metal electrons of the substrate, rather than a direct interaction with a substrate atom that drives the surface *trans*-effect. These calculations thus indicate that the same effect would be seen for both commensurate and incommensurate overlayers.

Interestingly, the intensity of the surface *trans*-effect seen on Ag(111) appears to be dependent upon the ability to accumulate charge between the Ag(111) surface and the FePc. This may explain why the inclusion of dispersion forces dramatically changes the predicted structural differences induced by the surface *trans*-effect. The vdW corrections predict a less negative electrostatic potential for the clean Ag(111) surface than the uncorrected calculations do (see Fig. 5.6). Specifically at the measured adsorption height of the FePc molecule ($\sim$2.8 Å, corresponding to 1.2 Ag substrate layer spacings) the potential, with respect to the vacuum level, is less negative by $\sim$0.4 eV (Fig. 5.6). Therefore, in the region between the surface and the adsorbed molecule there is a significant decrease in the energy required to remove an electron to the vacuum level, i.e. the local work function is significantly reduced. We posit that this lowering of the local work function, when using the vdW-DF functional, allows a greater charge accumulation in the σ-bonding area, intensifying the Ag(111) surface *trans*-effect. Such a sensitivity to changes in the local work function reinforces the idea that the surface *trans*-effect arises from interactions with the electrostatic potential of the substrate, rather than being mediated through direct interaction with any individual atom. The theoretical calculations thus predict that the "surface *trans*-effect" is mediated through redistribution of charge along the *trans* σ-bonds in a manner similar to that of the traditional *trans*-effect.

5.4 Conclusion

Utilising the X-ray standing waves technique, we have obtained the first quantitative structural measurement of the consequences of the so-called "surface *trans*-effect", observing the displacement of the metal centre of a metal-organic species by its ligation to a molecular ligand. This displacement has been modelled by DFT calculations that show excellent agreement with the experimental results, provided that corrections are included for dispersion forces. Furthermore, these dispersion-corrected calculations predict that the electronic effect on the FePc/water moiety of introducing the Ag(111) surface is

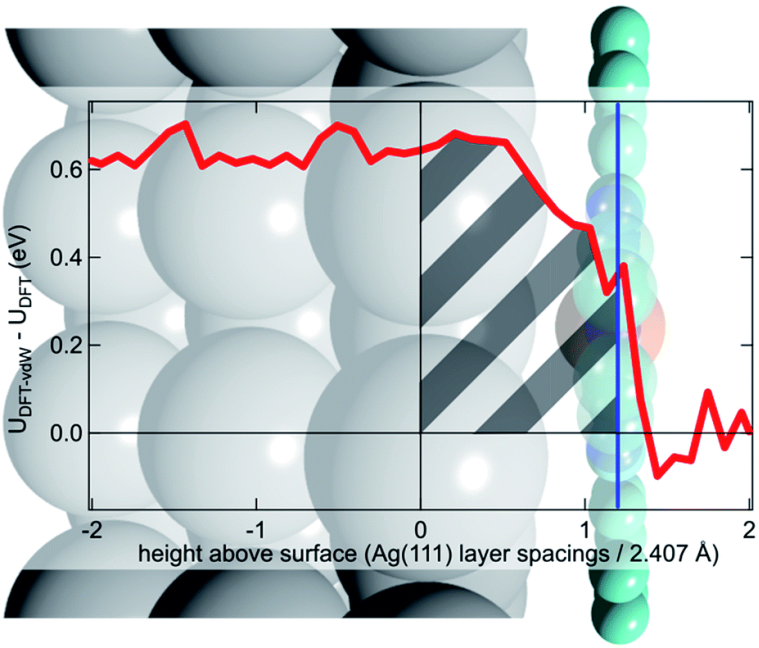

Figure 5.6: Difference between the optB88-vdW and PBE functionals in the calculated plane-averaged electrostatic potential from a clean Ag surface (red line), the termination of which is set at 0, overlaid atop a schematic of Ag(111)/FePc. The adsorption height of the FePc is also indicated (blue line), showing that at the position occupied by the FePc molecule the dispersion corrected DFT calculations predict a more positive potential. We posit that this allows a greater accumulation of charge between the surface and the adsorbed FePc (shaded grey), intensifying the *trans*-effect of the surface.

remarkably similar to that of introducing an ammonia molecule. However, the main difference between the traditional *trans*-effect and the surface *trans*-effect would seem to be that, rather than involving a direct interaction between the metal complex centre and an atom in the coordinating ligand/surface, it is the interaction between the metal complex centre and the delocalised electronic states of the metal substrate that drives the surface *trans*-effect.

This result has wide-ranging implications in the field of metal-organic complexes supported on metal substrates. The most obvious influence is on potential catalysts, especially considering adsorbed planar species like MPs and MPcs, as the active site is inherently *trans* to the substrate, and the coordination of a ligand *trans* to the substrate gives rise to the activated complex of such a catalyst. It can be inferred that the weakening of the metal centre-ligand interaction by the substrate will suppress the reactivity of the adsorbed complex, suggesting that one cannot simply adsorb a liquid or gas phase catalyst onto a metal substrate and expect comparable activity. Instead, as concluded in a previous published work from our group [23], it may be necessary to choose metal centres that are traditionally seen as being "too reactive" for catalytic reactions. It is also not unreasonable, as was proposed by Hieringer et al. [22], to expect that different substrates will have varying intensities of the surface *trans*-effect. This extra degree of freedom could be exploited to tune the selectivity of such a catalyst, for example, in electrochemical oxygen [139] and CO_2 [172] reduction, where the metal-organic complexes are positioned on a metallic electrode. In a similar fashion, the consequences for the design of electronic devices that assume the substrate to be an inert component will be deleterious; the influence of the substrate must be considered from the outset. On the other hand, this result is potentially promising in the field of adsorbed gas sensors. As the surface *trans*-effect not only affects the ligand to metal centre interaction, but also the surface to metal centre interaction, the response of the adsorbed metal complex to a gaseous species will induce an effect on the substrate, potentially amplifying the response of the gas sensor as was observed for NO ligation to FePc on graphene [151].

As it has now been clearly demonstrated that the surface *trans*-effect occurs in a manner similar to that in traditional coordination chemistry, it raises the question as to whether there is a comparable *cis*-effect. The *cis*-effect is considerably less studied in coordination chemistry than the *trans*-effect, but can have a similar influence on the reactivity of a metal complex, especially in octahedral systems. However, the experimental results presented here provide no evidence for such an effect, though some redistribution of charge in the plane of the FePc molecule was seen in the CRM's (cf. Fig. 5.5a). It is therefore probable that a surface *cis*-effect does indeed exist, hence, a study like that presented here, but investigating a system where a potential *cis*-effect would be expected to dominate, could be fruitful.

Finally, the prediction of the remarkable similarity of the electronic effect of the "surface *trans*-effect" to the traditional *trans*-effect, as shown in the charge redistribution maps,

strongly suggests that this phenomenon is truly a *trans*-effect, not only in appearance, but also in physical manifestation. Surprisingly, though it manifests as a *trans*-effect, this effect is not due to an interaction with a single substrate atom, but instead with the surface delocalised electrons, making this a true surface, rather than a local effect. Thus, we conclude that the name "surface *trans*-effect" is fully justified.

6 4-Fluorothiophenol on Ag(111) – a Prospective Molecular Spacer

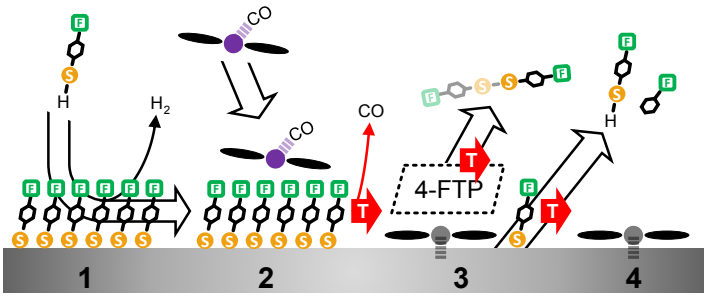

The precise control over the electronic properties and function of the metal centres in metal-organic complexes such as metallo-porphyrins (MPs) and metallo-phthalocyanines (MPcs) holds promise for their targeted application in, e.g., nanoscale chemical conversion devices and molecular sensors. However, when immobilizing these flat chelate complexes on solid supports, the influence of the latter on the metal centres can decisively alter their chemistry and functional properties, e.g. *via* the charge transfer and orbital hybridization observed on metal substrates. In the present work we explore a simple strategy to both spatially and electronically decouple prototypical MP and MPc compounds from a Ag(111) surface, by preventing direct physical contact with the underlying support *via* insertion of a self-assembled monolayer (SAM) of 4-fluorothiophenol (4-FTP). Such molecular spacers may thus provide extensive means to investigate, sustain and fine-tune the chemical reactivity of these complexes towards reactant species, aiming at their tailor-made application in, e.g., heterogeneous catalysis, as well as to allow for the design of hybrid functional systems of increasing sophistication such as stacked multilayer architectures. Herein, we show that at low temperature (∼150 K) the 4-FTP SAM on Ag(111) can indeed serve to decouple iron phthalocyanine (FePc) and ruthenium tetraphenylporphyrin (Ru(CO)TPP) monolayers from the Ag(111) surface. When the temperature is increased, however, the system's configuration breaks down, resulting in an inverted stacking followed by the complete removal of 4-FTP at elevated temperatures, the SAM thus playing the role of a thermally removable template. We elucidate the structural and chemical evolution of the organic double layer system by combination of X-ray photoelectron spectroscopy (XPS), temperature-programmed XPS (TP-XPS), temperature-programmed desorption (TPD), and low-energy electron diffraction (LEED) measurements.

6.1 Introduction

In the last two decades, numerous studies of metallo-porphyrins (MPs) and metallo-phthalocyanines (MPcs) have been undertaken on single-crystal supports and especially on metals [128, 129, 173], revealing their ability to form well-defined single-layer systems by self-assembly and opening up new prospects for the bottom-up functionalization and nanopatterning of surfaces. As in most cases these complexes adsorb with their tetrapyrrole macrocycle lying flat on the support (Fig. 6.1, A), the site *trans* to the surface remains accessible for the interaction of potential ligand molecules with the coordinatively unsaturated metal centre [22, 132, 169, 174, 175]. The reactivity of the latter towards incoming species, however, can be strongly influenced or even quenched by the supporting substrate [23], which can itself act as an axial ligand (cf. Refs. [21, 22, 132, 133, 154] and chapter 5), thus altering substantially the properties of the "immobilized" molecular complex. Indeed, charge transfer and orbital hybridization are often found to alter

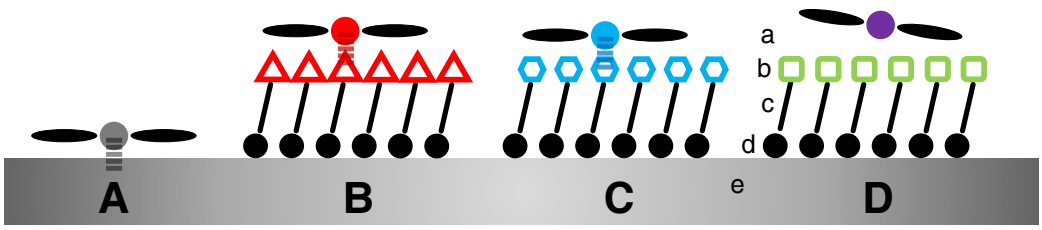

Figure 6.1: Schematic illustration of (A) a MP or MPc molecule adsorbed flat on a metal surface or (B-D) sitting on top of a self-assembled monolayer. Labels: a) MP or MPc; b) functional end group of SAM; c) backbone of SAM; d) head group of SAM binding to the substrate; e) metal substrate.

the formal oxidation state of the metal centre and the molecular electronic properties in general [176–180]. Thus, a major question arises whether it is possible, on metal supports, to maintain the properties and reactivity of the metal complexes preserved upon anchoring onto the solid surface. This can be decisive, for example, in heterogeneous catalysis, where one would ideally aim to combine the selectivity of the homogeneous catalyst (e.g., the metal complex) with the recyclability and ease of recovery of heterogeneous catalysts [125, 181, 182]. A possible, and in principle straightforward, strategy to achieve this goal could involve the functionalization of the metal surface with self-assembled monolayers (SAMs), where both the anchoring head group and the functional end group can be suitably chosen (Fig. 6.1, B-D). The modification of surfaces by means of SAMs [183] has been long known to afford a versatile approach to engineer tailor-made functional interfaces, particularly in organic electronics [184–192], for the design of artificial molecular devices [193, 194] and sensors [195, 196], the nanoscale patterning of surfaces [197] and in the field of biotechnology[191, 197]. Potential applications thus range from the

creation of highly sophisticated biocompatible interfaces, where SAMs provide enhanced specific binding and molecular recognition [195, 197], to the implementation in light emitting diodes [185, 186] and thin film transistors [187–190, 192]. Concerning the question raised above, SAMs may provide a robust and easy strategy to implement templates for decoupling, both structurally and electronically, MP or MPc monolayers from an underlying metal substrate [198]. As such, they have been utilized in previous studies to axially coordinate the metal centres of porphyrin molecules [199–204] by exploiting the central metal ion as the tether point [205], this approach potentially allowing to stack multilayer systems of MPs [199]. In a similar vein, the reactivity of the metal centre towards incoming ligands could, in principle, be influenced by the choice of the SAM, more precisely by the choice of the functional group interacting with the metal centre (Fig. 6.1, B-C), even providing a way to deliberately tune the specific binding properties of the latter.

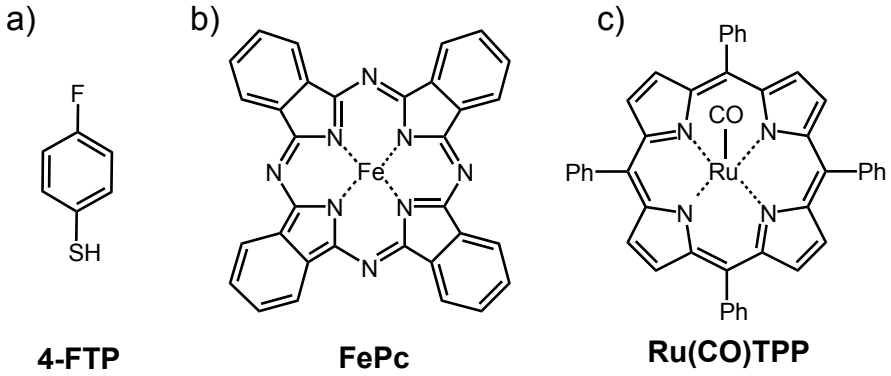

Figure 6.2: Chemical structure of the molecules used in this study: a) 4-fluorothiophenol (4-FTP), FC_6H_4SH; b) iron phthalocyanine (FePc), $C_{32}H_{16}N_8Fe$; c) ruthenium tetraphenylporphyrin (Ru(CO)TPP), $C_{44}H_{28}N_4Ru$-CO. In c) Ph denotes a phenyl substituent.

In the present study, with the future aim of probing the reactivity of "immobilized" MPs and MPcs upon decoupling from the metal surface and inspired by the previous work, we explore the structural and thermal evolution of two prototypical MP/SAM and MPc/SAM bilayers on Ag(111). This metal substrate was chosen because a variety of MPs and MPcs are known to readily self-assemble on its surface, forming ordered architectures [128, 129]. As to the SAM, we focus on the simplest aromatic thiol, benzenethiol or thiophenol, under addition of a fluorine end group, which – in contrast to some of the above mentioned investigations – is not expected to form a preferential (coordinative) bond with the metal centre of macrocyclic metal-organic complexes (cf. Fig. 6.1, D). Thus, the SAM should merely serve as "molecular spacer" between the latter and the underlying metal support. Iron phthalocyanine (FePc, Fig. 6.2b) and ruthenium tetraphenylporphyrin (Ru(CO)TPP with CO as protecting ligand, Fig. 6.2c) are deposited under highly controlled ultra-high vacuum (UHV) conditions onto the *in-*

situ prepared 4-fluorothiophenol (4-FTP, Fig. 6.2a) SAM on Ag(111). We find that at low temperature, the 4-FTP SAM indeed prevents direct contact of both tetrapyrrole molecules with the Ag(111) substrate, electronically decoupling the metal centre from the underlying metal substrate, whereas upon annealing, the spatial decoupling breaks down, with both FePc and RuTPP going underneath the SAM into direct contact with the Ag surface. Finally, at elevated temperatures (up to 700 K) the SAM molecules are removed by desorption, while the tetrapyrrole molecules remain adsorbed. The presented study highlights that the combination of X-ray photoelectron spectroscopy (XPS), temperature-programmed XPS (TP-XPS), temperature-programmed desorption (TPD), and low-energy electron diffraction (LEED) provides exhaustive chemical and structural information of such layered assemblies, thus spurring the investigation and the design of sophisticated functional layers and interfaces at the atomic scale by means of these methods.

6.2 Experimental Details

All experiments have been performed in the custom-made UHV chamber described in section 3.1, at a base pressure in the low 10^{-10} to mid 10^{-11} mbar regime. A clean Ag(111) surface was prepared by sputtering with Ne^+ ions (Neon 5.0, $p_{Neon} \approx 1 \times 10^{-5}$ mbar, $U = 1.1$ kV) at 300 K for 15 - 30 min and in grazing incidence geometry, followed by annealing at 725 K for 10 min (heating ramp: $2\,\mathrm{K\,s^{-1}}$; cooling down: $-1\,\mathrm{K\,s^{-1}}$). The cleanliness of the Ag(111) surface was assessed by means of XPS. The FePc (Sigma Aldrich, 90 % pure by dye content, triply purified [157]) was deposited by sublimation from a home-built Knudsen cell with quartz glass crucibles at ∼620 K. Similarly, Ru(CO)TPP (Sigma Aldrich, dye content ∼80 %) was evaporated at ∼610 K. The 4-FTP (Sigma Aldrich, 98 % purity, liquid) was purified by repeated freeze-thaw cycles and deposited by means of the needle doser described in section 3.1. The fluoro-terminated benzenethiolate SAM was prepared following saturation exposure of 4-FTP onto the Ag(111) sample kept at 300 K. LEED measurements were performed with the sample held at 90 K, and the superimposed reciprocal-space structures depicted in Figs. 6.3, 6.5 and 6.7 have been generated by means of the LEEDpat software [96]. TPD spectra were taken with a quadrupole mass spectrometer enclosed within a copper Feulner-cap, as described in section 3.1, and with the Ag(111) crystal positioned close to a millimetre from the cap aperture. Specifically, for the H_2 desorption measurement the inner surface of the Feulner-cap served to pump the enclosed volume *via* a freshly deposited titanium getter film and cryo trapping *via* liquid nitrogen flow cooling. Furthermore, during experiments an additional cold trap, covered by freshly deposited titanium films and cooled by liquid nitrogen flow, served to minimize the background pressure in the UHV chamber. In the TPD measurements, two different mass intervals were typically monitored, either sweeping the full mass-to-charge (m/z in units of amu/elementary charge) range between 5 and 135 (step 0.2) or – in

the low mass range – between 0.5 to 19 (step: 0.1). The (TP-)XPS measurements were performed using the non-monochromatized $Mg\text{-}K\alpha$ emission line (1253.6 eV) of the twin anode X-ray source. If not otherwise stated, the XPS measurements were carried out at 90 K. All XP spectra were calibrated against the binding energy of the Ag $3d_{5/2}$ core-level line (368.27 eV) [206]. The TP-XPS measurements were performed with a pass energy of 15 eV, in normal emission ($\theta_{emission} \approx 0°$, NE) geometry, with large area (LA) lens mode and a linear heating rate of 0.1 K s^{-1}. The Fe $2p_{3/2}$ TP-XPS contour plot in Fig. 6.8d was obtained after normalization and subtraction of a parabolic background from the individual XPS scans, whereas the corresponding S $2p$ spectrum in Fig. 6.8c was obtained by normalization to the high kinetic energy background only. Similarly, the S $2p$ and O $1s$ TP-XP spectra in Fig. 6.10a and 6.10c were obtained by normalization of the individual XPS scans only, while in the Ru $3d_{5/2}$ contour plot of Fig. 6.10b a straight line of fixed slope was subtracted from each XPS scan. Standard XP spectra were acquired in both normal and grazing emission ($\theta_{emission} \approx 70°$, GE) geometry, with 15 eV pass energy and medium area (MA) lens mode. To evaluate the peak positions in the standard XP spectra, fitting has been performed with the FitXPS software [207], utilizing simple parabolic (Fe $2p_{3/2}$, Ru $3d_{5/2}$, F $1s$) and linear backgrounds (S $2p$, O $1s$).

6.3 Results and Discussion

6.3.1 4-FTP SAM on Ag(111)

A saturated monolayer of 4-FTP was initially prepared by exposing the clean Ag(111) surface to the molecular vapours at 300 K. The XP spectrum labelled 1 in Fig. 6.3a shows the S $2p$ region of such a saturation coverage, recorded at a sample temperature of 90 K. The S $2p_{3/2}$ and $2p_{1/2}$ core-level lines in this spectrum are centred at binding energies (BE) of 161.7 eV and 162.9 eV, respectively, implying that the 4-FTP molecules form a thiolate bond with the underlying Ag(111) support [208–212]. No traces of chemisorbed atomic sulphur, expected to show up at 160.9 eV for the S $2p_{3/2}$ line [209], are detected in the measurements. This finding confirms that the C-S bond remains intact upon adsorption, which is further corroborated by the associated C $1s$ spectrum shown in Fig. 6.4. Here, fitting with three peaks of equal width on a linear background reveals three chemically distinct carbon species [213]: the dominant feature at 284.5 eV (C-C) is attributed to the carbon atoms in the phenyl ring of 4-FTP which are bound to two other carbon atoms; the two weaker features at 285.2 eV (S-C) and 286.5 eV (F-C) represent the carbon atoms bound to sulphur and fluorine species, respectively. The corresponding area ratio for the fitted carbon peaks of 1 (C-C) : 0.24 (S-C) : 0.26 (F-C) is in excellent agreement with the expected stoichiometric ratio of 4 (C-C) : 1 (S-C) : 1 (F-C) for 4-FTP. Therefore, this result confirms that the C-S bond is preserved upon adsorption and SAM formation and demonstrates the integrity of the 4-FTP molecule within the SAM. In addition, the

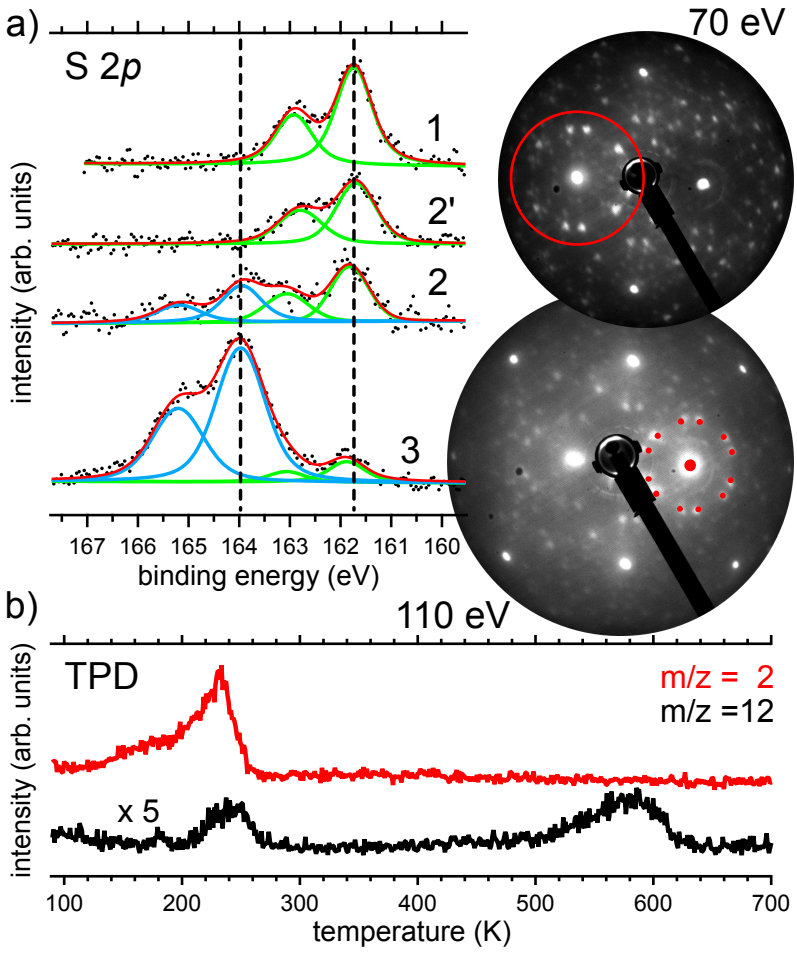

Figure 6.3: a) S 2*p* XP spectra of 4-FTP deposited on the Ag(111) surface at (1) 300 K, (2) 190 K (T_{meas} = 190 K) and (3) 90 K. All spectra were recorded at normal emission. Spectrum 2′ corresponds to preparation 2 after increase of the sample temperature to 255 K (T_{meas} = 255 K). The LEED patterns of a saturated monolayer of 4-FTP deposited at 300 K, as in preparation 1, are shown on the side (electron energies: E_p = 70 and 110 eV). The red circle and the spots highlighted in red signal the dominant $(\sqrt{7} \times \sqrt{7})$R19.1° superstructure. b) TPD spectra recorded with a heating rate of 0.5 K s^{-1} after 4-FTP deposition at 90 K.

F 1*s* binding energy of 687.0 eV (Fig. 6.8b, spectrum 1) is only marginally different from that of a condensed 4-FTP multilayer (686.95 eV) [213], suggesting that the fluorine end group in the saturated 4-FTP monolayer does not directly interact with the metal surface, compatible with a tilted up orientation of the molecules above the surface.

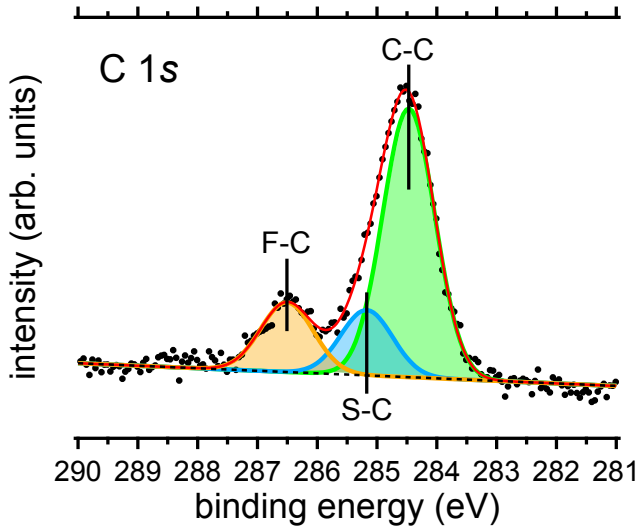

Figure 6.4: C 1*s* (NE) XP spectrum of the saturated monolayer of 4-FTP, deposited onto the Ag(111) surface at 300 K and corresponding to the S 2*p* XP spectrum 1 in Fig. 6.3a. This C 1*s* spectrum has been recorded subsequent to spectrum 1 in Fig. 6.3a, at the same nominal conditions and with the same measurement settings.

Conversely, spectrum 3 in Fig. 6.3a shows that for a thin multilayer of 4-FTP deposited at 90 K, the binding energies of the dominant S 2*p* components are located at 164.0 eV ($2p_{3/2}$) and 165.2 eV ($2p_{1/2}$), respectively. This clearly indicates the presence of unreacted thiol molecules [210, 211]. The weak components at 161.9 eV and 163.1 eV also reveal that only a small fraction of 4-FTP molecules at the interface undergoes S-H cleavage and thiolate formation at 90 K. Upon deposition at 190 K, spectrum 2 comprises thiol and thiolate species in roughly 1 : 1 proportion, whereas increasing the temperature to 255 K (spectrum 2′) yields a slight increase in the thiolate signal and completely removes the thiol component.

The thermal evolution of the layer composition from thiol to thiolate is further elucidated by the TPD measurements in Fig. 6.3b, where the broad feature peaked at 235 K for $m/z = 2$ signals H_2 desorption from the surface following S-H bond cleavage and (at least partial) recombination of atomic H into H_2 [214, 215]. The thiolate formation thus appears to be completed just above 250 K. Concomitantly, the slightly shifted maximum in the carbon signal intensity ($m/z = 12$) shows that, independently of the S-H cleavage, desorption of excess 4-FTP takes place between 210 and 270 K, whereas the broad peak

between 520 and 620 K corresponds to the desorption of the thiolate species of the SAM, as will be discussed in more detail in section 6.3.5.

In summary, the XPS and TPD measurements give evidence of the formation of a well-defined 4-FTP SAM at room temperature (RT), anchored to the Ag(111) surface *via* a thiolate bond. The thermal evolution of the S-H bond reveals that above 250 K no intact thiol species are present on the surface. The molecules in the SAM are expected to adsorb in a tilted up geometry, in accordance with previous reports on 4-FTP SAMs on coinage metal surfaces [216–218], where adsorption angles between 30° (Au(111) [217]) and 60° (Cu(100) [218]) relative to the surface plane were suggested. Importantly, the obtained SAM exhibits a predominant LEED pattern featuring a long-range ordered $(\sqrt{7} \times \sqrt{7})$R19.1° superstructure (Fig. 6.3). This indicates ordered packing of the molecules with a prevailing superstructure described by the matrix notation $\begin{pmatrix} 2 & -1 \\ 1 & 3 \end{pmatrix}$ and a nominal coverage of $1/7 = 0.143$, which was previously observed also for 4-FTP on Cu(111) [216]. In contrast, for thiophenol (TP) on Ag(111) a $(\sqrt{7} \times \sqrt{31}, 88°)$R40.9° phase with 4 standing up TP molecules and 17 Ag atoms per unit mesh has been reported (coverage: 0.235) [219]. On the same Ag surface, $(\sqrt{7} \times \sqrt{7})$R19.1° structures similar to our study were observed for atomic sulphur [220], methanethiolate [221], and SAMs of longer chain alkanethiols [222], whereby a complex, reconstructed surface model with a nearly hexagonal surface Ag layer with lower Ag density (i.e., 3/7 of that of the underlying substrate layers) and three sulphur atoms per unit mesh was proposed. Note that our LEED analysis cannot provide conclusive evidence regarding the involvement of the Ag surface layer in the long-range superstructure, which is beyond the scope of the present work.

6.3.2 Compression of FePc by Co-Deposited 4-FTP

Before examining the adsorption of FePc on top of the 4-FTP SAM introduced above, we investigated the pristine FePc monolayer on Ag(111) and the effect caused by co-adsorbed 4-FTP molecules. Fig. 6.5a shows the LEED pattern of FePc/Ag(111) for a coverage slightly lower than that of the densest monolayer of FePc on Ag(111). It corresponds to the overlayer structure identified as a commensurate C2-phase in the detailed work of Bobaru et al. [158] and is described by the epitaxy matrix $\begin{pmatrix} 5 & 0 \\ 3 & 6 \end{pmatrix}$, corresponding to a 0.033 coverage with respect to the Ag surface density. After prolonged exposure to 4-FTP at 300 K, this superstructure changes (Fig. 6.5b), yielding a clearly distinct LEED pattern. The latter closely resembles that of the incommensurate FePc/Ag(111) I-phase of the saturated single layer (cf. Bobaru et al. [158]) with matrix $\begin{pmatrix} 4.80 & -0.40 \\ 2.58 & 5.68 \end{pmatrix}$. This phase is known to exhibit a moderately denser packing of the FePc molecules, which is maintained up to monolayer completion [158]. Similar dense phases, with slightly modified matrix

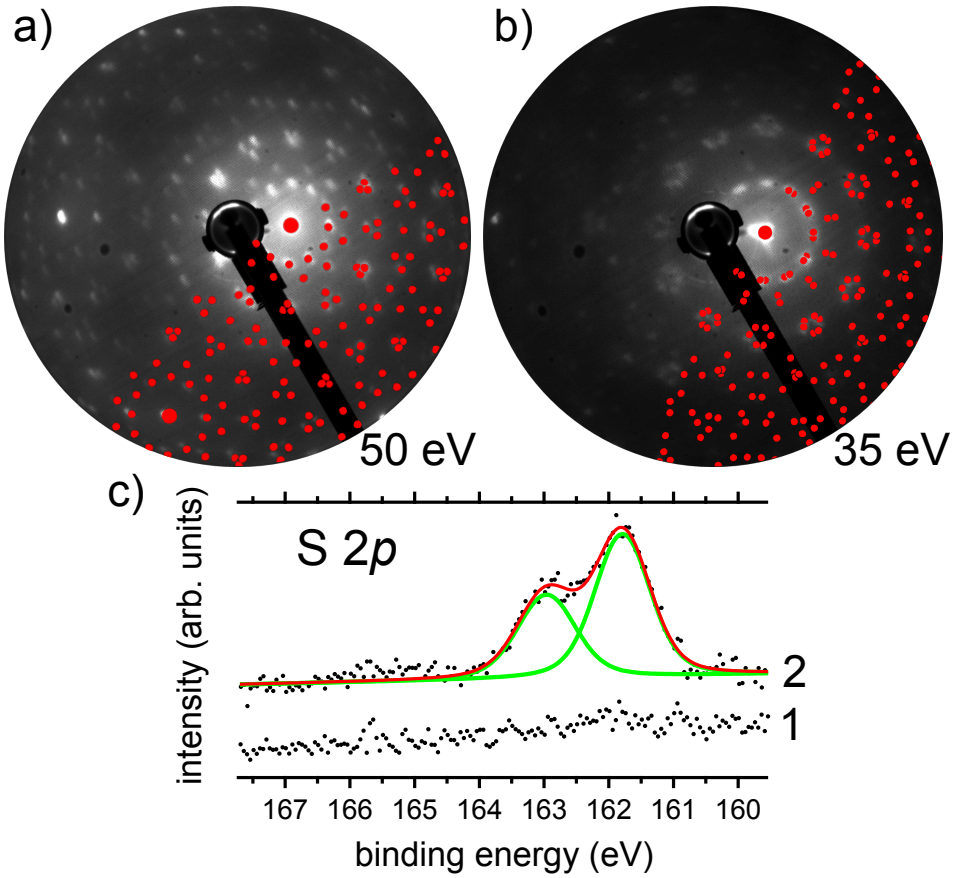

Figure 6.5: LEED pattern of FePc/Ag(111) recorded at 85 K: a) prior to and b) after exposure to 4-FTP at 300 K. The overlayer in a) corresponds to the C2-phase described by Bobaru et al. [158], the overlayer in b) to the I-phase of the same work. Red dots mark the reciprocal space spots corresponding to the respective matrix notations reported in the text. c) S 2*p* (GE) XP spectra for the FePc overlayers in a) and b), thus (1) before and (2) after the deposition of 4-FTP at 300 K (T_{meas} = 300 K).

notation, are also found for other Pc species on Ag(111), e.g. CuPc [223] and TiOPc [179]. Fig. 6.5c shows corresponding S 2*p* XP spectra before (spectrum 1) and after (spectrum 2) the deposition of 4-FTP at 300 K. After 4-FTP deposition, the presence of S $2p_{3/2}$ and $2p_{1/2}$ lines at 161.8 eV and 163.0 eV, respectively, indicate that 4-FTP is co-adsorbed in the form of a thiolate as seen in Fig. 6.3a (spectrum 1). However, the corresponding Fe $2p_{3/2}$ spectra of the FePc layer (displayed in Fig. 6.6) show no considerable modification of the Fe $2p_{3/2}$ core-level line between spectrum 1 and 2 (prior to and after 4-FTP exposure), with both spectra resembling the shape of the reference monolayer in spectrum 3. This suggests that the sulphur moiety of the 4-FTP molecules does not coordinate to the iron

centres of the FePc molecules. We thus assume that thiolate formation occurs on patches of free Ag, and based on the change of the LEED pattern in Fig. 6.5 we propose that the co-adsorbed 4-FTP compresses the FePc islands into a denser phase. This is, in turn, indicative of a phase separation between chemisorbed 4-FTP and FePc molecules, rather than mixing of both species.

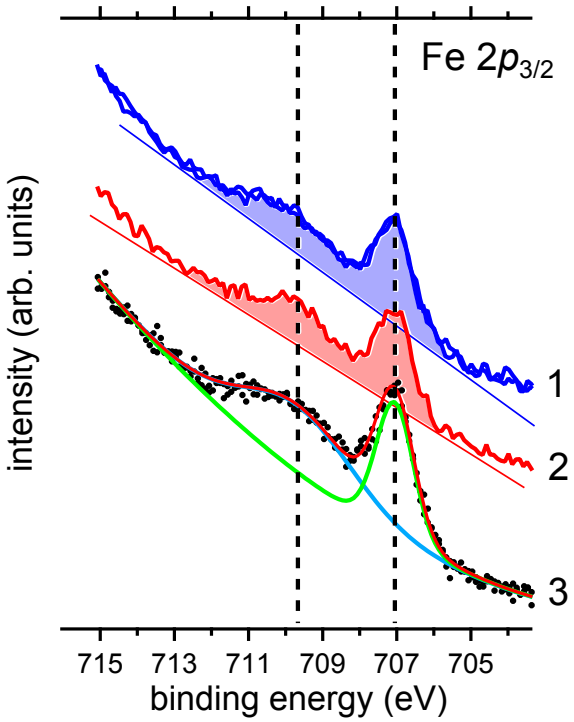

Figure 6.6: Fe $2p_{3/2}$ (GE) XP spectra of (1) an FePc coverage on Ag(111) slightly lower than the densest monolayer (T_{meas} = 300 K), (2) the system in spectrum 1 after 4-FTP exposure at 300 K (T_{meas} = 300 K) and (3) the reference monolayer of FePc on Ag(111) shown in spectrum 5 of Fig. 6.7a (T_{meas} = 90 K). Note that the Fe $2p_{3/2}$ spectrum 1 corresponds to the S 2*p* (GE) XP spectrum 1 in Fig. 6.5c and, similarly, spectrum 2 corresponds to the system investigated in spectrum 2 in Fig. 6.5c. The continuous straight lines and shaded areas in spectrum 1 and 2 are arbitrarily drawn to allow for qualitative comparison. The peak positions of the reference layer in spectrum 3 are marked by vertical dashed lines.

6.3.3 Deposition of FePc onto 4-FTP SAM / Ag(111)

Fig. 6.7a displays a collection of Fe $2p_{3/2}$ XP spectra for different preparations. The bottom spectrum, denoted 5, presents the Fe $2p_{3/2}$ signature of a saturated monolayer of FePc on Ag(111). The sharp feature at a binding energy of 707.0 eV, emerging from

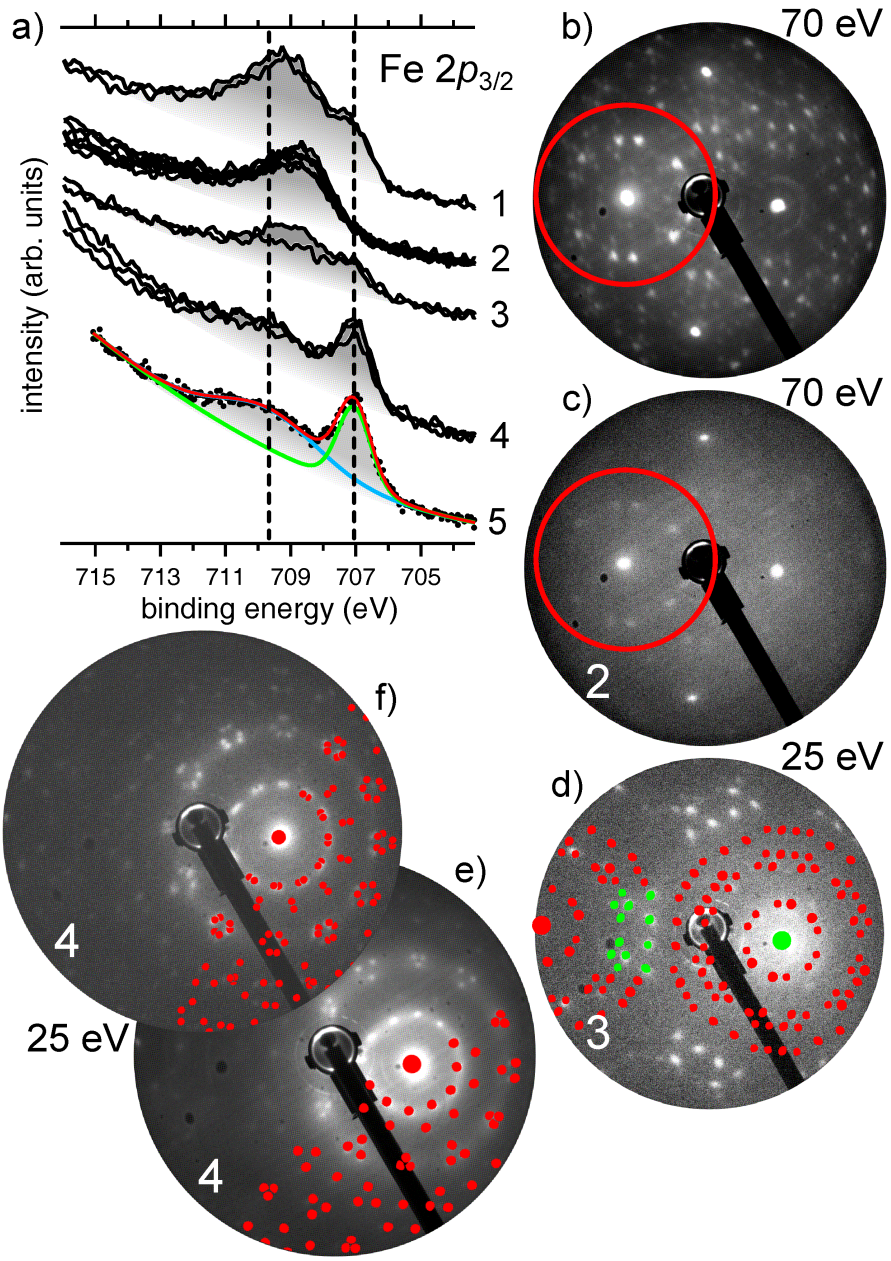

Figure 6.7: a) Fe $2p_{3/2}$ (GE) XP spectra of (1) FePc deposited onto a FePc monolayer, (2) FePc deposited onto the 4-FTP SAM at 90 K and annealed to 130 K, (3) 300 K and (4) 500 K, and (5) an FePc/Ag(111) monolayer. All XP spectra were recorded at T_{meas} = 90 K. Peak positions for the FePc monolayer are marked by vertical dashed lines. b) LEED pattern of the 4-FTP SAM on Ag(111). c-f) LEED patterns of FePc deposited onto the 4-FTP SAM at 90 K after annealing to c) 130 K, d) 300 K, e-f) 500 K. All LEED patterns were recorded at T_{meas} = 90 K and with the indicated electron energies.

the complex multiplet structure of the transition metal ion, is usually assumed to arise from the interaction between the Fe metal centre and the underlying metal support and associated to Fe(0) (cf. Refs. [174, 224–226]). However, when depositing a comparable amount of FePc on top of the 4-FTP SAM at 90 K (followed by an annealing step to 130 K), the surface-induced Fe $2p_{3/2}$ feature at 707.0 eV completely disappears, leaving only the single broad multiplet structure centred between 708 and 709 eV (spectrum 2 in Fig. 6.7a). This clearly indicates the absence of a direct contact between the FePc molecules and the metal surface. Notably, a similarly broad Fe $2p_{3/2}$ multiplet structure at 709 eV has also been reported for FePc multilayers by Bai et al. [224] and related to a Fe central ion in the 2+ oxidation state. Furthermore, when comparing the respective LEED patterns of the 4-FTP SAM on Ag(111) before (Fig. 6.7b) and after (Fig. 6.7c) deposition of FePc, it is observed that the 4-FTP signal gets strongly attenuated, but still the predominant $(\sqrt{7} \times \sqrt{7})$R19.1° superstructure remains visible, as highlighted by the red circles in Fig. 6.7b and 6.7c. Taken together, these findings indicate that the structure of the 4-FTP SAM is preserved upon FePc deposition at low temperature and that the FePc molecules must be sitting on top of the SAM, spatially and electronically decoupled from the Ag(111) support. The absence of additional diffraction spots in the LEED pattern of Fig. 6.7c suggests that the FePc on top of the 4-FTP layer exhibits no long-range order. Further evidence for the spatial and electronic decoupling of the FePc molecules of spectrum 2 from the Ag(111) surface is provided by direct comparison to spectrum 1 in Fig. 6.7a, where additional FePc was deposited onto a saturated FePc monolayer. Here, the FePc molecules in the second layer contribute to an enhancement of the multiplet features at higher binding energy and to the pronounced attenuation of the low binding energy component of FePc in direct contact with Ag(111).

Notably, when the FePc/4-FTP/Ag(111) junction is annealed to 300 K, spectrum 3 in Fig. 6.7a is obtained, which shows an overall decrease of the Fe $2p_{3/2}$ signal, together with the reappearance of the interface related component around 707.0 eV. Moreover, a new dominant LEED pattern becomes visible (Fig. 6.7d), which closely resembles the denser $(\sqrt{7} \times \sqrt{31}, 88°)$R40.9° phase reported by Gui et al. [219] for thiophenol (TP) on Ag(111) and exhibits a characteristic motif in reciprocal space (green and red dots in Fig. 6.7d). This structure can be described by the epitaxy matrix $\begin{pmatrix} -1 & -3 \\ 6 & 1 \end{pmatrix}$ and thus represents a commensurate overlayer.

The described changes indicate that the spatial decoupling of FePc from the metal substrate through the 4-FTP SAM breaks down at room temperature, leaving access (at least partly) for the FePc molecules to the underlying Ag surface and inducing a compression of the chemisorbed 4-FTP SAM into a denser phase. Such behaviour corroborates the tendency to phase separation proposed in the previous section. Note also that the majority of 4-FTP still remains adsorbed upon this change in morphology, as discussed in more detail in section 6.3.5. Finally, following annealing to 500 K, the Fe $2p_{3/2}$ signal (spectrum 4 in Fig. 6.7a) resembles the signature of monolayer FePc on Ag(111), with

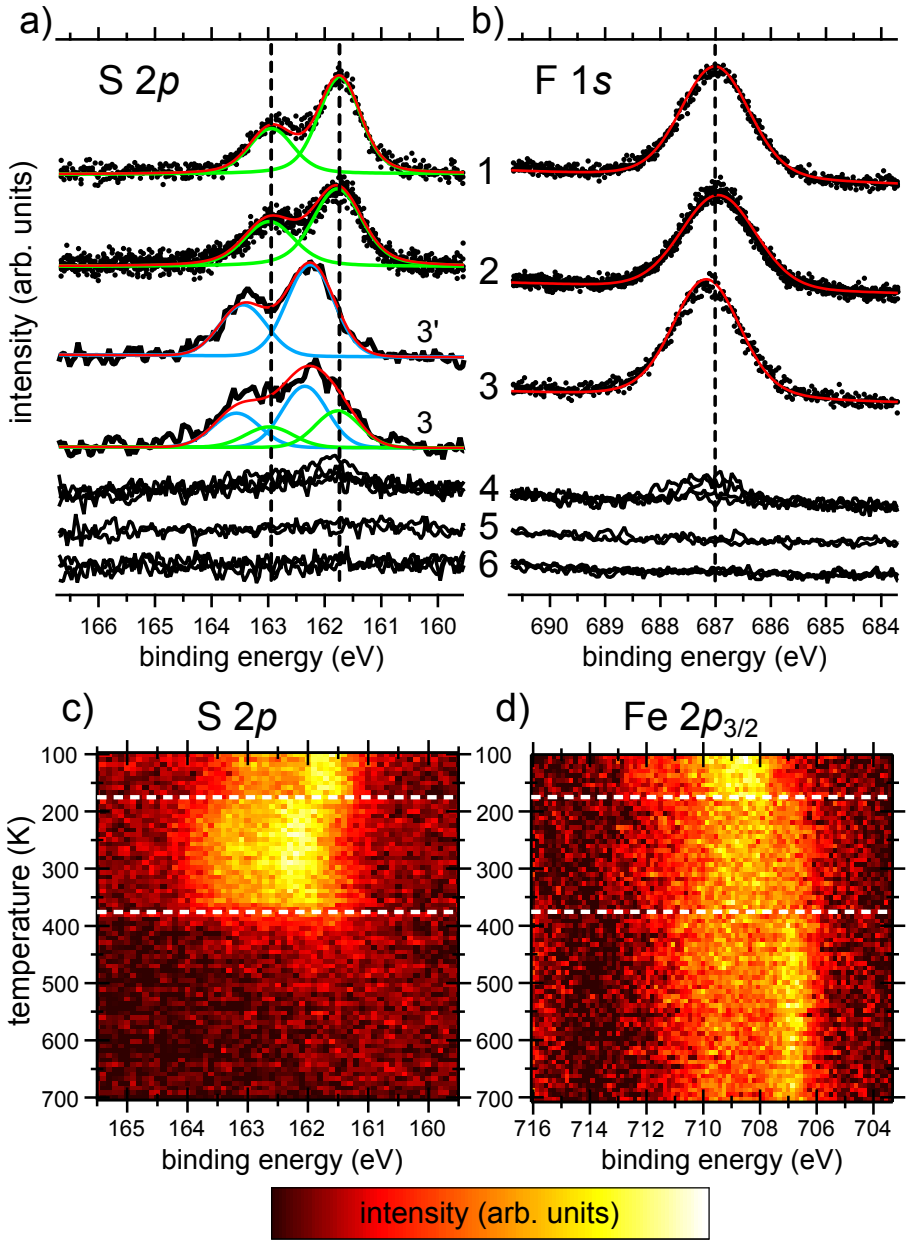

Figure 6.8: a) S 2*p* and b) F 1*s* XP spectra of (1) 4-FTP SAM on Ag(111) at 90 K, (2) FePc deposited onto the 4-FTP SAM at 90 K and annealed to 130 K, and after further annealing to (3) 300 K, (4) 500 K and (5) 700 K, and (6) FePc monolayer on Ag(111) as reference. All XP spectra were recorded in NE geometry. Dashed vertical lines indicate the fitted peak positions. Panels c) and d) display the corresponding TP-XP spectra comprised of alternatingly scanned S 2*p* and Fe $2p_{3/2}$ regions (temperature range: 100 - 700 K, heating rate: 0.1 K s^{-1}).

spots of both the C2- and I-phases [158] present in the LEED patterns (cf. Fig. 6.7e and 6.7f). This is in strong contrast with the system annealed to only 300 K, where a dominant (compressed) 4-FTP superstructure is identifiable, and may be explained by the removal of 4-FTP at such elevated temperatures.

The presented data suggest that the 4-FTP SAM acts initially as a spatial decoupling layer but is then progressively displaced from the interface at increasing temperature. Evidence for this conclusion is provided by the spectroscopic fingerprints in Fig. 6.8. The S $2p$ (Fig. 6.8a) and F $1s$ (Fig. 6.8b) spectra of the SAM on Ag(111) (labelled 1) do not show any clear shifts in binding energy after deposition of FePc at 90 K and annealing at 130 K (spectra labelled 2). Thus, the sulphur head group of the SAM remains bound to the surface as a thiolate species and the fluorine end group interacts only very weakly with the physisorbed FePc molecules. However, after annealing the system to 300 K, the S $2p_{3/2}$ and $2p_{1/2}$ lines shift to ∼162.3 eV and ∼163.5 eV (spectrum 3′ in Fig. 6.8a), respectively, corresponding to a distinct shift of 0.6 eV towards higher binding energy, and thus indicating a chemical change of the 4-FTP overlayer. Nevertheless, remainders of the Ag-bound thiolate species may still be present, as observed in the fitting analysis of spectrum 3 in Fig. 6.8a (see also the more complete fitting analysis in Fig. A.1 in appendix A.1). Along with the change of the S $2p$ signals after annealing to 300 K, also the broad F $1s$ peak shows a similar but smaller shift from 687.0 eV to 687.2 eV. We rationalize these shifts in terms of the FePc molecules "slipping" underneath the 4-FTP layer and coming into direct contact with the Ag surface. Specifically, if the coverage of FePc is high enough to saturate the silver surface, all 4-FTP molecules will be detached with their sulphur head group from the Ag surface and displaced above the FePc overlayer, yielding a true chemical shift for the S $2p$ core levels (cf. spectrum 3′ in Fig. 6.8a). At lower FePc coverage, however, a fraction of 4-FTP may remain bound to the Ag(111) surface as in the original thiolate-bonded SAM (cf. spectrum 3 in Fig. 6.8a and appendix A.1) and may be compressed into the denser phase described by the LEED pattern of Fig. 6.7d. The F $1s$ core level, in contrast to the S $2p$ line, is less perturbed and the small binding energy change is presumably related to the reduced polarization screening of the core hole at increasing separation from the metal surface [227, 228]. Further evidence for the inverted layer stacking of 4-FTP and FePc upon annealing to 300 K is provided by the change in the C $1s$ and S $2p$ attenuation for 4-FTP (appendix A.2, Figs. A.2 and A.3), with a distinct increase of the 4-FTP related signals upon annealing.

Finally, after heating the system to 500 K (spectrum 4 in Fig. 6.8a and 6.8b), only minor amounts of sulphur and fluorine are detectable, implying the almost complete removal of 4-FTP from the surface. Moreover, the S $2p_{3/2}$ binding energy of ∼161.8 eV of the persisting sulphur species indicates that, after this annealing step, the 4-FTP species remaining on the surface are only those directly bound to the Ag metal as thiolate (cf. TPD data in Fig. 6.11a and corresponding discussions in section 6.3.5). Again, this may occur if the deposited amount of FePc is less than needed for a full FePc saturated monolayer

on Ag(111) to fully replace the 4-FTP. Further annealing to 700 K leads, however, to desorption of all residual 4-FTP molecules (spectrum 5).

To better characterize the thermal evolution of the FePc/4-FTP bilayer, TP-XPS measurements were performed for both the S $2p$ and Fe $2p_{3/2}$ spectral regions, as shown in Fig. 6.8c and 6.8d, starting from FePc deposited on top of the 4-FTP SAM at 90 K. Below a temperature of ∼175 K (marked by a white dashed line in Fig. 6.8c and 6.8d), the Fe $2p_{3/2}$ region again shows the single broad multiplet feature at about 708 - 709 eV and the S $2p_{3/2}$ core level is centred at ∼161.7 eV (as in spectrum 2 in Fig. 6.8a). Above 175 K, the S $2p$ levels undergo a sudden jump to higher binding energy, as previously observed in Fig. 6.8a (from spectrum 2 to 3 and 3′) and in Fig. A.3 of the appendix, while the Fe $2p_{3/2}$ signal loses intensity and a component towards lower binding energy appears. The situation changes further above ∼375 K, whereby most of the 4-FTP is removed, and the FePc-metal interface related Fe $2p_{3/2}$ component at ∼707 eV is fully restored. The FePc molecules then remain adsorbed on the Ag(111) surface up to 700 K in the TP-XPS measurements.

Summing up, our data show that up to ∼175 K the prepared 4-FTP SAM can indeed serve as a molecular spacer layer for FePc, while the SAM becomes "permeable" to FePc at higher temperatures. This points to the interaction of the FePc molecules with the Ag(111) support being comparatively stronger than the thiolate bond between silver and 4-FTP.

6.3.4 Deposition of Ru(CO)TPP onto 4-FTP SAM / Ag(111)

To assess the generality of the scenario presented above, we investigated the adsorption of Ru(CO)TPP molecules on the 4-FTP SAM. After Ru(CO)TPP deposition onto the 4-FTP SAM at 90 K, followed by mild annealing at 200 K, a single Ru $3d_{5/2}$ component appears, located at a binding energy of 281.3 eV (spectra labelled 2 in Fig. 6.9a), which is accompanied by an O $1s$ line centred at 533.1 eV (spectra labelled 2 in Fig. 6.9b). Conversely, the porphyrin monolayer in contact with the Ag(111) support shows a sharp Ru $3d_{5/2}$ feature at 279.5 eV and no trace of oxygen (spectra labelled 3 in Fig. 6.9a and 6.9b). These two findings signal the loss of CO before or upon adsorption onto pristine Ag(111), to yield adsorbed RuTPP; in particular, the respective Ru $3d_{5/2}$ binding energy agrees well with the value for intact and cyclodehydrogenated RuTPP molecules (279.5 - 279.6 eV) adsorbed on Ag(111) in Refs. [229, 230], suggesting Ru in the Ru(0) oxidation state and therefore the occurrence of charge transfer from the silver substrate into the metal centre. On the other hand, the deposition of excess molecules beyond the monolayer coverage on top of RuTPP/Ag(111) leads to a second Ru $3d_{5/2}$ component close to 281.0 eV in the XP spectrum (Fig. 6.9a, spectrum labelled 1), distinctive of Ru(II) species [231], and again without presence of oxygen. By comparison, for Ru(CO)TPP deposited onto the 4-FTP SAM, the somewhat higher binding energy of 281.3 eV can most likely be attributed to the presence of CO (the protecting ligand) coordinated to the ruthenium centre. This

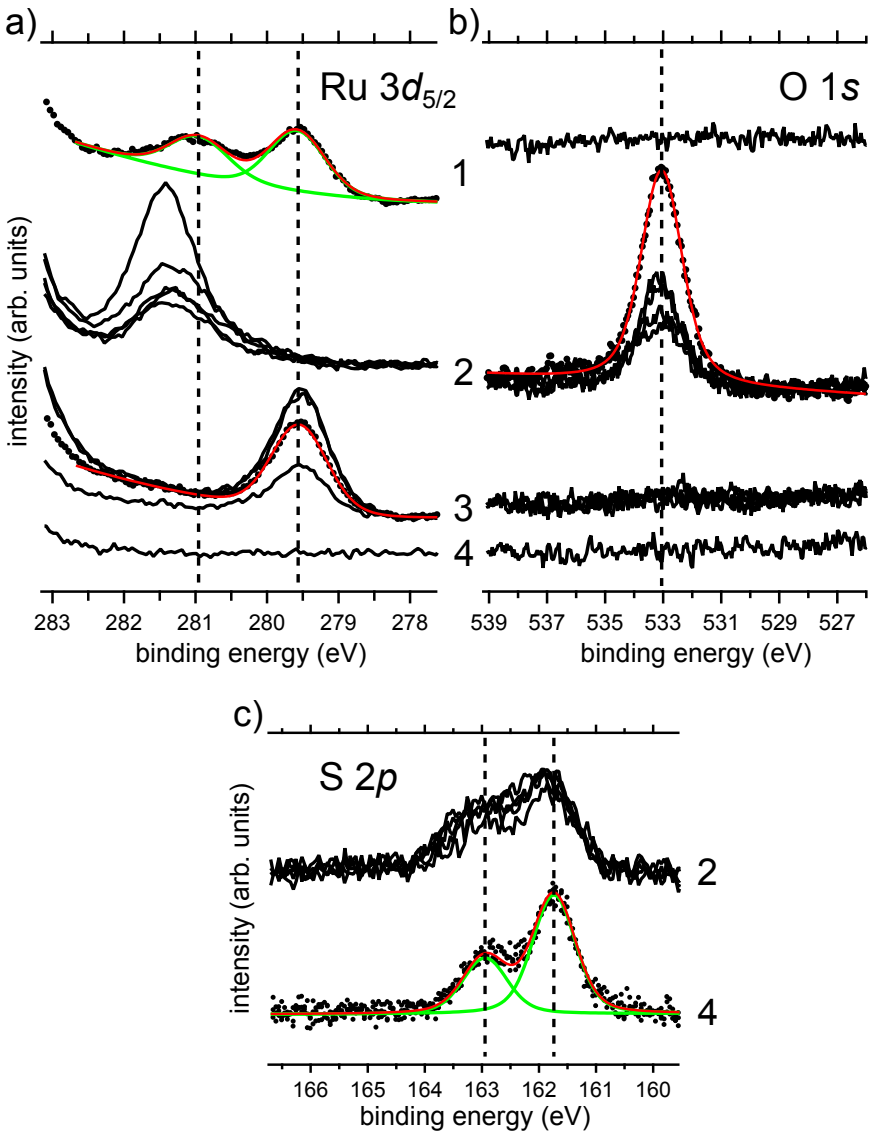

Figure 6.9: a) Ru $3d_{5/2}$ and b) O 1*s* XP spectra, recorded at GE, and corresponding c) S 2*p* spectra, recorded at NE, of (1) more than a saturated monolayer of RuTPP on Ag(111), (2) different coverages of Ru(CO)TPP on the 4-FTP SAM on Ag(111), (3) a saturated layer and various sub-monolayer coverages of RuTPP on Ag(111) and (4) the pristine 4-FTP SAM on Ag(111) as reference. Ru(CO)TPP has been deposited onto the 4-FTP SAM with the sample kept at 90 K, followed by mild annealing to 200 K. The spectra of the RuTPP layers in 1 and 3 were recorded at 300 K (except for one spectrum within 3, where the RuTPP sub-monolayer has been recorded at 90 K). The vertical dashed lines mark fitted peak positions.

conclusion is corroborated by a reported O 1*s* binding energy of 533 eV for CO binding to the iron centres in FePc/Au(111) [174]. Importantly, the S $2p_{3/2}$ core level in Fig. 6.9c is only marginally shifted to higher binding energy upon deposition of Ru(CO)TPP (from 161.7 eV, spectrum 4, to ∼161.8 eV, spectrum 2). As for the case of FePc, this indicates that up to 200 K the sulphur head groups of the molecules in the 4-FTP SAM remain bound to the underlying Ag substrate, preventing direct contact between Ru(CO)TPP and Ag(111) and suppressing the charge transfer from the metal substrate to the central Ru ions.

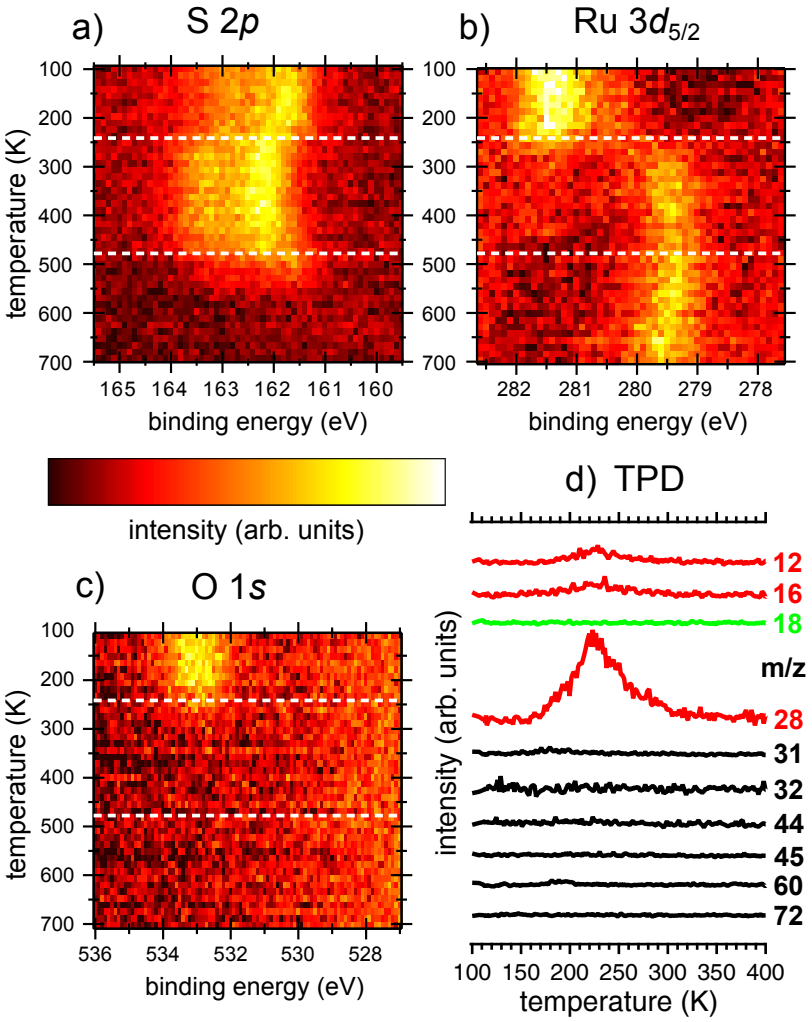

Figure 6.10: a)-c) S 2*p*, Ru $3d_{5/2}$ and O 1*s* TP-XP spectra of Ru(CO)TPP, after deposition onto the 4-FTP SAM at 90 K followed by slight annealing to 200 K. A heating rate of 0.1 K s^{-1} was used. d) Corresponding TPD spectra at a heating rate of 0.5 K s^{-1}.

The TP-XPS contour plots in Fig. 6.10a-c characterize the thermal evolution of the Ru(CO)TPP/4-FTP/Ag(111) system and verify the close similarity to the FePc case. In particular, a sudden shift of the dominant S $2p_{3/2}$ component at ∼161.8 eV to a higher binding energy centred around 162.2 eV occurs at a temperature of 240 K (marked by a white dashed line in Fig. 6.10a). At about the same temperature the centroid of the main Ru $3d_{5/2}$ line changes dramatically from ∼281.3 eV to ∼279.5 eV and the O 1*s* intensity appears to be completely quenched. As a consequence, the TP-XPS measurements reveal that the Ru(CO)TPP molecules come into direct contact with the surface at a temperature of 240 K. This is somewhat retarded in comparison with the 175 K for FePc, pointing to a weaker interaction of the porphyrin macrocycle with the silver substrate, which is presumably due to the presence of the tilted phenyl rings [153, 232]. Moreover, the similar onset for the changes of all core levels in Fig. 6.10 suggests that the bond of the Ru centres with the CO ligand is cleaved as soon as the porphyrin molecules are intercalated into the SAM and the charge transfer from the substrate into the Ru centres is established.

The attribution of the O 1*s* intensity (spectra labelled 2 in Fig. 6.9b) to the CO ligands (*vide supra*) is directly confirmed by TPD, as shown in Fig. 6.10d. Here, the dominant signal at $m/z = 28$ (CO), along with the corresponding CO fragments of $m/z = 16$ (O) and $m/z = 12$ (C), indicates molecular desorption of CO peaking at ∼230 K.

While the Ru(CO)TPP molecules come into contact with Ag(111), 4-FTP molecules have to be displaced from the organic/metal interface. This explains the observed shift of the S 2*p* line towards higher binding energy due to the modified chemical environment and polarization screening. The simultaneous desorption of CO may either be a direct cause of the newly evolving Ru-Ag(111) interaction or simply arise from replacement of the CO ligand with coordinating thiolate species. The 4-FTP molecules then start to desorb above 450 K (compared to the onset at 375 K for FePc), whereas the RuTPP remains on the surface up to much higher temperatures.

In conclusion, for adsorbed Ru(CO)TPP, the 4-FTP SAM can serve for spatial decoupling up to 240 K.

6.3.5 Desorption of the 4-FTP SAM

Finally, we focus on the thermal desorption of the SAM for the different systems considered in this study. The relevant TPD spectra are shown in Fig. 6.11a. As it turns out, depending on the system under investigation, 4-FTP does not simply desorb from the SAM as intact thiol, i.e. *via* recombination of the thiolate species with hydrogen atoms. In fact, the TPD measurements suggest a more complicated behaviour, with at least three different chemical species identified as possible desorption products. In Fig. 6.11, mass fragment $m/z = 108$ was monitored as the dominant fragment associated with the desorption of intact 4-FTP from the surface, whereas mass fragment $m/z = 83$ is proposedly attributed to thiolate radical detection. The latter would arise either from the direct desorption of the thiolate radical or as the fragment of a desorbing disulphide [215, 233], formed from

two thiolate species linking *via* their sulphur atoms rather than recombining into thiol. A third dominant desorbing species is detected at a mass-to-charge ratio $m/z = 96$ and assigned to fluorobenzene, signaling partial dissociation of 4-FTP *via* scission of the anchoring C-S bond. As the parent ion mass of the disulphide species ($m/z = 254$) was not accessible in the presented study, the assignment of the desorption products relies on the comparison with reference spectra for p-fluorobenzenethiol (SDBS No. 13725), bis(3-fluorophenyl) disulphide (SDBS No. 52131) and fluorobenzene (SDBS No. 2445) provided by the AIST database [41]. According to these reference data, mass fragment $m/z = 108$ should almost solely arise from the intact thiol species, whereas mass fragment $m/z = 83$ appears for both thiol and disulphide, but becomes more dominant (with respect to the parent ion) for the disulphide species, the latter thus serving as a measure for the desorption of either a thiolate radical or disulphide. Therefore, masses 83 and 108 should be

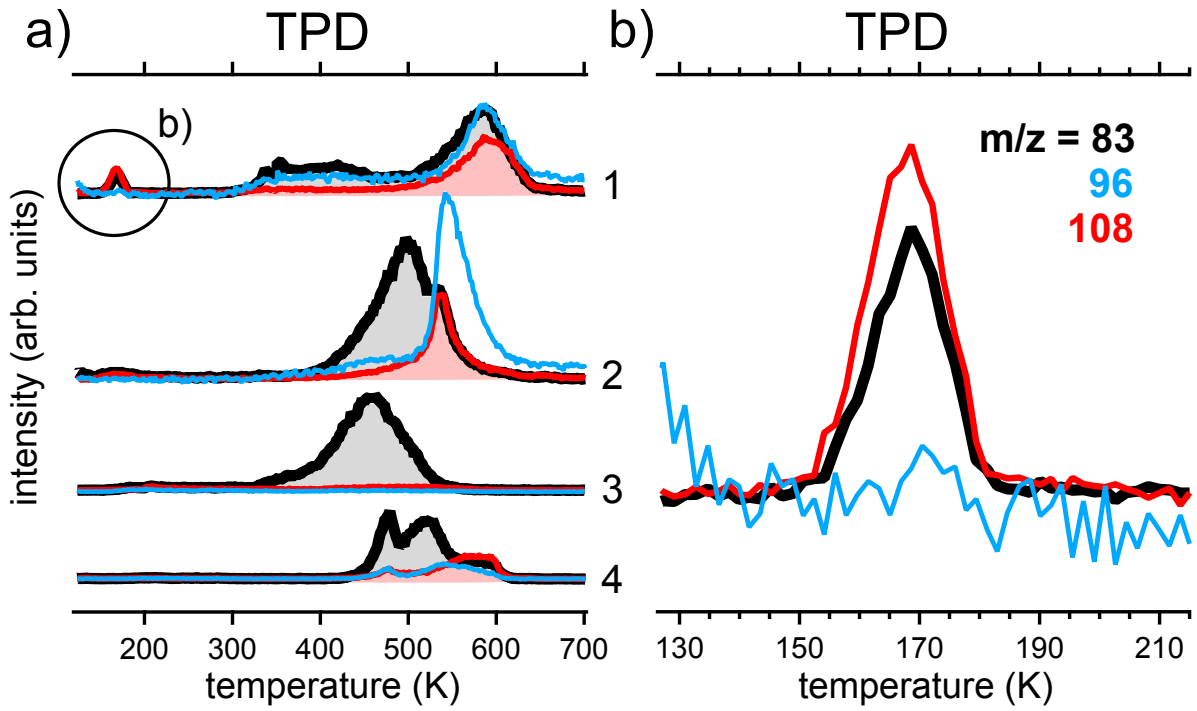

Figure 6.11: a) TPD spectra for mass-to-charge ratios $m/z = 83$ (black), $m/z = 96$ (light blue) and $m/z = 108$ (red) of (1) the 4-FTP SAM on Ag(111), (2) FePc on the 4-FTP SAM/Ag(111), (3) a higher coverage of FePc (as compared to the system in 2) on the 4-FTP SAM/Ag(111) and (4) Ru(CO)TPP on the 4-FTP SAM/Ag(111). The TPD spectra have been recorded in the temperature range of 120 - 700 K with a heating rate of $0.5\,\mathrm{K\,s^{-1}}$. b) Zoom-in into the 4-FTP desorption feature in TPD spectrum 1 at around 170 K.

well suited for chemical discrimination of the thiol species and the species associated with thiolate radical detection. This assumption is confirmed by additional data presented in appendix A.3, Fig. A.4, where TPD spectra for $m/z = 127$ and 128 are reported, which show a striking similarity of the latter (the parent thiol species with $m/z = 128$) to the fragment $m/z = 108$ and of the former (the thiolate radical or doubly ionized disulphide species) to the fragment $m/z = 83$. Fluorobenzene differs from these two species by its characteristic predominant signal at $m/z = 96$.

With reference to Fig. 6.11b, the desorption of intact 4-FTP in spectrum 1 (Fig. 6.11a) at ∼170 K yields the fingerprint (i.e. the fragmentation pattern) of the thiol species. Additionally, the absence of an appreciable desorption feature at $m/z = 96$ suggests the absence of concomitant fluorobenzene desorption as well as of noticeable fragmentation into this product. In contrast, in spectrum 1 of Fig. 6.11a the 4-FTP SAM on Ag(111) appears to desorb in the form of all three species, namely the species detected as thiolate radical (i.e. the thiolate-related species), the intact thiol (as e.g. observed in Ref. [234] for cyclohexanethiol on Au(111)) and fluorobenzene, with desorption maxima at around 585 K. The presence of these desorption products can be discerned by qualitative comparison to the spectra in Fig. 6.11b, which show predominant thiol desorption. Specifically, in spectrum 1 of Fig. 6.11a the distinct signal in mass 96 signals fluorobenzene desorption, while the increased intensity of mass 83 compared to mass 108 indicates desorption of the thiolate-related species along with thiol desorption. For the case of FePc deposited onto the 4-FTP SAM, as shown in spectrum 2 in Fig. 6.11a, the desorption behaviour is clearly different. Here, the SAM molecules first leave the surface as a species that is detected as thiolate (peak at 500 K), and subsequently as thiol and fluorobenzene (sharp desorption maxima at ∼540 K). Interestingly, at slightly increased coverage of FePc (cf. TPD spectrum 3) thiol and fluorobenzene desorption appear to be completely quenched, with only the thiolate-related species of $m/z = 83$ desorbing. This behaviour corroborates the view that prior to thermal desorption of the 4-FTP SAM, the FePc molecules "slip" underneath the SAM at ∼175 K and, at sufficient FePc coverage, prevent the thiolate bond of 4-FTP with the Ag substrate. In agreement with the different desorption behaviour observed in spectrum 2 and 3, we suggest that this blocking of the surface inhibits both C-S bond scission and the recombinative desorption of FC_6H_4S- and FC_6H_4-radicals with hydrogen atoms (assuming that both processes are directly mediated by the silver surface) to yield thiol and fluorobenzene, while it becomes more likely for the thiolate radical species to either directly desorb or couple and leave the surface as disulphide ($m/z = 83$). In spectrum 2, the deposited amount of FePc may not be enough to fully cover the metal surface, thus leaving part of it accessible to the SAM and allowing for the recombinative thiol and fluorobenzene desorption. Here, also note that thiol and fluorobenzene desorption take place at a higher temperature than the desorption of the thiolate-related species, suggesting that the thiolate-Ag bond is stronger than the binding of 4-FTP after FePc intercalation. However, it needs to be considered that the suggested desorption

of both intact thiol and fluorobenzene molecules requires a reservoir of atomic hydrogen on the surface. In this regard, one could tentatively propose that upon S-H cleavage during formation of the SAM, a part of the split hydrogen atoms remains bound to the Ag(111) surface (cf. butanethiol on Au(001) [235]) with only a fraction of it desorbing as H_2 (Fig. 6.3b), or, alternatively, for thiol or fluorobenzene desorption the hydrogen is abstracted from coadsorbed molecular species. Former assumption is in apparent contrast with previous studies showing that chemisorbed atomic hydrogen recombines and desorbs as H_2 from Ag(111) below 200 K [236–238]. Nevertheless, diffusion of H into the subsurface upon saturation of the surface with a molecular organic layer cannot *a priori* be ruled out. Considering the intact 4-FTP desorption, we also argue that the detected thiol signal indeed corresponds to thiol desorption and does not primarily originate from desorbed thiolate species *via* hydrogen abstraction from surfaces inside the mass spectrometer [239]. The rationale for this argument is that the signals ascribed to thiol desorption from the here considered SAMs closely resemble the fragmentation pattern and intensity ratios around $m/z = 108$ and 128 for 4-FTP multilayer desorption below ∼200 K (cf. Fig. A.5 in the appendix). The latter is clearly different from the desorption pattern ascribed to predominant thiolate/disulphide desorption (cf. mass-to-charge ratios $m/z = 127$ and 128 in Fig. A.4 and the desorption patterns in Fig. A.5). In general, no consensus regarding the fate of the hydrogen of the SH group on Au and Ag surfaces has been achieved [183], which, in agreement with the variety of desorption channels observed in the presented investigation, rather indicates a strong correlation with the investigated systems. In our case it also has to be noted that reference H_2-TPD spectra from the clean Ag(111) surface (not shown) did not evidence any hydrogen desorption. Regarding the unsolved nature of the detected thiolate-related species, one should note that desorption as thiolate radical or as disulphide was shown also to critically depend on the investigated system, in particular the specific molecules, the molecular density of the SAM, associated steric constraints and the molecule-substrate interaction [233, 234, 240, 241].

Importantly, for Ru(CO)TPP on the 4-FTP SAM (Fig. 6.11a, spectrum 4), the 4-FTP desorption behaviour is qualitatively similar to the FePc case (spectrum 2). However, the origin of the sharp desorption features at ∼480 K could not be resolved and reflects an additional desorption channel of still unknown origin.

To conclude, for the considered 4-FTP SAM on Ag(111) the TPD data suggest that clean patches of the surface need to be accessible for the thiolate species to recombinatively desorb as intact thiol. The same holds for the desorption of fluorobenzene, following the dissociation of 4-FTP *via* scission of the anchoring C-S bond. A further implication is that these two desorption channels can potentially be switched off by blocking the Ag(111) surface by the intercalation of a molecular layer (FePc or RuTPP). The hydrogen needed for recombinative thiol or fluorobenzene desorption may originate from the inital S-H bond cleavage upon SAM formation, trapped on the (sub)surface until SAM desorption, or is simply abstracted from the coadsorbed molecular species. In addition, upon intercalation

of FePc and RuTPP at temperatures above 175 K and 240 K, respectively, no distinct loss of 4-FTP is detected in the TPD spectra of Fig. 6.11a, indicating that the 4-FTP molecules remain adsorbed on top of FePc/Ag(111) and RuTPP/Ag(111), respectively, and on free areas of bare Ag.

6.4 Conclusion

By a combination of LEED, XPS, TP-XPS and TPD measurements we shed light on the thermal evolution of two prototypical organic/organic/metal junctions, comprising a macrocyclic metal-organic complex deposited onto an aromatic self-assembled monolayer of 4-FTP on Ag(111). At low temperatures, the latter is shown to act as molecular spacer layer that effectively decouples, both spatially and electronically, a FePc and a Ru(CO)TPP layer from the underlying silver substrate. The system evolution is summarized in Fig. 6.12. Saturation exposure of the Ag(111) surface at 300 K to 4-FTP leads to the formation of a well-defined thiolate-bonded SAM, whereby part of the hydrogen atoms originating from S-H bond scission desorbs associatively as H_2 (cf. situation 1 in Fig. 6.12) and a remaining fraction – as a possible explanation for the observed recombinative thiol and fluorobenzene desorption – may still reside on the (sub)surface. A FePc and Ru(CO)TPP layer deposited directly on top of the SAM at low temperature remains physically decoupled from the Ag(111) surface (situation 2 in Fig. 6.12). Moderate annealing (175 K and 240 K for FePc and Ru(CO)TPP, respectively) leads to the breakdown of this decoupling. The experiments evidence that this involves the metal-organic complexes coming into direct contact with the silver substrate and progressively displacing the SAM molecules from the surface to yield an inverted layer (Fig. 6.12, situation 3; note that the depicted morphology has merely suggestive character). In the case of Ru(CO)TPP this also causes the loss of the protecting CO ligand. At higher temperatures the 4-FTP molecules desorb, leaving the surface either as thiolate radical or disulphide species (as tentatively illustrated in Fig. 6.12), or as intact thiol and fluorobenzene. The desorption as thiol or fluorobenzene is attributed to the direct interaction with the bare Ag surface, facilitating both the scission of C-S bonds as well as allowing for the recombinative desorption with atomic hydrogen. This channel can be effectively blocked by increasing the coverage of the metal-organic complexes. Finally, the FePc or RuTPP layers remain on the surface up to 700 K (Fig. 6.12, situation 4). Regarding the inverted layer (situation 3), as no 4-FTP desorption yet occurs upon intercalation of the metal-organic complexes and breaking of the Ag-S bond, one might speculate that either the dehydrogenated 4-FTP species individually interact with the Fe or Ru metal centres of the organic complexes or link together as disulphide species. The former scenario is unlikely, as the absolute coverage of the metal-organic complexes is deemed to be a factor 3-4 smaller than the 4-FTP coverage and no indication of sulphur to Fe/Ru bonding is given by the TP-XPS data. The latter scenario would be in agreement with the detection of the thiolate-related

species in TPD, possibly being a fragment of desorbing disulphide upon further heating. However, typical S $2p_{3/2}$ XPS binding energies for organic disulphides are in the range 163-163.2 eV [242, 243], 0.7-0.9 eV higher than found here, although lower values might be expected upon interaction with the metal centres (cf. pyrite [244]). For the inverted layer in situation 3, a conclusive assignment of the 4-FTP-related species is therefore not possible with the employed techniques.

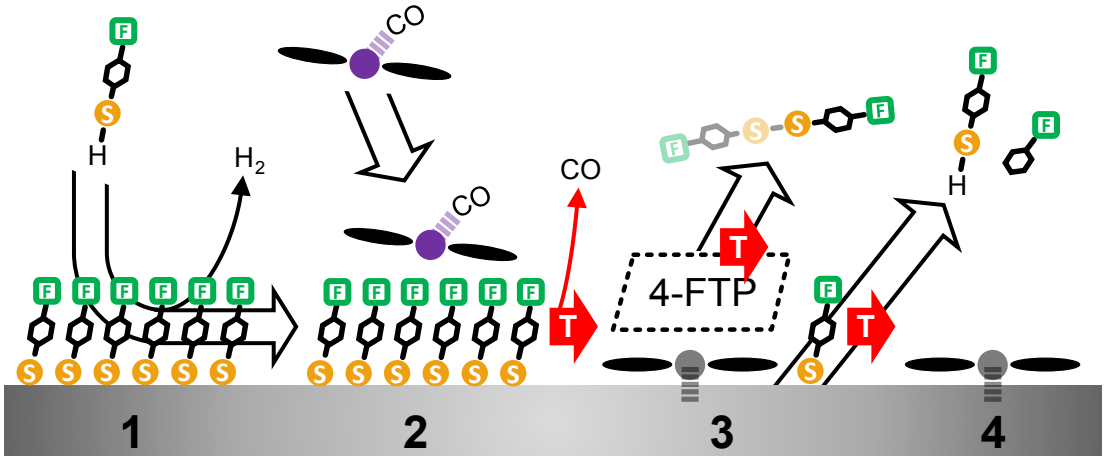

Figure 6.12: Schematics of the thermal evolution of the metal-organic complexes (FePc, Ru(CO)TPP) deposited onto the 4-FTP SAM on Ag(111): (1) thiolate-bonded 4-FTP SAM on Ag(111); (2) metal complex on top of the SAM at low temperatures, spatially decoupled from the Ag(111) surface; (3) breakdown of the spatial decoupling after increasing the sample temperature, with the metal complex in direct contact with the Ag(111) surface; (4) metal complex in direct contact with the Ag(111) surface after thermal desorption of the 4-FTP SAM.

Different systems have been so far investigated to ensure selective decoupling of metal-organic complexes – and organic molecules in general – from metal substrates, including insulating sodium chloride nanolayers [245, 246], metal oxide ultrathin films [247], hexagonal boron nitride [248–250], a copper nitride layer [251], and the oxygen pre-coverage of a metal surface [252]. Here, we have focused on thiolate-anchored self-assembled monolayers. Our study on Ag(111) shows that the 4-FTP SAM can be regarded as a thermally removable spacer layer, whereby the occurrence of molecular displacement and molecular exchange does not ensure physical decoupling at room temperature. A moderately higher thermal stability (∼60 K) is, however, found for the Ru(CO)TPP/4-FTP/Ag(111) system over FePc/4-FTP/Ag(111). Our findings, and the comparison with previous work on gold [198, 199, 201, 204], suggest that the choice of the metal substrate and the SAM's anchoring group may be crucial to shift the stability of the junction towards higher temperature. In fact, recent work on organic-organic heterostructures on metals has shown

that the strength of the organic-metal interaction is a decisive factor for the bilayer arrangement [253]. We also envisage that the interaction of the SAM's end group with the metal-organic complexes as well as the chain-to-chain interaction within the SAM itself may provide additional degrees of freedom to weaken the ability of the metal-organic complexes to penetrate through the SAM. Nevertheless, for sufficiently low temperatures the here considered 4-FTP SAM can indeed be employed as a decoupling spacer between the MP and MPc overlayers and the silver surface, preventing charge transfer from the latter into the molecules' metal centres. In general, such a decoupling approach may be useful, e.g., for catalytic and photocatalytic studies of "immobilized" tetrapyrrole complexes, where substrate-mediated charge transfer and the rapid quenching of photo-excitations by the metal should be avoided. Another practical aspect emerging from our results is that, upon mild heating, the considered SAM could provide a protective layer for, specifically, reactive MP and MPc species, "buried" underneath the SAM. While our study exemplarily demonstrates the feasibility of using SAMs for spatial and electronic decoupling, it also shows that the flexibility of the molecular design of the SAM is critical for the actual application and optimization of the approach.

7 Photochemistry on Surfaces

7.1 Introduction

As outlined in section 3.3, it is highly desirable to expand our surface science toolbox appropriately to induce and investigate light triggered chemical reactions. Specifically, as heterogeneous photocatalysis relies on the excitation and subsequent charge or energy transfer across the interface between a solid catalyst and a molecular reactant [254], well controlled surface science conditions provide ideal prerequisites to reveal and understand the underlying physics of such processes at the atomic level. This is essential for practical exploitation in tailor-made applications. In this regard, as described in section 3.3, a low cost and highly versatile UHV compatible LED-based re-entrant light source has been devised in this work, providing our UHV setup with high intensity illumination at selected wavelengths in the visible range (400 - 700 nm) and down to the UV regime (e.g. 365 - 370 nm).

In order to demonstrate the capability of this self-made light source, this chapter presents proof-of-concept investigations on two different systems in which the exposure to UV light induces either a chemical change of an adsorbate species or its removal from the surface. In the first considered case, exposure to UV light triggers the dehalogenation of a brominated precursor adsorbed on a metal support. Here, the scission of the C-Br bond is ascribed to the light-induced generation of "hot" electrons in the metal substrate. In the second considered case, glycine adsorbed on rutile $TiO_2(110)$ is removed from the surface by UV exposure. Here, the light-induced desorption of molecular fragments is tentatively ascribed to excitation of electrons across the band gap in the photoactive support. Both adsorbate systems have been previously characterized in the master's thesis of F. Haag [255], therefore the presented photo-induced study largely relies on the preparation conditions, experimental results and physical understanding achieved in that extensive groundwork.

7.2 Light-Induced Dehalogenation on Ag(111)

As demonstrated by Basagni et al. in Ref. [55], the light-induced dehalogenation of brominated precursors may have beneficial application in Ullmann coupling reactions on surfaces. In general, surface-assisted Ullmann coupling reactions have received much attention in recent years as they afford a promising strategy to the polymerization of organic

building-blocks towards the creation of robust covalently-bonded networks [19, 62]. Specifically, in Ref. [55] it was shown that, after exposure to 405 nm light for 12 h while keeping the Au(111) substrate at RT, mild annealing to temperatures below the threshold for thermal C-Br dissociation on gold already yielded ordered organometallic networks of an applied sterically hindered precursor. Although the reaction mechanism itself was not in the focus of that work, similar to Basagni et al. it can be suggested that the observed photodissociation of the carbon-halogen bond is mediated by photoexcited "hot" substrate electrons [256–260]. Thus, from a general perspective, even though electronic excitations of adsorbed molecules can be quenched by the supporting metal substrate [259, 261], the photoexcitation of substrate electrons itself represents a viable route to induce photochemical reactions on metal surfaces. To this end, and with the aim of further investigating and confirming the light-induced on-surface dehalogenation of brominated precursors, 6-bromo-N-(p-tolyl)pyridin-2-amine (BTPA) supported on Ag(111) has been investigated here and upon exposure to UV light using the light source described in section 3.3.

7.2.1 Experimental Details

The experiments on BTPA on Ag(111) have been performed in the custom-made UHV chamber described in section 3.1, utilizing the Phoibos 100 analyzer and non-monochromatized $Mg\text{-}K\alpha$ emission (photon energy: 1253.6 eV) for the XPS measurements. The XP spectra in Fig. 7.1 have been acquired in grazing emission geometry (GE), using a pass energy of 15 eV, open exit slit, entrance slit 5, medium area (MA) lens mode and keeping the Ag(111) sample at 85 K. The binding energy of all XP spectra is calibrated against the Ag $3d_{5/2}$ core level of the Ag(111) substrate at a binding energy of 368.27 eV [206]. A clean Ag(111) surface was prepared by sputtering the Ag(111) single crystal at 300 K (RT) with Ne^+ ions for 25-40 min. After sputtering, the surface order was restored by annealing the Ag(111) crystal to 725 K for 5 min, with heating and cooling performed at fixed rates of $1\,\mathrm{K\,s^{-1}}$ and $-1\,\mathrm{K\,s^{-1}}$, respectively. The 6-bromo-N-(p-tolyl)pyridin-2-amine molecule (BTPA, shown in Fig. 7.1a) was synthesized by Dr. Guillaume Médard at the Chemistry Department of the Technical University of Munich. The high vapor pressure of the BTPA powder at RT allowed for facile deposition in UHV in the following manner: a gate valve connected to the vial containing the molecular powder was opened to the chamber, with the Ag(111) sample positioned in line of sight of the respective chamber port. BTPA evaporation was performed for 20-25 min, at chamber pressures of $\sim 5 \times 10^{-11}$ mbar and with the Ag(111) sample at 85 K. Latter allows to adsorb the BTPA intact, avoiding thermal C-Br dissociation starting slightly above 200 K [255]. UV light exposure was performed by means of the re-entrant light source devised in section 3.3, utilizing a 365-370 nm ($\sim$3.4 eV) LED (LZ1-00UV00, LED Engin, Inc.) at operating current of 0.7 A, the sample at 85 K and the light source in very close position to the sample, as depicted in Fig. 7.1b. During BTPA deposition and light exposure as well as during the XPS measurements, the combination of a cold trap and a titanium sublimation pump was applied to reduce

the chamber background pressure to a minimum and minimize spurious physisorption of residual gas molecules onto the Ag(111) surface kept at low temperature (85 K). The Br 3*d* XP spectra of Fig. 7.1c have been fitted with the FitXPS software [207], utilizing a parabolic background.

7.2.2 Results and Discussion

Fig. 7.1c shows the Br 3*d* XP spectrum of the as-deposited BTPA on Ag(111) (black dots) and of the same system after annealing to 300 K for 5 min (grey dots). The as-deposited system shows Br 3*d* core-level lines at 70.8 eV ($3d_{5/2}$) and 71.9 eV ($3d_{3/2}$), with the 3*d* multiplet peaks being split by 1.09 eV. The $3d_{5/2}$ peak at 70.8 eV is, compared to a reported value of 70.4 eV in Ref. [262], indicative of an intact C-Br bond and, as a result, intact BTPA molecules. In contrast, after annealing to 300 K, the Br 3*d* lines are completely shifted to lower binding energies, indicating the thermal dissociation of the carbon-halogen bond [263], with the bromine atoms remaining chemisorbed on the Ag(111) surface. The corresponding Br 3*d* binding energies are 68.2 eV ($3d_{5/2}$) and 69.2 eV ($3d_{3/2}$), with a splitting of 1.03 eV. These values are in accord with reported binding energies for Br bound directly to the Ag surface in Refs. [262, 264]. Importantly, considering the XP spectra in Fig. 7.1d, UV light exposure has an effect similar to the thermally induced C-Br bond scission shown in Fig. 7.1c. Starting with the Br 3*d* spectrum of the as-deposited, intact BTPA at 85 K (black line), with increased UV exposure periods from 130 to 360 min (light blue to dark blue curves) a progressive enhancement of the signal from the surface bonded Br species is observed, gradually approaching the grey spectrum that represents complete (thermal) debromination. In the specific case, and especially when compared to the published results of Basagni et al. in Ref. [55] (405 nm exposure for 12 h on a Au(111) support at RT), the observed light-induced changes are very pronounced. Finally, considering the XP spectra shown in Fig. 7.1e, also prolonged exposure to X-rays induces a chemical change in the Br 3*d* features that is very similar to the effect of the UV light, specifically resembling the spectrum after 130 min UV exposure. In the presented case, the system was exposed to the *Mg-Kα* radiation for about 230 min in XPS measurement position (GE), causing a measured drain current of 0.12 µA from the X-ray exposed parts of the manipulator (note that not only the Ag(111) surface but the whole sample holder faces X-ray exposure and contributes to the drain current). This drain current implies the photoemission of a total of $\sim 7 \times 10^{11}$ electrons per second and, as a consequence, $\sim 1 \times 10^{16}$ electrons in the 230 min of X-ray exposure. For comparison, this total number of emitted electrons within 230 min is an order of magnitude greater than the number of Ag(111) surface atoms in an area of 1 cm^2 (the Ag(111) surface has a surface atom density of $\sim 1 \times 10^{15}\,cm^{-2}$). Accordingly, even though the exposed Ag(111) surface does not account for the entire photoemission related drain of electrons, we assume that still a reasonable number of electrons are being excited within and leave the Ag(111) surface, passing through the deposited BTPA overlayer. These electrons, specifically the large

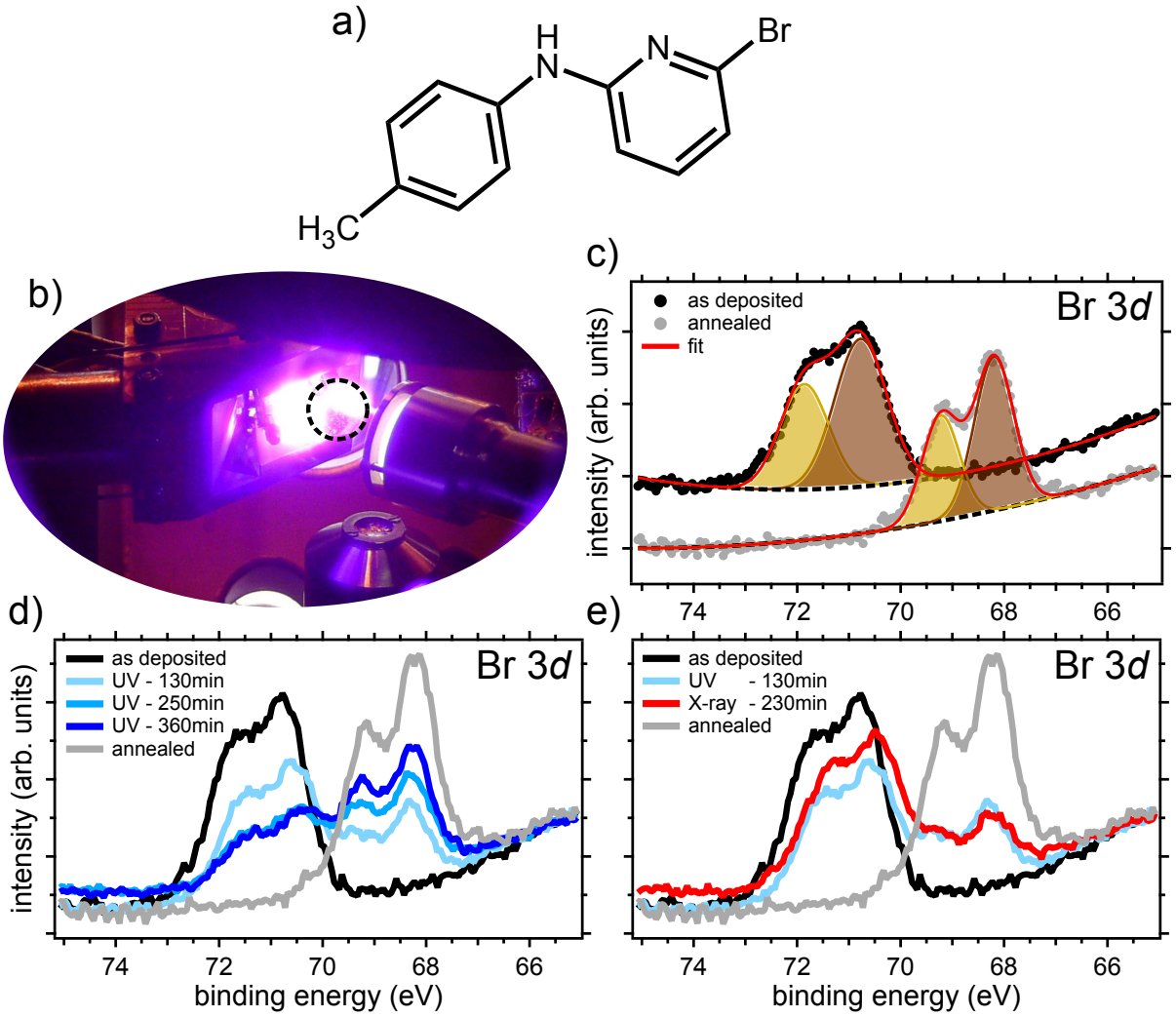

Figure 7.1: Light-induced dehalogenation of 6-bromo-N-(p-tolyl)pyridin-2-amine (BTPA) on Ag(111). a) Chemical structure of BTPA. b) Re-entrant light source in operation, equipped with a 365-370 nm LED and positioned very close to the sample for UV light exposure. The position of the sample is highlighted by the dashed black circle. c) Fitted Br 3*d* XP spectra for BTPA on Ag(111), as deposited at 85 K (black dots) and after having been annealed to 300 K for 5 min (grey dots). d) Comparison of the Br 3*d* XP spectra after UV light exposure of the as-deposited BTPA/Ag(111) at 85 K and for different amounts of time (130, 250 and 360 min, respectively). e) Comparison of Br 3*d* XP spectra after UV light and X-ray exposure (for 130 and 230 min, respectively) of the as-deposited systems. The Br 3*d* spectra for as-deposited (black line) and annealed systems (grey line) are shown as reference for the intact and the completely debrominated BTPA. All XP spectra have been recorded at 85 K.

fraction of inelastically scattered electrons and secondary electrons created in cascade processes with low kinetic energy, can be responsible for inducing the chemical changes of BTPA observed after X-ray exposure (cf. Refs. [265, 266]). Thus, although it cannot be resolved whether "hot" electrons excited below the vacuum level only (cf. Ref. [257]), here created by absorption of ∼3.4 eV photons or upon X-ray exposure, or also low energy electrons passing through the BTPA overlayer during X-ray exposure induce the observed dehalogenation of BTPA, the similarity of the results for both UV- and X-ray exposure in Fig. 7.1e strongly points to the process being caused by photoexcited substrate electrons (as already suggested by Basagni et al. [55]), rather than by direct photo-excitation of the adsorbed molecule.

7.3 Light-Induced Desorption from Rutile TiO_2(110)

TiO_2 is a well-known photocatalyst. The photocatalytic properties rely on its semiconducting nature, whereby photons with energy higher than the band gap (∼3 - 3.3 eV for bulk TiO_2 [254, 267, 268]) can excite electron-hole pairs inside the material [254, 268]. With this excitation the semiconductor becomes reactive, allowing for (interfacial) charge transfer between semiconductor surface and adsorbate species, and thus, it is able to induce oxidation and reduction reactions [254].

Motivated by this intrinsic photoactivity of TiO_2, in the presented experiments we investigate the effect of above band gap excitations on glycine (Gly, Fig. 7.2a) adsorbed on rutile TiO_2(110), utilizing ∼3.4 eV photons. The adsorption structure of Gly on rutile TiO_2(110) has already been investigated by Lerotholi et al. in Ref. [269], revealing that, at coverages up to a monolayer (ML), Gly is adsorbed in the form of glycinate and anchored above two five-fold-coordinated surface titanium atoms *via* its two carboxylate oxygen atoms. In addition, for coverages exceeding the ML, Lerotholi et al. confirmed that Gly is present in the zwitterionic form with COO^- and NH_3^+ functional groups.

Here, starting with initial Gly coverages exceeding the ML, XPS and mass spectrometry measurements reveal that UV light exposure causes a progressive reduction of the Gly overlayer thickness, almost restoring the uncovered TiO_2 surface. This is associated with the desorption of molecular fragments.

7.3.1 Experimental Details

Similar to section 7.2, the experiments on Gly on rutile TiO_2(110) have been performed in the custom-made UHV chamber described in section 3.1, by means of the Phoibos 100 analyzer and non-monochromatized $Mg\text{-}K\alpha$ emission. All the XP spectra have been acquired in normal electron emission geometry (NE), using a pass energy of 15 eV, open exit slit, entrance slit 5 and large area (LA) lens mode. While the background spectra of the clean TiO_2 surface have been acquired at a sample temperature of 300 K, all other XP

spectra were recorded with the sample kept at 200 K. XP spectra are calibrated against the Ti $2p_{3/2}$ core level of the TiO_2(110) substrate at a binding energy of 459.3 eV [267]. The mass spectrum monitoring the UV light induced desorption from Gly adsorbed on TiO_2(110), as illustrated in Fig. 7.3c, was recorded with TiO_2 sample, re-entrant light source and the mass spectrometer (cf. section 3.1) arranged such that both the light exposure and the detection of desorbing molecular species from the surface was possible simultaneously. For this, the sample was positioned under the Feulner-cap aperture with a slight sideward tilt of ∼35°, moving the surface normal away from the entrance axis of the mass spectrometer (cf. experimental arrangement shown in Fig. 7.3f). Furthermore, background signals at the mass-to-charge ratios (m/z) 20, 21, 22 and 40 were subtracted from the spectrum in Fig. 7.3c for the clarity of presentation. These signals are ascribed to neon and argon atoms, present in the residual gas of the UHV chamber after sample sputtering. To minimize the background pressure during the experiments and to avoid adsorption of contaminants onto the TiO_2 surface, both the Feulner-cap of the mass spectrometer (for mass spectrometry measurements only) and an additional cold trap serve to pump residual gases *via* deposition of a reactive titanium getter film and cryogenic trapping by liquid nitrogen cooling (cf. section 3.1). The rutile TiO_2(110) crystal (square-shaped, 10×10 mm^2, PI-KEM Ltd.), glued onto a molybdenum backplate *via* a mixture of Aremco Ceramabond 503 and Graphi-Bond 551-RN, was cleaned by repeated cycles of sputtering at 300 K with Ne^+ or Ar^+ ions and annealing to 930 K for 20-30 min, with both heating and cooling performed at ∼5 K s^{-1} [255]. The performed heating in vacuum leads to bulk reduction and *n*-type doping [267, 270], rendering the TiO_2 crystals conductive (cf. preparation conditions in Refs. [267, 271]) and, as a result, suited for XPS investigations. For the here considered measurements, however, the multiple preceding cycles of sputtering and annealing with neon and without O_2 treatment may have caused progressive deterioration of the surface structure of the TiO_2 crystal, likely resulting in an increasingly reduced and roughened surface and the onset of shear plane formation (cf. Ref. [272]), as judged by LEED. As a result, the precise surface morphology of the TiO_2 crystal is not known. Glycine (Sigma Life Science, ≥99 %) was deposited from a quartz glass crucible by means of a home-built molecular beam evaporator at 390 K, with the TiO_2 crystal kept at 200 K. At this temperature, the sample was then subject to subsequent XPS measurements and light exposure. UV light exposure was performed by the same means as mentioned in section 7.2, utilizing 365-370 nm (∼3.4 eV) LEDs (LZ1-00UV00, LED Engin, Inc.), operated at a current of 0.7 A. During the light exposure the sample was kept at 200 K, with either the re-entrant light source in very close position to it, just as depicted in Fig. 7.2b, or further apart, as shown in Fig. 7.3f, to allow for simultaneous recording of mass spectra.

7.3.2 Results and Discussion

After Gly deposition with the TiO_2 sample kept at 200 K, the corresponding N 1*s* XP spectrum in Fig. 7.2c (black curve) shows the presence of two distinct chemical species, indicative of Gly coverage exceeding the ML [269]. Here, the weaker, low binding energy shoulder at around 400.3 eV, which closely resembles the N 1*s* signal of a monolayer of Gly on TiO_2 (cf. ML reference, red curve, from Ref. [255]), is ascribed to the glycinate species directly bound to the TiO_2 as reported in Ref. [269]. The dominant species at a binding energy of ∼402.5 eV, in contrast, is attributed to the physisorbed Gly above the glycinate ML, and existing in the zwitterionic form. For comparison, glycinate and zwitterionic N 1*s* contributions in a saturation layer formed by Gly deposited onto TiO_2(011) at 300 K were associated with binding energies of 400.0 eV (glycinate) and 401.8 eV (zwitterion), respectively, in Ref. [273]. Furthermore, an energy splitting between the two species of 2.3 eV has been reported in Ref. [269] (where, however, the XPS binding energy scale was not calibrated). The latter value is in excellent agreement with our findings. Similarly to N 1*s*, the C 1*s* XP spectrum shown in Fig. 7.2d (as deposited, black curve) also indicates the presence of an initial Gly overlayer that exceeds a ML coverage (cf. ML reference, red curve), with two chemically distinct C 1*s* species at binding energies of ∼287.2 eV and ∼289.4 eV and of almost equal intensity. The corresponding C 1*s* binding energies found for the 300 K saturation layer in Ref. [273] amount to 286.7 eV and 289.2 eV, respectively, where the 1:1 intensity ratio of the two carbon features is ascribed to adsorption of the intact glycinate molecule. In each case, the high binding energy C 1*s* species is associated with the deprotonated carboxyl group (either of the surface-bonded glycinate or the zwitterionic species in the condensed multilayer), the low binding energy species with the carbon atom bonded to the amino group. Comparing the as-deposited system to the ML reference in Fig. 7.2d, the high binding energy component of the monolayer is only slightly red-shifted by ∼0.1 eV, whereas the low binding energy component is red-shifted by ∼0.3 eV. The latter more pronounced shift is related to the presence of the zwitterion (NH_3^+) on top of the glycinate (NH_2) ML in the as-deposited system, whereas the rather unaffected high binding energy species confirms the presence of the similar carboxylate group in both the glycinate and zwitterionic species.

After UV light exposure (365-370 nm, ∼3.4 eV) for 150 min, with the re-entrant light source in very close position to the sample (Fig. 7.2b), apart from minor residues of nitrogen and carbon fragments, the N 1*s* and C 1*s* spectra (blue curves in Fig. 7.2c and d) reveal that most of the Gly overlayer has been removed. Note that during UV light exposure the sample temperature was maintained at 200 K, whereas the glycinate monolayer directly bonded to the TiO_2 surface should remain adsorbed at least up to 550 K [255, 273]. Consequently, the here observed removal of Gly from the TiO_2 surface is clearly induced by the UV light.

In order to reveal the identity of the desorbing molecular fragments, the UV light exposure has been performed with simultaneous detection of a mass spectrum. The

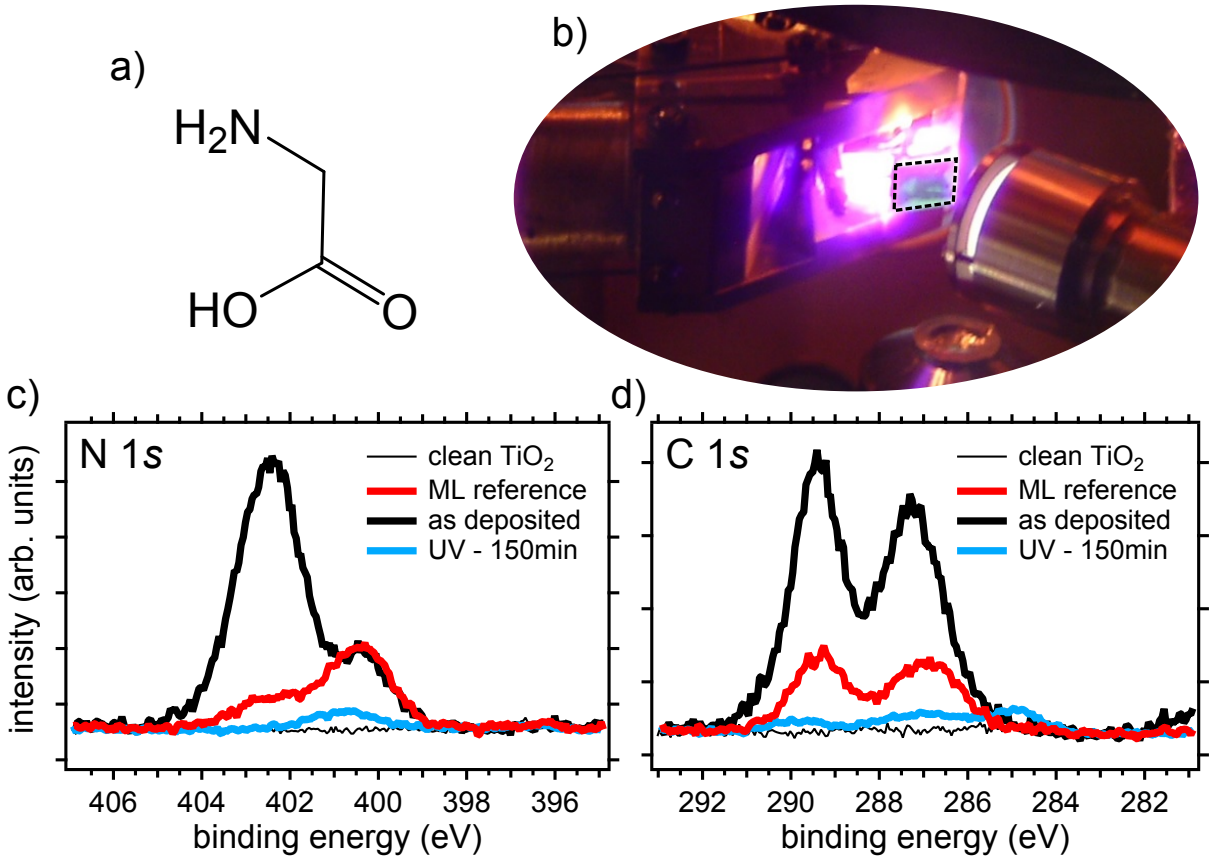

Figure 7.2: Light-induced removal of Gly from rutile $TiO_2(110)$ monitored by XPS: a) Chemical structure of glycine. b) Re-entrant light source in operation, equipped with a 365-370 nm LED and positioned very close to the sample for UV light exposure. The position of the sample is highlighted by the dashed black box. c),d) N 1*s* and C 1*s* XP spectra of Gly on rutile $TiO_2(110)$, as deposited at 200 K (black curves) and after UV light exposure for 150 min at 200 K (blue curves). In addition, both background spectra for the clean TiO_2 surface (thinner black curves) and the spectra of a Gly monolayer on $TiO_2(110)$ (ML, red curves, provided by F. Haag [255]) are shown for reference.

experimental arrangement is shown in Fig. 7.3f. Similar to the previous experiment, Gly has been deposited onto the TiO_2 sample kept at 200 K. Considering the corresponding N 1*s* and C 1*s* XP spectra of the as-deposited system in Fig. 7.3a and b (black curves), direct comparison to the ML reference (red curves) again shows that the initial coverage of Gly exceeds the ML. With the start of the UV exposure at a sample temperature of 200 K, the mass spectrum in Fig. 7.3c shows the instantaneous onset of desorption of molecular fragments of various mass-to-charge ratios. Latter are illustrated by the sum over all mass spectra during light exposure in Fig. 7.3d. The corresponding time evolution of selected mass-to-charge ratios is also shown in Fig. 7.3e, showing both the onset as well as the steplike decrease in the desorption signal when switching the UV light on and off. In agreement with the observed desorption of molecular species in Fig. 7.3c, also the N 1*s* and C 1*s* spectra in Fig. 7.3a and b (blue curves), recorded after the 20 minutes of UV exposure, show drastically reduced intensities, resembling a Gly coverage that is even smaller than the reference ML spectrum. However, even though this clearly shows that a large fraction of the adsorbed Gly has been removed by UV exposure, the respective mass spectrum in Fig. 7.3d does neither show a predominant signal at m/z = 30 (dominant fragment of Gly), nor any signal intensity at m/z = 75 (parent ion of Gly). Both these two mass-to-charge ratios would be expected for the desorption of intact Gly [41, 42]. Note that XPS prior to UV exposure indeed indicates a considerable fraction of the adsorbed Gly present in the zwitterionic form, i.e. it should not have undergone deprotonation to glycinate and thus it would be expected to desorb as intact molecules. In contrast, the major light-induced desorption features are m/z = 28 and m/z = 44, commonly identified as CO and CO_2. Thus, assuming that the deposited Gly is initially intact and exists both as the deprotonated glycinate species and the zwitterionic form, as confirmed by the XP spectrum in Fig. 7.3a (black curve), most of the desorbed Gly does not seem to leave the surface intact. With no clear fingerprint of the Gly being detected in the mass spectrum, more comprehensive investigations are required to determine the nature of the photochemical process that leads to the light-induced removal of Gly. In our study, this is hampered by the fact that the precise surface morphology of the TiO_2(110) surface was deteriorated upon prolonged sputtering-annealing cycles, presumably leading to an increasingly reduced surface. Nevertheless, the light-induced desorption of molecular fragments, as monitored in Fig. 7.3e, is in agreement with the light-induced removal of the Gly overlayer and corroborates the findings illustrated in Fig. 7.2 and the photocatalytic role of TiO_2.

7.4 Conclusion

As demonstrated by way of two very different systems, our home-built, movable LED-based light source – compatible for the application in UHV chambers equipped with DN40 CF (ConFlat) chamber ports – provides light of sufficient intensity to trigger photochemi-

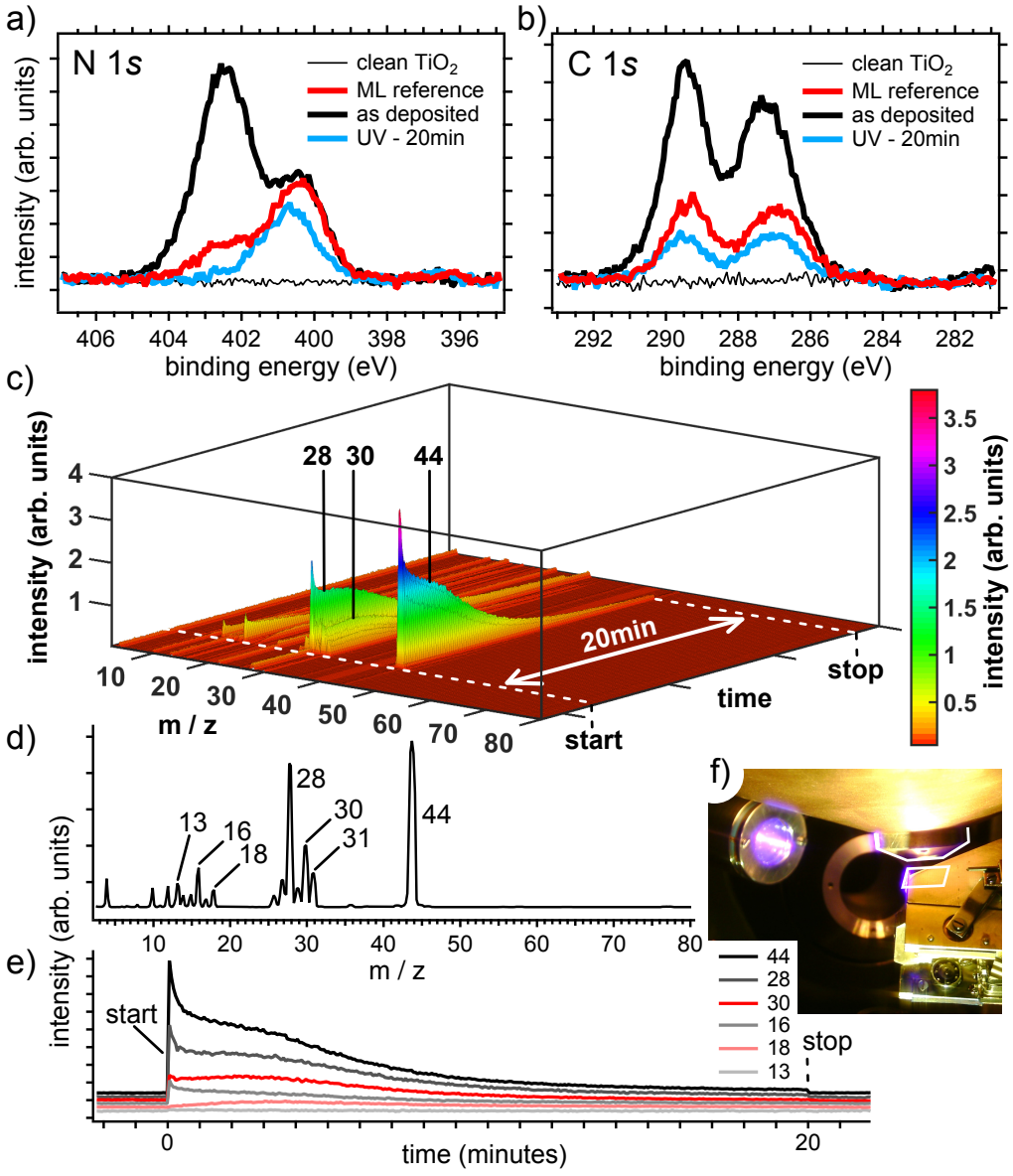

Figure 7.3: Light-induced removal of Gly from rutile TiO_2(110) monitored by mass spectrometry: a),b) N 1*s* and C 1*s* XP spectra of Gly on rutile TiO_2(110), as deposited at 200 K (black curves) and after UV light exposure for 20 min at 200 K (blue curves), with the sample positioned under the mass spectrometer, just as shown in f) (sample and Feulner-cap aperture are highlighted by white solid lines). The ML reference spectra are the same as in Fig. 7.2. c) Corresponding 2D mass spectrum monitoring the mass-to-charge ratio (m/z) of desorbing species for the 20 min period of UV light exposure. d) Sum of all the mass spectra during light exposure in c). The main desorption features are labeled with their m/z ratio. e) Time-dependent desorption signal for selected mass-to-charge ratios in c).

cal reactions on surfaces. Specifically, as seen for BTPA on Ag(111), the ease of triggering reactions by metal substrate excitation *via* the applied LED light represents a promising pathway to further enhance and complement on-surface synthesis and, in the considered case, aids on-surface Ullmann coupling reactions [55]. In the case of glycine adsorbed on rutile TiO_2, even though the underlying physical processes that cause the removal of glycine remain unresolved, the combined application of the LED-based light source and mass spectrometry demonstrates its applicability for the real-time monitoring of photon stimulated desorption and (associated) light-induced reactions.

To conclude, although the here presented proof-of-concept studies are far from comprehensive, the strong effects seen upon LED light exposure motivate to further pursue our approach of using a re-entrant window and high-power LEDs of selected wavelength. Improvements of the presented re-entrant light source are possible. These include the operation of the LEDs at higher currents upon an improved cooling, the replacement of the borosilicate window by a material that is more suited for UV transmission, or even the fusion of the applied lens and window glass by replacing the window glass with a plano-convex lens and, finally, the application of lock-in techniques, using a pulsed LED in combination with mass spectrometry for dedicated photon stimulated desorption studies.

8 Conclusions and Outlook

In the presented thesis, different roles that metal supports can play for (metal-)organic adsorbates have been investigated and revealed by means of a UHV-based surface science approach. Specifically, in consideration of the observed substrate effects, also a molecular spacer layer was introduced in order to physically decouple molecular adsorbates from the underlying metal support. In the following lines, the obtained results are briefly summarized and put into perspective.

In chapter 4, exploiting a repertoire of real-space imaging and spectroscopic tools, the sequential thermal evolution of Diethylstilbestrol (DES) and Bisphenol A (BPA) on a Cu(111) surface has been revealed, eventually leading to the formation of branched molecular chains. Although, at first glance, the rather disordered nature of the final reaction product does not appear desirable for the controlled bottom-up synthesis of covalent organic frameworks, it is the initial step of the covalent coupling of DES and BPA precursors to polymeric chains that turns out to be highly selective. Specifically, by mild annealing of the as-deposited molecules, TPD measurements reveal the complete deprotonation of the terminal hydroxyl groups. This first deprotonation step is assumed to be followed, similar as reported in Ref. [20], by *enol-keto* tautomerization mediated C-H activation at the carbon atoms in *ortho*-position, leading to the subsequent *ortho-ortho* coupling of neighboring molecules in the second step. This particular reaction pattern is verified by the almost identical behavior of DES and BPA in the performed TPD, (TP-)XPS and STM measurements. While TPD reveals the desorption of H_2, already indicative of the covalent *ortho-ortho* coupling, TP-XPS measurements evidence that the concomitant transformation from well ordered molecular overlayers to molecular chains, as monitored by STM, indeed does not involve a chemical change of the oxygen species. Finally, a third H_2 desorption feature, occurring at different temperatures for DES and BPA and accompanied by concomitant desorption of H_2O, signals a further chemical modification of the polymeric chains, associated with oxygen removal and the likely formation of C-O-C bridges and C-C bonds within the disordered polymers, and not compatible with a second *ortho-ortho* coupling step. Even though the third reaction step has additionally led to an increase in disorder, the presence of the branched molecular chains at temperatures up to 540 and 730 K underlines the remarkable thermal stability and robustness of such covalently linked organic frameworks, in turn, making them a promising construction material in nanoscale devices. With respect to the bottom-up synthesis, the here investigated hydroxy-directed coupling mechanism represents a complementary mechanism

that, if combined systematically with the established Ullmann process [19], may further facilitate the approach of sequential and selective C-C coupling to form ever more complex structures in a hierarchical manner [19, 62, 67]. In this regard, future experiments on purposely designed molecular precursors which contain both halogen and hydroxyl groups are envisaged.

In chapter 5, synchrotron-based normal incidence X-ray standing waves (NIXSW) measurements supported by density functional theory (DFT) calculations shed light on the nature of the so-called "surface *trans*-effect" [21, 22]. In such experiments, the vertical displacement of the iron center in iron phthalocyanine (FePc) adsorbed on Ag(111), upon coordination to H_2O and NH_3, can be determined quantitatively and reproduced nicely by theory, once corrections are included for dispersion forces. Most intriguingly, the corresponding DFT calculations reveal that the electronic effect of introducing the Ag(111) surface in *trans*-position to a water molecule, as reflected in the corresponding charge redistribution maps, is extremely similar to the effect of introducing an ammonia molecule *trans* to a water molecule. The Ag(111) surface thus appears to behave similarly to a molecular ligand. Furthermore, as the FePc overlayer is known to be incommensurate with the underlying Ag(111) lattice, the observed "surface *trans*-effect" thus involves the interaction with the delocalised electronic states of the metal substrate rather than the direct interaction with a single substrate atom. Specifically for metal-organic complexes immobilized on metal supports this finding has far-reaching consequences. On the one hand, the influence of the substrate on the reactivity of the metal center needs to be considered from the outset, on the other hand, similar to the influence the substrate has on an incoming ligand in *trans*-position, the latter also exerts influence on the substrate. Such systems, for which the response of the substrate (or the metal-organic complex) towards an incoming ligand would be directly measurable, represent the textbook example of a molecular sensor and call for further investigations directed towards their applicability in realistic devices.

In two proof-of-concept studies in chapter 7, two intrinsically different surfaces, namely Ag(111) and rutile TiO_2(110), have been electronically activated by exposure to ultraviolet (UV) light. In the case of Ag(111), light exposure causes the dehalogenation of the adsorbed brominated precursor 6-bromo-N-(p-tolyl)pyridin-2-amine (BTPA). Here, the scission of the C-Br bond is ascribed to the light-induced generation of "hot" electrons on the metal support. In the case of glycine on TiO_2(110) instead, exposure to UV light leads to the removal of the amino acid from the surface. The latter is tentatively ascribed to above band gap excitation within the photoactive support. Thus, from a general perspective, even though electronic excitations of adsorbed molecules can heavily be quenched by the supporting substrate, the photoexcitation of the underlying substrate itself has to be considered as viable route to trigger photochemical reactions on surfaces. In this regard, especially the observed light-induced, surface-supported dehalogenation [55] represents a promising tool to improve and complement the already

established strategies (like the surface-assisted Ullmann coupling [19]) for the bottom-up synthesis of nano-scaled structures. In addition, both the verified applicability of the devised LED-based re-entrant light source, described in section 3.3, as well as its flexibility in terms of wavelength – LEDs cover almost the entire visible range from 400 - 700 nm and even go down to ultraviolet wavelengths of 265 nm – motivate further investigations directed to tackle the photochemical properties of surfaces and adsorbates.

Finally, in order to "turn off" the strong influence of metal substrates on molecular adsorbates that has been observed in the previous examples, in chapter 6 a self-assembled monolayer (SAM) of 4-fluorothiophenol (4-FTP) is introduced as molecular spacer layer to spatially and electronically decouple the two prototypical metal-organic complexes FePc and ruthenium tetraphenylporphyrin (Ru(CO)TPP) from a Ag(111) surface. For low temperatures ($\sim$150 K), the 4-FTP SAM indeed prevents a direct contact between the metal-organic complexes and the substrate. However, upon annealing to 175 K and 240 K for FePc and Ru(CO)TPP, respectively, the 4-FTP SAM becomes permeable and the organic/SAM/metal-stacking breaks down, with both complexes getting into contact with the Ag(111) surface. This process involves the displacement of the 4-FTP thiolate species from the surface, to yield an inverted layer stacking. In particular, if the deposited amount of FePc or Ru(CO)TPP is not sufficient to completely saturate the silver surface, the remaining surface remains covered by the 4-FTP SAM, which, according to the observed LEED patterns, is then even compressed to a denser phase, indicative of phase separation between 4-FTP and the metal-organic complexes on Ag(111). The thermal evolution of the layer configuration is revealed by characteristic LEED patterns and core-level binding energies and shifts in (TP-)XPS measurements. The experimental findings stress the importance of the structure and, specifically, the thermal stability and "permeability" of SAMs applied for the functionalization of surfaces, which is regarded to be critical for their purposeful application. In our case, as the terminal fluorine group of the SAM is not expected to form a (coordinative) bond with the metal center, the 4-FTP monolayer is merely considered a molecular spacer layer. However, endowing SAMs with appropriate end groups to axially coordinate metallo-porphyrins or metallophthalocyanines (cf. Refs. [199–205]) may provide a direct access to deliberately tune the chemical properties and reactivity of their metal centers towards incoming reactants, which should be addressed in future investigations.

To conclude, by showing a wealth of physical and chemical phenomena on surfaces, the presented experiments stress the relevance and applicability of the classical UHV-based surface science approach for various technologically relevant fields, such as heterogeneous catalysis, the surface-assisted bottom-up synthesis of nanostructures and, in general, the tailored functionalization of surfaces. In this regard, particularly the combination of various different experimental techniques such as (TP-)XPS, TPD, LEED and STM facilitates comprehensive characterization and thus provides a full picture of the system

under investigation.

Appendix

A.1 S *2p* XP Spectra of FePc/4-FTP/Ag(111) after Annealing to 300 K

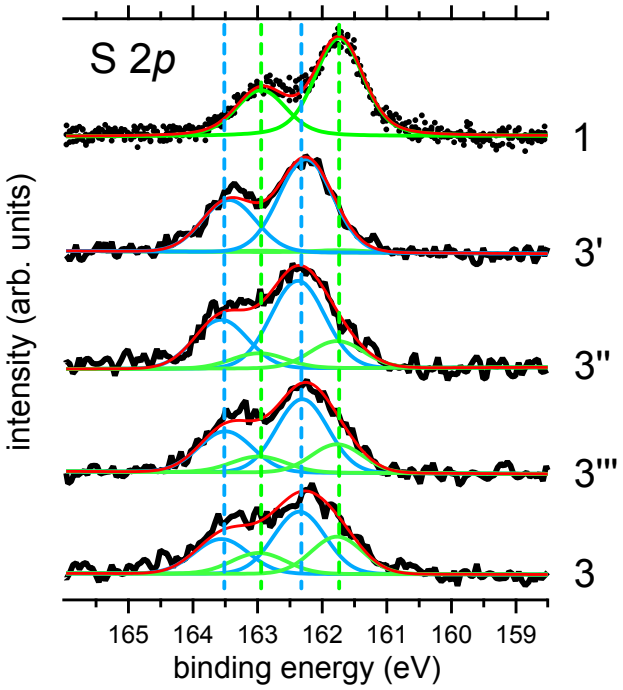

Figure A.1: S 2*p* (NE) XP spectra of (1) 4-FTP SAM on Ag(111), (3)(3′)(3″) FePc deposited onto the 4-FTP SAM on Ag(111) at 90 K, followed by annealing to 300 K, and (3‴) FePc deposited onto the 4-FTP SAM on Ag(111) at 300 K. Spectrum 3‴ has been recorded at 300 K, all other spectra have been recorded at 90 K. Spectrum 3 is recorded on the same system as the LEED pattern in Fig. 6.7d of chapter 6.

Fig. A.1 displays the fitted S 2*p* spectra of FePc deposited onto the 4-FTP SAM on Ag(111) at 90 K, followed by annealing to 300 K (spectra 3, 3′ and 3″), and FePc deposited onto 4-FTP/Ag(111) directly at 300 K (spectrum 3‴). The spectrum of the 4-FTP SAM on Ag(111) (spectrum 1) serves as binding energy reference for the Ag-bound thiolate

species of 4-FTP and, similar to spectrum 3 and 3′, is also displayed in Fig. 6.8a of chapter 6. In contrast to spectrum 3′, for the fit of spectra 3, 3″ and 3‴ the Ag-bound thiolate species of spectrum 1 (green curves in Fig. A.1), with peak positions constrained to 161.75 eV and 162.95 eV for S $2p_{3/2}$ and $2p_{1/2}$ contributions, respectively, needs to be introduced to obtain good fitting. Apart from the dominant S $2p$ features at 162.3 eV and 163.5 eV (blue curves in Fig. A.1), evolving after annealing the systems to 300 K (or by depositing FePc onto 4-FTP/Ag(111) directly at 300 K), this indicates that some of the 4-FTP remains directly bound to the Ag(111) surface as thiolate. We ascribe the remainder of this Ag-bound thiolate species to the deposition of less than a full layer coverage of FePc on Ag(111). Latter, in turn, would be needed to completely displace the 4-FTP from the Ag(111) surface. Also note that spectrum 3 corresponds to the LEED pattern in Fig. 6.7d of chapter 6, corroborating the assumption that it is the remaining surface-bound thiolate species that is compressed to a denser phase. Fitting has been performed with the FitXPS software [207], using two S $2p$ spin-orbit doublets of fixed energy splitting (1.2 eV), fixed 2:1 intensity ratio between the $j = 3/2$ and $j = 1/2$ components and similar FWHM, superimposed onto a linear background.

A.2 XPS (C *1s*, S *2p*) on the Thermal Evolution of FePc/4-FTP/Ag(111)

Fig. A.2 shows the C 1s (NE) XP spectra of the 4-FTP SAM on Ag(111) (spectrum 1), the FePc monolayer on Ag(111) (spectrum 2), the FePc deposited onto the 4-FTP SAM on Ag(111) at 90 K (spectrum 3), and the system of spectrum 3 after annealing to 300 K (spectrum 4). Importantly, in spectrum 4 the C 1s feature at around 286.5 eV, ascribed to the 4-FTP carbon atom bound to fluorine (cf. Fig. 6.4, F-C), is restored. This corroborates the conclusion that upon annealing to 300 K (from spectrum 3 to 4) 4-FTP is displaced from the Ag(111) surface, moving on top of the FePc layer (cf. schematic 4) and preventing attenuation of the associated C 1s features by FePc. In contrast, the 4-FTP related feature at ∼286.5 eV is attenuated by the FePc overlayer in spectrum 3. The C 1s data thus support the intercalation of FePc, as stated in chapter 6.

Fig. A.3 displays the S $2p$ (NE) XP spectra of the 4-FTP SAM on Ag(111) (green spectra, system 1), FePc deposited onto the 4-FTP SAM on Ag(111) at 90 K (light-blue spectra, system 3), and the latter after having been annealed to 300 K (orange spectra, system 4). After deposition of FePc at 90 K, the S $2p$ signal gets moderately attenuated, attributed to FePc sitting on top of the SAM (sketch 3). However, after annealing the systems to 300 K, the pronounced blue shift of the S $2p$ features is accompanied by the increase of the corresponding S $2p$ signal intensity. The overall gain in S $2p$ signal intensity supports the assumption that FePc penetrates the 4-FTP SAM at temperatures above 175 K, coming into contact with the Ag(111) surface and resulting in the inverted layer

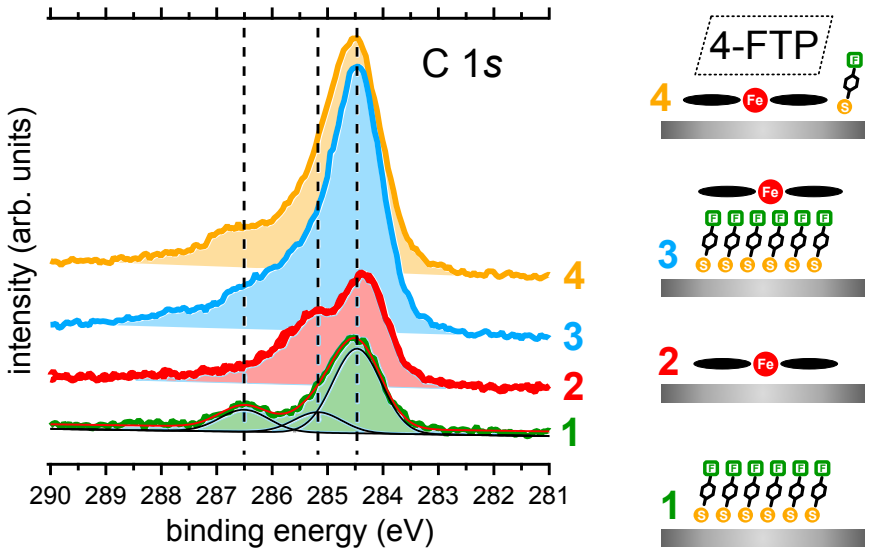

Figure A.2: C 1*s* (NE) XP spectra of (1) the 4-FTP SAM on Ag(111), (2) the saturated FePc monolayer on Ag(111) and (3) FePc deposited onto the 4-FTP SAM at 90 K, followed by (4) annealing to 300 K. All spectra were recorded at 90 K. Spectrum 1, including the fitted peaks, corresponds to the C 1*s* spectrum shown in Fig. 6.4 of chapter 6. Suggested (explanatory) overlayer morphologies are sketched on the right.

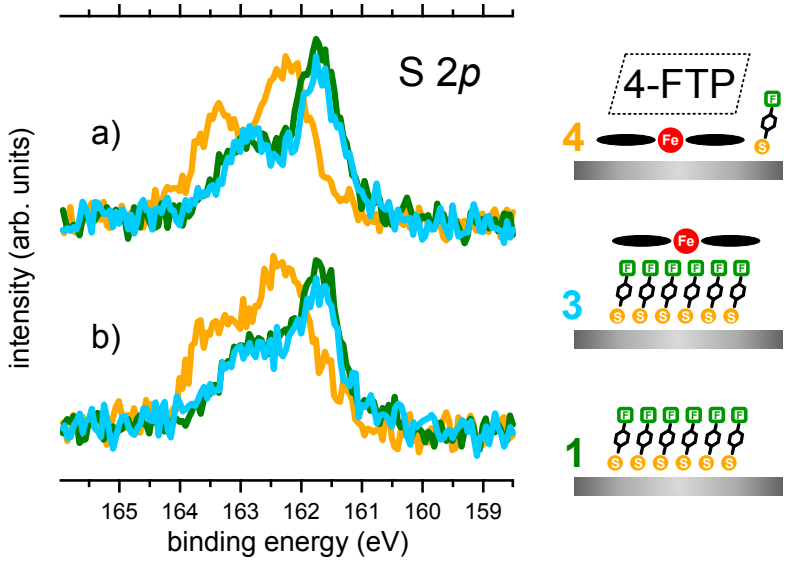

Figure A.3: S 2*p* (NE) XP spectra of the 4-FTP SAM on Ag(111) (green spectra), FePc deposited onto the 4-FTP SAM at 90 K (light-blue spectra), and of the latter system after annealing to 300 K (orange spectra). Panels a) and b) present different preparations. All spectra were recorded at 90 K. Suggested overlayer morphologies are sketched on the right.

stacking illustrated in sketch 4. The ratio of the integrated areas under the S 2*p* spectra of Fig. A.3 amounts to roughly 1 : 0.9 : 1.1 (system 1 : system 3 : system 4), normalized against the S 2*p* intensity of the 4-FTP SAM on Ag(111) (system 1). Thus, also the S 2*p* data support the intercalation of FePc, as shown in chapter 6.

A.3 TPD of 4-FTP/Ag(111) and of FePc and Ru(CO)TPP Deposited on It

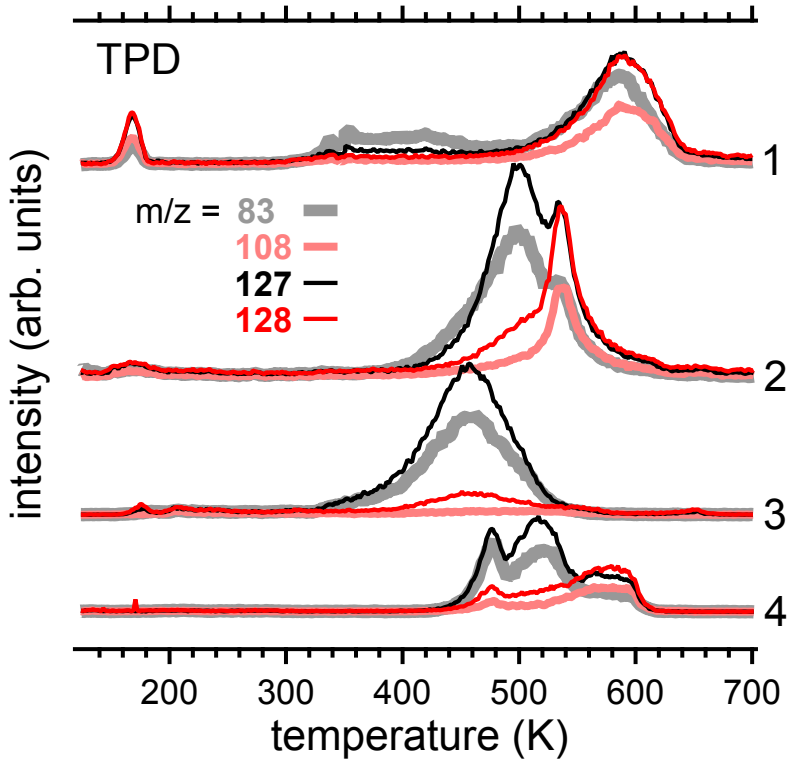

Figure A.4: TPD spectra for $m/z = 83$ (grey), $m/z = 108$ (light red), $m/z = 127$ (black) and $m/z = 128$ (red) of (1) the 4-FTP SAM on Ag(111), (2) FePc on the 4-FTP SAM/Ag(111), (3) a higher coverage of FePc (as compared to the system in 2) on the 4-FTP SAM/Ag(111) and (4) Ru(CO)TPP on the 4-FTP SAM/Ag(111). The TPD spectra have been recorded in the temperature range of 120 - 700 K with a heating rate of $0.5\,\mathrm{K\,s^{-1}}$.

Fig. A.4 shows the TPD spectra for the various systems of Fig. 6.11a (cf. chapter 6), with addition of spectra for $m/z = 127$ and $m/z = 128$. It can be observed that the signal at $m/z = 128$ (the parent ion of the intact 4-FTP) exhibits a close similarity with the signal

at $m/z = 108$. In addition, the signal at $m/z = 127$ (ascribed to the thiolate radical or doubly ionized disulphide species) behaves very similarly to the signal at $m/z = 83$. This corroborates the assumption that mass signals $m/z = 108$ and 83 serve as distinct measure for the desorption of the thiol and the thiolate-related species (the thiolate radical or disulphide species), respectively. Considering the nature of the latter, direct desorption as thiolate radical was observed to be dominant over disulphide desorption for low density structures of hexanethiol on Au(111) [240, 241], specifically stressing the impact of molecular density, associated steric constraints [234] and molecule-substrate interaction on the actual desorption product.

A.4 Fragmentation Patterns for the Desorption of the 4-FTP SAM

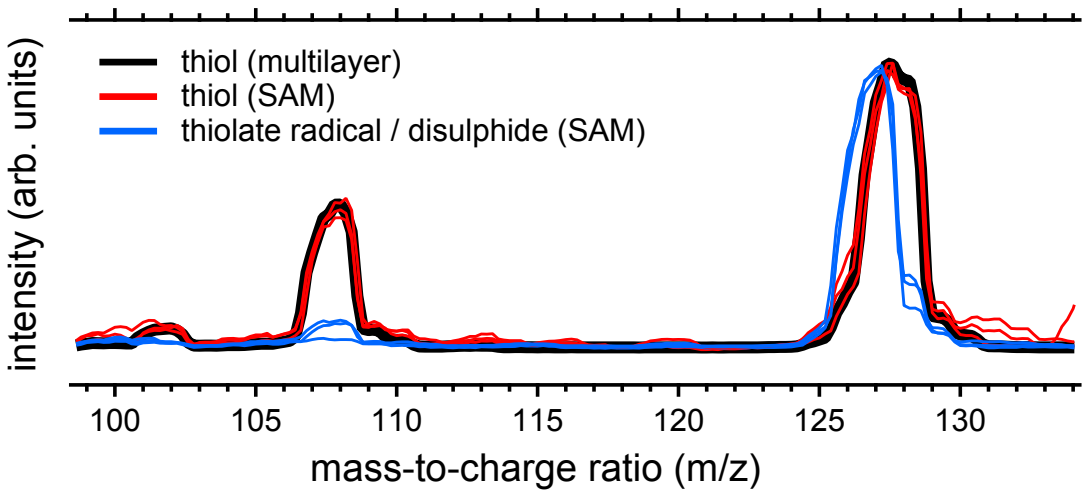

Figure A.5: TPD signals for 4-FTP SAM desorption in the range of the mass-to-charge ratios between $m/z = 99$ and $m/z = 134$: red and blue curves display the desorption signals summed over the temperature ranges that show thiol (∼550 K - 620 K) and thiolate radical/disulphide desorption (∼425 K - 535 K), respectively, while the black curve displays the fragmentation pattern for 4-FTP multilayer desorption below 200 K. Red and blue curves directly correspond to the TPD spectra in Fig. 6.11a and start with the saturated monolayer of 4-FTP as initial 4-FTP coverage. The presented spectra have been normalized to show comparable intensity for the mass-to-charge signals at $m/z = 127$ and $m/z = 128$.

As discussed in section 6.3.5, Fig. A.5 displays the TPD signals for 4-FTP SAM desorption for the mass-to-charge ratios between $m/z = 99$ and $m/z = 134$. Red and blue curves display the desorption signals summed over the temperature ranges that show

thiol (∼550 K - 620 K) and thiolate radical/disulphide desorption (∼425 K - 535 K), respectively. These spectra directly correspond to the TPD spectra in Fig. 6.11a, where the initial 4-FTP coverage is always the saturated monolayer of 4-FTP on Ag(111) (4-FTP SAM), prepared by exposing the Ag(111) surface to 4-FTP vapours at 300 K (cf. section 6.3.1). The black curve, in contrast, shows the mass pattern for 4-FTP multilayer desorption below 200 K. Importantly, the close similarity to this 4-FTP multilayer desorption pattern confirms the assumption of intact 4-FTP (thiol) desorption at elevated temperatures (red curves). Latter is reflected in the respective mass signals at $m/z = 108$ and $m/z = 128$ in both Fig. 6.11 and Fig. A.4. Furthermore, the fragmentation pattern ascribed to intact thiol desorption (red and black curves) is also clearly distinguishable from the ascribed thiolate radical/disulphide desorption (blue curves), reflected in the distinctive mass signals at $m/z = 83$ and $m/z = 127$ in Fig. 6.11 and Fig. A.4. This confirms that, in the presented study, and depending on the investigated system, the deposited 4-FTP SAM may leave the surface again as both the intact thiol and the thiolate-related species. Also note that the corresponding two fragmentation patterns in Fig. A.5 (red and blue curves) qualitatively resemble the two clearly different reference spectra of p-fluorobenzenethiol (SDBS No. 13725) and bis(3-fluorophenyl) disulphide (SDBS No. 52131) of the AIST database [41].

List of Publications

- P. S. Deimel, P. Feulner, J. V. Barth, and F. Allegretti, "Spatial decoupling of macrocyclic metal-organic complexes from a metal support: a 4-fluorothiophenol self-assembled monolayer as thermally removable spacer," *manuscript in preparation*.

- D. A. Duncan, P. S. Deimel, M. Paszkiewicz, A. Wiengarten, P. Casado Aguilar, R. G. Acres, F. Klappenberger, W. Auwärter, A. P. Seitsonen, J. V. Barth, and F. Allegretti, "Facile oxidation of titanium- to oxotitanium-porphyrins in ultra-high vacuum: the supported monolayer on Ag(111)," *manuscript in preparation*.

- M. Fritton, D. A. Duncan, P. S. Deimel, A. Rastgoo-Lahrood, F. Allegretti, J. V. Barth, W. M. Heckl, J. Björk, and M. Lackinger, "The role of kinetics *vs.* thermodynamics in surface-assisted Ullmann coupling on gold and silver surfaces," *submitted to the Journal of the American Chemical Society*, 2018.

- T. Paintner, J. Björk, P. Du, S. Klyatskaya, M. Paszkiewicz, R. Hellwig, M. Uphoff, M. A. Öner, E. Cuniberto, P. S. Deimel, Y.-Q. Zhang, C.-A. Palma, F. Allegretti, M. Ruben, J. V. Barth, and F. Klappenberger, "Interfacial ring-closure reaction mediated by proton-tunnelling transfer," *to be submitted*.

- P. S. Deimel, K. Stoiber, L. Jiang, J. A. Lloyd, S. C. Oh, S. Fischer, Ö. Sağlam, H. Schlichting, A. C. Papageorgiou, J. V. Barth, F. Allegretti, and J. Reichert, "Bisphenol A and diethylstilbestrol on Cu(111): on-surface polymerization initiated by hydroxy-directed *ortho* C-H bond activation," *The Journal of Physical Chemistry C*, vol. 123, no. 2, pp. 1354–1361, 2019.

- N. Hohn, A. E. Hetzenecker, M. A. Giebel, S. Geier, L. Bießmann, V. Körstgens, N. Saxena, J. Schlipf, W. Ohm, P. S. Deimel, F. Allegretti, J. V. Barth, S. V. Roth, T. F. Fässler, and P. Müller-Buschbaum, "Amphiphilic diblock copolymer-mediated structure control in nanoporous germanium-based thin films," *Nanoscale*, vol. 11, no. 4, pp. 2048–2055, 2019.

- M. Schwarz, M. Garnica, D. A. Duncan, A. P. Paz, J. Ducke, P. S. Deimel, P. K. Thakur, T.-L. Lee, A. Rubio, J. V. Barth, F. Allegretti, and W. Auwärter, "Adsorption conformation and lateral registry of cobalt porphine on Cu(111)," *The Journal of Physical Chemistry C*, vol. 122, no. 10, pp. 5452–5461, 2018.

- M. Schwarz, D. A. Duncan, M. Garnica, J. Ducke, P. S. Deimel, P. K. Thakur, T.-L. Lee, F. Allegretti, and W. Auwärter, "Quantitative determination of a model organic/insulator/metal interface structure," *Nanoscale*, vol. 10, no. 46, pp. 21971–21977, 2018.
- H. Aldahhak, M. Paszkiewicz, F. Allegretti, D. A. Duncan, S. Tebi, P. S. Deimel, P. Casado Aguilar, Y.-Q. Zhang, A. C. Papageorgiou, R. Koch, J. V. Barth, W. G. Schmidt, S. Müllegger, W. Schöfberger, F. Klappenberger, E. Rauls, and U. Gerstmann, "X-ray spectroscopy of thin film free-base corroles: a combined theoretical and experimental characterization," *The Journal of Physical Chemistry C*, vol. 121, no. 4, pp. 2192–2200, 2017.
- M. Schwarz, A. Riss, M. Garnica, J. Ducke, P. S. Deimel, D. A. Duncan, P. K. Thakur, T.-L. Lee, A. P. Seitsonen, J. V. Barth, F. Allegretti, and W. Auwärter, "Corrugation in the weakly interacting hexagonal-BN/Cu(111) system: structure determination by combining noncontact atomic force microscopy and X-ray standing waves," *ACS Nano*, vol. 11, no. 9, pp. 9151–9161, 2017.
- S. Tebi, M. Paszkiewicz, H. Aldahhak, F. Allegretti, S. Gonglach, M. Haas, M. Waser, P. S. Deimel, P. Casado Aguilar, Y.-Q. Zhang, A. C. Papageorgiou, D. A. Duncan, J. V. Barth, W. G. Schmidt, R. Koch, U. Gerstmann, E. Rauls, F. Klappenberger, W. Schöfberger, and S. Müllegger, "On-surface site-selective cyclization of corrole radicals," *ACS Nano*, vol. 11, no. 3, pp. 3383–3391, 2017.
- P. S. Deimel, R. M. Bababrik, B. Wang, P. J. Blowey, L. A. Rochford, P. K. Thakur, T.-L. Lee, M.-L. Bocquet, J. V. Barth, D. P. Woodruff, D. A. Duncan, and F. Allegretti, "Direct quantitative identification of the "surface trans-effect"," *Chemical Science*, vol. 7, no. 9, pp. 5647–5656, 2016.
- D. A. Duncan, J. H. K. Pfisterer, P. S. Deimel, R. G. Acres, M. Fritton, P. Feulner, J. V. Barth, and F. Allegretti, "Formation of a thermally stable bilayer of coadsorbed intact and deprotonated thymine exploiting the surface corrugation of rutile TiO_2(110)," *Physical Chemistry Chemical Physics*, vol. 18, no. 30, pp. 20433–20442, 2016.
- P. B. Weber, R. Hellwig, T. Paintner, M. Lattelais, M. Paszkiewicz, P. Casado Aguilar, P. S. Deimel, Y. Guo, Y.-Q. Zhang, F. Allegretti, A. C. Papageorgiou, J. Reichert, S. Klyatskaya, M. Ruben, J. V. Barth, M.-L. Bocquet, and F. Klappenberger, "Surface-guided formation of an organocobalt complex," *Angewandte Chemie International Edition*, vol. 55, no. 19, pp. 5754–5759, 2016.
- D. A. Duncan, P. S. Deimel, A. Wiengarten, R. Han, R. G. Acres, W. Auwärter, P. Feulner, A. C. Papageorgiou, F. Allegretti, and J. V. Barth, "Immobilised molecular catalysts and the role of the supporting metal substrate," *Chemical Communications*, vol. 51, no. 46, pp. 9483–9486, 2015.

Bibliography

[1] B. Kasemo, "Biological surface science," *Surface Science*, vol. 500, pp. 656–677, mar 2002.

[2] D. G. Castner and B. D. Ratner, "Biomedical surface science: foundations to frontiers," *Surface Science*, vol. 500, pp. 28–60, mar 2002.

[3] M. Saraste, "Oxidative phosphorylation at the *fin de siècle*," *Science*, vol. 283, pp. 1488–1493, mar 1999.

[4] M. Tirrell, E. Kokkoli, and M. Biesalski, "The role of surface science in bioengineered materials," *Surface Science*, vol. 500, pp. 61–83, mar 2002.

[5] G. A. Somorjai and Y. Li, "Impact of surface chemistry," *Proceedings of the National Academy of Sciences*, vol. 108, pp. 917–924, sep 2010.

[6] K. Qadir, S. H. Joo, B. S. Mun, D. R. Butcher, J. R. Renzas, F. Aksoy, Z. Liu, G. A. Somorjai, and J. Y. Park, "Intrinsic relation between catalytic activity of CO oxidation on Ru nanoparticles and Ru oxides uncovered with ambient pressure XPS," *Nano Letters*, vol. 12, pp. 5761–5768, oct 2012.

[7] J. Liu, F. R. Lucci, M. Yang, S. Lee, M. D. Marcinkowski, A. J. Therrien, C. T. Williams, E. C. H. Sykes, and M. Flytzani-Stephanopoulos, "Tackling CO poisoning with single-atom alloy catalysts," *Journal of the American Chemical Society*, vol. 138, pp. 6396–6399, may 2016.

[8] H.-J. Freund, "The surface science of catalysis and more, using ultrathin oxide films as templates: a perspective," *Journal of the American Chemical Society*, vol. 138, pp. 8985–8996, jul 2016.

[9] M. D. Marcinkowski, M. T. Darby, J. Liu, J. M. Wimble, F. R. Lucci, S. Lee, A. Michaelides, M. Flytzani-Stephanopoulos, M. Stamatakis, and E. C. H. Sykes, "Pt/Cu single-atom alloys as coke-resistant catalysts for efficient C–H activation," *Nature Chemistry*, vol. 10, pp. 325–332, jan 2018.

[10] F. Tao, S. Dag, L.-W. Wang, Z. Liu, D. R. Butcher, H. Bluhm, M. Salmeron, and G. A. Somorjai, "Break-up of stepped platinum catalyst surfaces by high CO coverage," *Science*, vol. 327, pp. 850–853, feb 2010.

[11] Y. Ren, K. Yuan, X. Zhou, H. Sun, K. Wu, S. L. Bernasek, W. Chen, and G. Q. Xu, "Catalytic intermediates of CO_2 hydrogenation on Cu(111) probed by in operando near-ambient pressure technique," *Chemistry - A European Journal*, vol. 24, pp. 16097–16103, oct 2018.

[12] T. J. Hurlburt, W.-C. Liu, R. Ye, and G. A. Somorjai, "Surface science approach to the molecular level integration of the principles in heterogeneous, homogeneous, and enzymatic catalysis," *Topics in Catalysis*, vol. 61, pp. 1210–1217, may 2018.

[13] A. L. Sobolewski and W. Domcke, "Photoinduced water splitting with oxotitanium porphyrin: a computational study," *Physical Chemistry Chemical Physics*, vol. 14, no. 37, pp. 12807–12817, 2012.

[14] O. Morawski, K. Izdebska, E. Karpiuk, J. Nowacki, A. Suchocki, and A. L. Sobolewski, "Photoinduced water splitting with oxotitanium tetraphenylporphyrin," *Physical Chemistry Chemical Physics*, vol. 16, no. 29, pp. 15256–15262, 2014.

[15] O. Morawski, K. Izdebska, E. Karpiuk, A. Suchocki, Y. Zhydachevskyy, and A. L. Sobolewski, "Titanyl phthalocyanine as a water photooxidation agent," *The Journal of Physical Chemistry C*, vol. 119, pp. 14085–14093, jun 2015.

[16] F. Klappenberger, R. Hellwig, P. Du, T. Paintner, M. Uphoff, L. Zhang, T. Lin, B. A. Moghanaki, M. Paszkiewicz, I. Vobornik, J. Fujii, O. Fuhr, Y.-Q. Zhang, F. Allegretti, M. Ruben, and J. V. Barth, "Functionalized graphdiyne nanowires: on-surface synthesis and assessment of band structure, flexibility, and information storage potential," *Small*, vol. 14, p. 1704321, feb 2018.

[17] P. B. Bennett, Z. Pedramrazi, A. Madani, Y.-C. Chen, D. G. de Oteyza, C. Chen, F. R. Fischer, M. F. Crommie, and J. Bokor, "Bottom-up graphene nanoribbon field-effect transistors," *Applied Physics Letters*, vol. 103, p. 253114, dec 2013.

[18] M. Ohtomo, Y. Sekine, H. Hibino, and H. Yamamoto, "Graphene nanoribbon field-effect transistors fabricated by etchant-free transfer from Au(788)," *Applied Physics Letters*, vol. 112, p. 021602, jan 2018.

[19] M. Lackinger, "Surface-assisted Ullmann coupling," *Chemical Communications*, vol. 53, no. 56, pp. 7872–7885, 2017.

[20] Q. Li, B. Yang, H. Lin, N. Aghdassi, K. Miao, J. Zhang, H. Zhang, Y. Li, S. Duhm, J. Fan, and L. Chi, "Surface-controlled mono/diselective *ortho* C–H bond activation," *Journal of the American Chemical Society*, vol. 138, pp. 2809–2814, feb 2016.

[21] K. Flechtner, A. Kretschmann, H.-P. Steinrück, and J. M. Gottfried, "NO-induced reversible switching of the electronic interaction between a porphyrin-coordinated cobalt ion and a silver surface," *Journal of the American Chemical Society*, vol. 129, pp. 12110–12111, oct 2007.

[22] W. Hieringer, K. Flechtner, A. Kretschmann, K. Seufert, W. Auwärter, J. V. Barth, A. Görling, H.-P. Steinrück, and J. M. Gottfried, "The surface trans effect: influence of axial ligands on the surface chemical bonds of adsorbed metalloporphyrins," *Journal of the American Chemical Society*, vol. 133, pp. 6206–6222, apr 2011.

[23] D. A. Duncan, P. S. Deimel, A. Wiengarten, R. Han, R. G. Acres, W. Auwärter, P. Feulner, A. C. Papageorgiou, F. Allegretti, and J. V. Barth, "Immobilised molecular catalysts and the role of the supporting metal substrate," *Chemical Communications*, vol. 51, no. 46, pp. 9483–9486, 2015.

[24] P. L. J. Gunter, J. W. Niemantsverdriet, F. H. Ribeiro, and G. A. Somorjai, "Surface science approach to modeling supported catalysts," *Catalysis Reviews*, vol. 39, pp. 77–168, feb 1997.

[25] C. R. Henry, "Surface studies of supported model catalysts," *Surface Science Reports*, vol. 31, pp. 231–325, jan 1998.

[26] A. T. Bell, "The impact of nanoscience on heterogeneous catalysis," *Science*, vol. 299, pp. 1688–1691, mar 2003.

[27] J. V. Barth, G. Costantini, and K. Kern, "Engineering atomic and molecular nanostructures at surfaces," *Nature*, vol. 437, pp. 671–679, sep 2005.

[28] K. Oura, M. Katayama, A. V. Zotov, V. G. Lifshits, and A. A. Saranin, *Surface Science*. Springer Berlin Heidelberg, 2003.

[29] H. Lüth, *Solid Surfaces, Interfaces and Thin Films*. Springer Berlin Heidelberg, 2010.

[30] A. Einstein, "Über einen die Erzeugung und Verwandlung des Lichtes betreffenden heuristischen Gesichtspunkt," *Annalen der Physik*, vol. 322, no. 6, pp. 132–148, 1905.

[31] D. McMorrow and J. Als-Nielsen, *Elements of Modern X-ray Physics*. John Wiley and Sons Ltd, 2011.

[32] S. Hüfner, *Photoelectron Spectroscopy*. Springer Berlin Heidelberg, 2010.

[33] B. D. Ratner and D. G. Castner, "Electron spectroscopy for chemical analysis," in *Surface Analysis – The Principal Techniques*, pp. 47–112, John Wiley & Sons, Ltd.

[34] J. C. Fuggle, L. M. Watson, D. J. Fabian, and S. Affrossman, "X-ray excited Auger and photoelectron spectra of magnesium, some alloys of magnesium and its oxide," *Journal of Physics F: Metal Physics*, vol. 5, pp. 375–383, feb 1975.

[35] D. A. King, "Thermal desorption from metal surfaces: a review," *Surface Science*, vol. 47, pp. 384–402, jan 1975.

[36] J. B. Miller, H. R. Siddiqui, S. M. Gates, J. N. Russell, J. T. Yates, J. C. Tully, and M. J. Cardillo, "Extraction of kinetic parameters in temperature programmed desorption: a comparison of methods," *The Journal of Chemical Physics*, vol. 87, pp. 6725–6732, dec 1987.

[37] H. Ibach, *Physics of Surfaces and Interfaces*. Springer Berlin Heidelberg, 2006.

[38] D. P. Woodruff and T. A. Delchar, *Modern Techniques of Surface Science (Cambridge Solid State Science Series)*. Cambridge University Press, 1994.

[39] A. Wiengarten, J. A. Lloyd, K. Seufert, J. Reichert, W. Auwärter, R. Han, D. A. Duncan, F. Allegretti, S. Fischer, S. C. Oh, Ö. Sağlam, L. Jiang, S. Vijayaraghavan, D. Écija, A. C. Papageorgiou, and J. V. Barth, "Surface-assisted cyclodehydrogenation; break the symmetry, enhance the selectivity," *Chemistry - A European Journal*, vol. 21, pp. 12285–12290, jul 2015.

[40] L. K. Ono and B. Roldan Cuenya, "Size effects on the desorption of O_2 from Au_2O_3/Au^0 nanoparticles supported on SiO_2: a TPD study," *The Journal of Physical Chemistry C*, vol. 112, pp. 18543–18550, nov 2008.

[41] *SDBSWeb* : https://sdbs.db.aist.go.jp (National Institute of Advanced Industrial Science and Technology (retrieved September 16, 2018).

[42] NIST Mass Spec Data Center, S. E. Stein, director, "Mass Spectra," in *NIST Chemistry WebBook, NIST Standard Reference Database Number 69* (P. J. Linstrom and W. G. Mallard, eds.), National Institute of Standards and Technology, Gaithersburg MD, 20899, doi:10.18434/T4D303 (retrieved September 16, 2018).

[43] D. P. Woodruff, B. C. C. Cowie, and A. R. H. F. Ettema, "Surface structure determination using X-ray standing waves: a simple view," *Journal of Physics: Condensed Matter*, vol. 6, pp. 10633–10645, dec 1994.

[44] D. P. Woodruff, "Surface structure determination using X-ray standing waves," *Reports on Progress in Physics*, vol. 68, pp. 743–798, mar 2005.

[45] D. P. Woodruff, D. L. Seymour, C. F. McConville, C. E. Riley, M. D. Crapper, N. P. Prince, and R. G. Jones, "A simple X-ray standing wave technique for surface

structure determination - theory and an application," *Surface Science*, vol. 195, pp. 237–254, jan 1988.

[46] S. K. M. Henze, O. Bauer, T.-L. Lee, M. Sokolowski, and F. S. Tautz, "Vertical bonding distances of PTCDA on Au(111) and Ag(111): relation to the bonding type," *Surface Science*, vol. 601, pp. 1566–1573, mar 2007.

[47] J. J. Lee, C. J. Fisher, D. P. Woodruff, M. G. Roper, R. G. Jones, and B. C. C. Cowie, "Non-dipole effects in photoelectron-monitored X-ray standing wave experiments: characterisation and calibration," *Surface Science*, vol. 494, pp. 166–182, dec 2001.

[48] M. B. Trzhaskovskaya, V. I. Nefedov, and V. G. Yarzhemsky, "Photoelectron angular distribution parameters for elements Z=1 to Z=54 in the photoelectron energy range 100–5000 eV," *Atomic Data and Nuclear Data Tables*, vol. 77, pp. 97–159, jan 2001.

[49] M. B. Trzhaskovskaya, V. I. Nefedov, and V. G. Yarzhemsky, "Photoelectron angular distribution parameters for elements Z=55 to Z=100 in the photoelectron energy range 100–5000 eV," *Atomic Data and Nuclear Data Tables*, vol. 82, pp. 257–311, nov 2002.

[50] C. Bürker, A. Franco-Cañellas, K. Broch, T.-L. Lee, A. Gerlach, and F. Schreiber, "Self-metalation of 2H-tetraphenylporphyrin on Cu(111) studied with XSW: Influence of the central metal atom on the adsorption distance," *The Journal of Physical Chemistry C*, vol. 118, pp. 13659–13666, jun 2014.

[51] D. Wechsler, M. Franke, Q. Tariq, L. Zhang, T.-L. Lee, P. K. Thakur, N. Tsud, S. Bercha, K. C. Prince, H.-P. Steinrück, and O. Lytken, "Adsorption structure of cobalt tetraphenylporphyrin on Ag(100)," *The Journal of Physical Chemistry C*, vol. 121, pp. 5667–5674, mar 2017.

[52] I. Kröger, B. Stadtmüller, C. Kleimann, P. Rajput, and C. Kumpf, "Normal-incidence X-ray standing-wave study of copper phthalocyanine submonolayers on Cu(111) and Au(111)," *Physical Review B*, vol. 83, may 2011.

[53] E. Goiri, M. Matena, A. El-Sayed, J. Lobo-Checa, P. Borghetti, C. Rogero, B. Detlefs, J. Duvernay, J. E. Ortega, and D. G. de Oteyza, "Self-assembly of bicomponent molecular monolayers: adsorption height changes and their consequences," *Physical Review Letters*, vol. 112, mar 2014.

[54] R. Romberg, S. P. Frigo, A. Ogurtsov, P. Feulner, and D. Menzel, "Photon stimulated desorption of neutral hydrogen atoms from condensed water and ammonia

by resonant O 1*s* and N 1*s* excitation: search for the signature of ultrafast bond breaking," *Surface Science*, vol. 451, pp. 116–123, apr 2000.

[55] A. Basagni, L. Ferrighi, M. Cattelan, L. Nicolas, K. Handrup, L. Vaghi, A. Papagni, F. Sedona, C. Di Valentin, S. Agnoli, and M. Sambi, "On-surface photo-dissociation of C–Br bonds: towards room temperature Ullmann coupling," *Chemical Communications*, vol. 51, no. 63, pp. 12593–12596, 2015.

[56] A. Gourdon, "On-surface covalent coupling in ultrahigh vacuum," *Angewandte Chemie International Edition*, vol. 47, pp. 6950–6953, sep 2008.

[57] J. Méndez, M. Francisca López, and J. A. Martín-Gago, "On-surface synthesis of cyclic organic molecules," *Chemical Society Reviews*, vol. 40, no. 9, p. 4578, 2011.

[58] M. E. Garah, J. M. MacLeod, and F. Rosei, "Covalently bonded networks through surface-confined polymerization," *Surface Science*, vol. 613, pp. 6–14, jul 2013.

[59] J. Björk and F. Hanke, "Towards design rules for covalent nanostructures on metal surfaces," *Chemistry - A European Journal*, vol. 20, pp. 928–934, dec 2013.

[60] M. Lackinger, "On-surface polymerization - a versatile synthetic route to two-dimensional polymers," *Polymer International*, vol. 64, pp. 1073–1078, jun 2015.

[61] L. Dong, P. N. Liu, and N. Lin, "Surface-activated coupling reactions confined on a surface," *Accounts of Chemical Research*, vol. 48, pp. 2765–2774, aug 2015.

[62] Q. Fan, J. M. Gottfried, and J. Zhu, "Surface-catalyzed C–C covalent coupling strategies toward the synthesis of low-dimensional carbon-based nanostructures," *Accounts of Chemical Research*, vol. 48, pp. 2484–2494, jul 2015.

[63] P. A. Held, H. Fuchs, and A. Studer, "Covalent-bond formation *via* on-surface chemistry," *Chemistry - A European Journal*, vol. 23, pp. 5874–5892, jan 2017.

[64] C. Steiner, J. Gebhardt, M. Ammon, Z. Yang, A. Heidenreich, N. Hammer, A. Görling, M. Kivala, and S. Maier, "Hierarchical on-surface synthesis and electronic structure of carbonyl-functionalized one- and two-dimensional covalent nanoarchitectures," *Nature Communications*, vol. 8, p. 14765, mar 2017.

[65] Z. Xiang, D. Cao, and L. Dai, "Well-defined two dimensional covalent organic polymers: rational design, controlled syntheses, and potential applications," *Polymer Chemistry*, vol. 6, no. 11, pp. 1896–1911, 2015.

[66] Q. Shen, H.-Y. Gao, and H. Fuchs, "Frontiers of on-surface synthesis: from principles to applications," *Nano Today*, vol. 13, pp. 77–96, apr 2017.

[67] L. Lafferentz, V. Eberhardt, C. Dri, C. Africh, G. Comelli, F. Esch, S. Hecht, and L. Grill, "Controlling on-surface polymerization by hierarchical and substrate-directed growth," *Nature Chemistry*, vol. 4, pp. 215–220, jan 2012.

[68] J. Eichhorn, D. Nieckarz, O. Ochs, D. Samanta, M. Schmittel, P. J. Szabelski, and M. Lackinger, "On-surface Ullmann coupling: the influence of kinetic reaction parameters on the morphology and quality of covalent networks," *ACS Nano*, vol. 8, pp. 7880–7889, jul 2014.

[69] A. Basagni, F. Sedona, C. A. Pignedoli, M. Cattelan, L. Nicolas, M. Casarin, and M. Sambi, "Molecules–oligomers–nanowires–graphene nanoribbons: a bottom-up stepwise on-surface covalent synthesis preserving long-range order," *Journal of the American Chemical Society*, vol. 137, pp. 1802–1808, jan 2015.

[70] E. A. Lewis, M. D. Marcinkowski, C. J. Murphy, M. L. Liriano, A. J. Therrien, A. Pronschinske, and E. C. H. Sykes, "Controlling selectivity in the Ullmann reaction on Cu(111)," *Chemical Communications*, vol. 53, no. 55, pp. 7816–7819, 2017.

[71] Q. Fan, C. Wang, L. Liu, Y. Han, J. Zhao, J. Zhu, J. Kuttner, G. Hilt, and J. M. Gottfried, "Covalent, organometallic, and halogen-bonded nanomeshes from tetrabromo-terphenyl by surface-assisted synthesis on Cu(111)," *The Journal of Physical Chemistry C*, vol. 118, pp. 13018–13025, jun 2014.

[72] M. D. Giovannantonio, M. Tomellini, J. Lipton-Duffin, G. Galeotti, M. Ebrahimi, A. Cossaro, A. Verdini, N. Kharche, V. Meunier, G. Vasseur, Y. Fagot-Revurat, D. F. Perepichka, F. Rosei, and G. Contini, "Mechanistic picture and kinetic analysis of surface-confined Ullmann polymerization," *Journal of the American Chemical Society*, vol. 138, pp. 16696–16702, dec 2016.

[73] N. A. A. Zwaneveld, R. Pawlak, M. Abel, D. Catalin, D. Gigmes, D. Bertin, and L. Porte, "Organized formation of 2D extended covalent organic frameworks at surfaces," *Journal of the American Chemical Society*, vol. 130, pp. 6678–6679, may 2008.

[74] C.-Z. Guan, D. Wang, and L.-J. Wan, "Construction and repair of highly ordered 2D covalent networks by chemical equilibrium regulation," *Chemical Communications*, vol. 48, no. 24, p. 2943, 2012.

[75] S. Clair, M. Abel, and L. Porte, "Growth of boronic acid based two-dimensional covalent networks on a metal surface under ultrahigh vacuum," *Chemical Communications*, vol. 50, no. 68, pp. 9627–9635, 2014.

[76] S. Weigelt, C. Busse, C. Bombis, M. M. Knudsen, K. V. Gothelf, T. Strunskus, C. Wöll, M. Dahlbom, B. Hammer, E. Lægsgaard, F. Besenbacher, and T. R.

Linderoth, "Covalent interlinking of an aldehyde and an amine on a Au(111) surface in ultrahigh vacuum," *Angewandte Chemie International Edition*, vol. 46, pp. 9227–9230, dec 2007.

[77] S. Weigelt, C. Bombis, C. Busse, M. M. Knudsen, K. V. Gothelf, E. Lægsgaard, F. Besenbacher, and T. R. Linderoth, "Molecular self-assembly from building blocks synthesized on a surface in ultrahigh vacuum: kinetic control and topo-chemical reactions," *ACS Nano*, vol. 2, pp. 651–660, mar 2008.

[78] Y. Hu, N. Goodeal, Y. Chen, A. M. Ganose, R. G. Palgrave, H. Bronstein, and M. O. Blunt, "Probing the chemical structure of monolayer covalent-organic frameworks grown *via* Schiff-base condensation reactions," *Chemical Communications*, vol. 52, no. 64, pp. 9941–9944, 2016.

[79] F. Klappenberger, Y.-Q. Zhang, J. Björk, S. Klyatskaya, M. Ruben, and J. V. Barth, "On-surface synthesis of carbon-based scaffolds and nanomaterials using terminal alkynes," *Accounts of Chemical Research*, vol. 48, pp. 2140–2150, jul 2015.

[80] D. Zhong, J.-H. Franke, S. K. Podiyanachari, T. Blomker, H. Zhang, G. Kehr, G. Erker, H. Fuchs, and L. Chi, "Linear alkane polymerization on a gold surface," *Science*, vol. 334, pp. 213–216, oct 2011.

[81] Q. Sun, C. Zhang, H. Kong, Q. Tan, and W. Xu, "On-surface aryl–aryl coupling *via* selective C–H activation," *Chemical Communications*, vol. 50, pp. 11825–11828, aug 2014.

[82] J. A. Lloyd, A. C. Papageorgiou, S. Fischer, S. C. Oh, Ö. Sağlam, K. Diller, D. A. Duncan, F. Allegretti, F. Klappenberger, M. Stöhr, R. J. Maurer, K. Reuter, J. Reichert, and J. V. Barth, "Dynamics of spatially confined bisphenol A trimers in a unimolecular network on Ag(111)," *Nano Letters*, vol. 16, pp. 1884–1889, feb 2016.

[83] S. Fischer, A. C. Papageorgiou, J. A. Lloyd, S. C. Oh, K. Diller, F. Allegretti, F. Klappenberger, A. P. Seitsonen, J. Reichert, and J. V. Barth, "Self-assembly and chemical modifications of bisphenol A on Cu(111): interplay between ordering and thermally activated stepwise deprotonation," *ACS Nano*, vol. 8, pp. 207–215, dec 2013.

[84] L. C. Alworth, K. L. Howdeshell, R. L. Ruhlen, J. K. Day, D. B. Lubahn, T. H.-M. Huang, C. L. Besch-Williford, and F. S. vom Saal, "Uterine responsiveness to estradiol and DNA methylation are altered by fetal exposure to diethylstilbestrol and methoxychlor in CD-1 mice: effects of low *versus* high doses," *Toxicology and Applied Pharmacology*, vol. 183, pp. 10–22, aug 2002.

[85] J. D. Meeker, S. Ehrlich, T. L. Toth, D. L. Wright, A. M. Calafat, A. T. Trisini, X. Ye, and R. Hauser, "Semen quality and sperm DNA damage in relation to urinary bisphenol A among men from an infertility clinic," *Reproductive Toxicology*, vol. 30, pp. 532–539, dec 2010.

[86] A. P. Tharp, M. V. Maffini, P. A. Hunt, C. A. VandeVoort, C. Sonnenschein, and A. M. Soto, "Bisphenol A alters the development of the rhesus monkey mammary gland," *Proceedings of the National Academy of Sciences*, vol. 109, pp. 8190–8195, may 2012.

[87] D. C. Dolinoy, D. Huang, and R. L. Jirtle, "Maternal nutrient supplementation counteracts bisphenol A-induced DNA hypomethylation in early development," *Proceedings of the National Academy of Sciences*, vol. 104, pp. 13056–13061, aug 2007.

[88] J. G. Bromer, Y. Zhou, M. B. Taylor, L. Doherty, and H. S. Taylor, "Bisphenol-A exposure *in utero* leads to epigenetic alterations in the developmental programming of uterine estrogen response," *The FASEB Journal*, vol. 24, pp. 2273–2280, jul 2010.

[89] A. L. Herbst, H. Ulfelder, and D. C. Poskanzer, "Adenocarcinoma of the vagina – association of maternal stilbestrol therapy with tumor appearance in young women," *New England Journal of Medicine*, vol. 284, pp. 878–881, apr 1971.

[90] J. Blatt, L. Van Le, T. Weiner, and S. Sailer, "Ovarian carcinoma in an adolescent with transgenerational exposure to diethylstilbestrol," *Journal of Pediatric Hematology/Oncology*, vol. 25, pp. 635–636, aug 2003.

[91] J. E. Cooper, E. L. Kendig, and S. M. Belcher, "Assessment of bisphenol A released from reusable plastic, aluminium and stainless steel water bottles," *Chemosphere*, vol. 85, pp. 943–947, oct 2011.

[92] I. Horcas, R. Fernández, J. M. Gómez-Rodríguez, J. Colchero, J. Gómez-Herrero, and A. M. Baro, "WSXM: a software for scanning probe microscopy and a tool for nanotechnology," *Review of Scientific Instruments*, vol. 78, p. 013705, jan 2007.

[93] M. P. Seah, "Post-1989 calibration energies for X-ray photoelectron spectrometers and the 1990 Josephson constant," *Surface and Interface Analysis*, vol. 14, pp. 488–488, aug 1989.

[94] Z. Tao, T. Wang, D. Wu, L. Feng, J. Huang, X. Wu, and J. Zhu, "Construction of molecular regular tessellations on a Cu(111) surface," *Chemical Communications*, vol. 54, no. 51, pp. 7010–7013, 2018.

[95] S. C. Oh, J. A. Lloyd, S. Fischer, Ö. Sağlam, A. C. Papageorgiou, K. Diller, D. A. Duncan, F. Klappenberger, F. Allegretti, J. Reichert, and J. V. Barth, "Isomerism

control of diethylstilbestrol by metal surface induced O–H cleavage," *Chemical Communications*, vol. 54, no. 88, pp. 12495–12498, 2018.

[96] *LEEDpat*, Version 4.2, utility by K. E. Hermann (FHI) and M. A. Van Hove (HKBU), Berlin / Hong Kong, 2014; see also http://www.fhi-berlin.mpg.de/KHsoftware/LEEDpat/index.html.

[97] F. Bebensee, K. Svane, C. Bombis, F. Masini, S. Klyatskaya, F. Besenbacher, M. Ruben, B. Hammer, and T. Linderoth, "Adsorption and dehydrogenation of tetrahydroxybenzene on Cu(111)," *Chemical Communications*, vol. 49, no. 81, pp. 9308–9310, 2013.

[98] M. J. Jackman, K. L. Syres, D. J. H. Cant, S. J. O. Hardman, and A. G. Thomas, "Adsorption of dopamine on rutile TiO2 (110): a photoemission and near-edge X-ray absorption fine structure study," *Langmuir*, vol. 30, pp. 8761–8769, jul 2014.

[99] L. Smykalla, P. Shukrynau, C. Mende, H. Lang, M. Knupfer, and M. Hietschold, "Photoelectron spectroscopy investigation of the temperature-induced deprotonation and substrate-mediated hydrogen transfer in a hydroxyphenyl-substituted porphyrin," *Chemical Physics*, vol. 450-451, pp. 39–45, apr 2015.

[100] F. Bebensee, K. Svane, C. Bombis, F. Masini, S. Klyatskaya, F. Besenbacher, M. Ruben, B. Hammer, and T. R. Linderoth, "A surface coordination network based on copper adatom trimers," *Angewandte Chemie International Edition*, vol. 53, pp. 12955–12959, sep 2014.

[101] D. Payer, A. Comisso, A. Dmitriev, T. Strunskus, N. Lin, C. Wöll, A. DeVita, J. V. Barth, and K. Kern, "Ionic hydrogen bonds controlling two-dimensional supramolecular systems at a metal surface," *Chemistry - A European Journal*, vol. 13, pp. 3900–3906, may 2007.

[102] G. Heimel, S. Duhm, I. Salzmann, A. Gerlach, A. Strozecka, J. Niederhausen, C. Bürker, T. Hosokai, I. Fernandez-Torrente, G. Schulze, S. Winkler, A. Wilke, R. Schlesinger, J. Frisch, B. Bröker, A. Vollmer, B. Detlefs, J. Pflaum, S. Kera, K. J. Franke, N. Ueno, J. I. Pascual, F. Schreiber, and N. Koch, "Charged and metallic molecular monolayers through surface-induced aromatic stabilization," *Nature Chemistry*, vol. 5, pp. 187–194, feb 2013.

[103] G. Anger, A. Winkler, and K. D. Rendulic, "Adsorption and desorption kinetics in the systems H_2/Cu(111), H_2/Cu(110) and H_2/Cu(100)," *Surface Science*, vol. 220, pp. 1–17, oct 1989.

[104] K. Stoiber and H. Schlichting, *private communication*, 2018.

[105] P. S. Deimel, K. Stoiber, L. Jiang, J. A. Lloyd, S. C. Oh, S. Fischer, Ö. Sağlam, H. Schlichting, A. C. Papageorgiou, J. V. Barth, F. Allegretti, and J. Reichert, "Bisphenol A and diethylstilbestrol on Cu(111): on-surface polymerization initiated by hydroxy-directed *ortho* C-H bond activation," *The Journal of Physical Chemistry C*, vol. 123, pp. 1354–1361, dec 2018.

[106] X. Lu, Q. Zhang, and M. C. Lin, "Adsorption of methanol, formaldehyde and formic acid on the Si(100)-2×1 surface: a computational study," *Physical Chemistry Chemical Physics*, vol. 3, no. 11, pp. 2156–2161, 2001.

[107] Y. T. Lee and J. S. Lin, "A novel theoretical study of thermally-induced reaction and vibration dynamics of methanol dissociative adsorption onto a Si(001) surface," *RSC Advances*, vol. 6, no. 2, pp. 1491–1502, 2016.

[108] Z. Chen, Y. Mao, J. Chen, H. Wang, Y. Li, and P. Hu, "Understanding the dual active sites of the FeO/Pt(111) interface and reaction kinetics: density functional theory study on methanol oxidation to formaldehyde," *ACS Catalysis*, vol. 7, pp. 4281–4290, may 2017.

[109] G. P. López, D. G. Castner, and B. D. Ratner, "XPS O 1*s* binding energies for polymers containing hydroxyl, ether, ketone and ester groups," *Surface and Interface Analysis*, vol. 17, pp. 267–272, may 1991.

[110] S. J. Kerber, J. J. Bruckner, K. Wozniak, S. Seal, S. Hardcastle, and T. L. Barr, "The nature of hydrogen in X-ray photoelectron spectroscopy: general patterns from hydroxides to hydrogen bonding," *Journal of Vacuum Science & Technology A: Vacuum, Surfaces, and Films*, vol. 14, pp. 1314–1320, may 1996.

[111] R. J. Behm, K. Christmann, G. Ertl, and M. A. Van Hove, "Adsorption of CO on Pd(100)," *The Journal of Chemical Physics*, vol. 73, pp. 2984–2995, sep 1980.

[112] R. J. Purtell, R. P. Merrill, C. W. Seabury, and T. N. Rhodin, "Molecular adsorbate structures from angular-resolved photoemission: ammonia on Ir(111)," *Physical Review Letters*, vol. 44, pp. 1279–1281, may 1980.

[113] S. Bao, Ph. Hofmann, K.-M. Schindler, V. Fritzsche, A. M. Bradshaw, D. P. Woodruff, C. Casado, and M. C. Asensio, "Following the changes in local geometry associated with a surface reaction: the dehydrogenation of adsorbed ethylene," *Journal of Physics: Condensed Matter*, vol. 6, pp. L93–L98, feb 1994.

[114] K.-M. Schindler, V. Fritzsche, M. C. Asensio, P. Gardner, D. E. Ricken, A. W. Robinson, A. M. Bradshaw, D. P. Woodruff, J. C. Conesa, and A. R. González-Elipe, "Structural determination of a molecular adsorbate by photoelectron diffraction: ammonia on Ni{111}," *Physical Review B*, vol. 46, pp. 4836–4843, aug 1992.

[115] J. D. Batteas, A. Barbieri, E. K. Starkey, M. A. Van Hove, and G. A. Somorjai, "A tensor LEED analysis of the Rh(110)-p2mg(2 × 1)-2CO structure," *Surface Science*, vol. 313, pp. 341–348, jul 1994.

[116] G. Held and D. Menzel, "The structure of the p($\sqrt{3}$ × $\sqrt{3}$)R30° bilayer of D_2O on Ru(001)," *Surface Science*, vol. 316, pp. 92–102, sep 1994.

[117] Y. J. Kim, S. Thevuthasan, G. S. Herman, C. H. F. Peden, S. A. Chambers, D. N. Belton, and H. Permana, "Chemisorption geometry of NO on Rh(111) by X-ray photoelectron diffraction," *Surface Science*, vol. 359, pp. 269–279, jul 1996.

[118] E. Lundgren, X. Torrelles, J. Alvarez, S. Ferrer, H. Over, A. Beutler, and J. N. Andersen, "Surface X-ray-diffraction study of the Rh(111)+(2 × 2)-3CO structure," *Physical Review B*, vol. 59, pp. 5876–5880, feb 1999.

[119] D. I. Sayago, J. T. Hoeft, M. Polcik, M. Kittel, R. L. Toomes, J. Robinson, D. P. Woodruff, M. Pascal, C. L. A. Lamont, and G. Nisbet, "Bond lengths and bond strengths in weak and strong chemisorption: N_2, CO, and CO/H on nickel surfaces," *Physical Review Letters*, vol. 90, mar 2003.

[120] M. R. Albert and J. T. Yates, *The Surface Scientist's Guide to Organometallic Chemistry*. Washington, DC, USA: American Chemical Society, 1987.

[121] M. K. Bradley, D. Kreikemeyer Lorenzo, W. Unterberger, D. A. Duncan, T. J. Lerotholi, J. Robinson, and D. P. Woodruff, "Methoxy species on Cu(110): understanding the local structure of a key catalytic reaction intermediate," *Physical Review Letters*, vol. 105, aug 2010.

[122] D. Kreikemeyer-Lorenzo, W. Unterberger, D. A. Duncan, M. K. Bradley, T. J. Lerotholi, J. Robinson, and D. P. Woodruff, "Face-dependent bond lengths in molecular chemisorption: the formate species on cu(111) and cu(110)," *Physical Review Letters*, vol. 107, jul 2011.

[123] Z. V. Zheleva, T. Eralp, and G. Held, "Complete experimental structure determination of the p(3 × 2)pg phase of glycine on Cu{110}," *The Journal of Physical Chemistry C*, vol. 116, pp. 618–625, dec 2011.

[124] D. P. Woodruff, "The structure of surfaces: what do we know and what would we like to know?," *Journal of Physics: Condensed Matter*, vol. 22, p. 084016, feb 2010.

[125] C. Copéret, M. Chabanas, R. Petroff Saint-Arroman, and J.-M. Basset, "Homogeneous and heterogeneous catalysis: bridging the gap through surface organometallic chemistry," *Angewandte Chemie International Edition*, vol. 42, pp. 156–181, jan 2003.

[126] E. Palomares, M. V. Martínez-Díaz, S. A. Haque, T. Torres, and J. R. Durrant, "State selective electron injection in non-aggregated titanium phthalocyanine sensitised nanocrystalline TiO_2 films," *Chemical Communications*, no. 18, pp. 2112–2113, 2004.

[127] C. A. Bortolotti, L. Paltrinieri, S. Monari, A. Ranieri, M. Borsari, G. Battistuzzi, and M. Sola, "A surface-immobilized cytochrome c variant provides a pH-controlled molecular switch," *Chemical Science*, vol. 3, no. 3, pp. 807–810, 2012.

[128] W. Auwärter, D. Écija, F. Klappenberger, and J. V. Barth, "Porphyrins at interfaces," *Nature Chemistry*, vol. 7, pp. 105–120, feb 2015.

[129] J. M. Gottfried, "Surface chemistry of porphyrins and phthalocyanines," *Surface Science Reports*, vol. 70, pp. 259–379, nov 2015.

[130] B. Hulsken, R. V. Hameren, J. W. Gerritsen, T. Khoury, P. Thordarson, M. J. Crossley, A. E. Rowan, R. J. M. Nolte, J. A. A. W. Elemans, and S. Speller, "Real-time single-molecule imaging of oxidation catalysis at a liquid–solid interface," *Nature Nanotechnology*, vol. 2, pp. 285–289, apr 2007.

[131] B. E. Murphy, S. A. Krasnikov, N. N. Sergeeva, A. A. Cafolla, A. B. Preobrajenski, A. N. Chaika, O. Lübben, and I. V. Shvets, "Homolytic cleavage of molecular oxygen by manganese porphyrins supported on Ag(111)," *ACS Nano*, vol. 8, pp. 5190–5198, apr 2014.

[132] C. Wäckerlin, D. Chylarecka, A. Kleibert, K. Müller, C. Iacovita, F. Nolting, T. A. Jung, and N. Ballav, "Controlling spins in adsorbed molecules by a chemical switch," *Nature Communications*, vol. 1, pp. 1–7, aug 2010.

[133] N. Ballav, C. Wäckerlin, D. Siewert, P. M. Oppeneer, and T. A. Jung, "Emergence of on-surface magnetochemistry," *The Journal of Physical Chemistry Letters*, vol. 4, pp. 2303–2311, jun 2013.

[134] O. P. H. Vaughan, F. J. Williams, N. Bampos, and R. M. Lambert, "A chemically switchable molecular pinwheel," *Angewandte Chemie International Edition*, vol. 45, pp. 3779–3781, jun 2006.

[135] W. J. Cho, Y. Cho, S. K. Min, W. Y. Kim, and K. S. Kim, "Chromium porphyrin arrays as spintronic devices," *Journal of the American Chemical Society*, vol. 133, pp. 9364–9369, jun 2011.

[136] D. B. Dougherty, A. Sandin, E. Vescovo, and J. E. Rowe, "Coverage-dependent surface magnetism of iron phthalocyanine on an O-Fe(110) surface," *Physical Review B*, vol. 90, p. 045406, jul 2014.

[137] F. I. Bohrer, A. Sharoni, C. Colesniuc, J. Park, I. K. Schuller, A. C. Kummel, and W. C. Trogler, "Gas sensing mechanism in chemiresistive cobalt and metal-free phthalocyanine thin films," *Journal of the American Chemical Society*, vol. 129, pp. 5640–5646, may 2007.

[138] K. Seufert, W. Auwärter, and J. V. Barth, "Discriminative response of surface-confined metalloporphyrin molecules to carbon and nitrogen monoxide," *Journal of the American Chemical Society*, vol. 132, pp. 18141–18146, dec 2010.

[139] F. Sedona, M. D. Marino, D. Forrer, A. Vittadini, M. Casarin, A. Cossaro, L. Floreano, A. Verdini, and M. Sambi, "Tuning the catalytic activity of Ag(110)-supported Fe phthalocyanine in the oxygen reduction reaction," *Nature Materials*, vol. 11, pp. 970–977, oct 2012.

[140] A. Michaelides, K. Reuter, and M. Scheffler, "When seeing is not believing: oxygen on Ag(111), a simple adsorption system?," *Journal of Vacuum Science & Technology A: Vacuum, Surfaces, and Films*, vol. 23, pp. 1487–1497, nov 2005.

[141] J. Schnadt, A. Michaelides, J. Knudsen, R. T. Vang, K. Reuter, E. Lægsgaard, M. Scheffler, and F. Besenbacher, "Revisiting the structure of the p(4×4) surface oxide on Ag(111)," *Physical Review Letters*, vol. 96, apr 2006.

[142] H. Grönbeck and M. Odelius, "Photoemission core-level shifts reveal the thiolate-Au(111) interface," *Physical Review B*, vol. 82, aug 2010.

[143] G. Mercurio, E. R. McNellis, I. Martin, S. Hagen, F. Leyssner, S. Soubatch, J. Meyer, M. Wolf, P. Tegeder, F. S. Tautz, and K. Reuter, "Structure and energetics of azobenzene on Ag(111): benchmarking semiempirical dispersion correction approaches," *Physical Review Letters*, vol. 104, jan 2010.

[144] F. R. Hartley, "The *cis*- and *trans*-effects of ligands," *Chemical Society Reviews*, vol. 2, no. 2, p. 163, 1973.

[145] B. Pinter, V. Van Speybroeck, M. Waroquier, P. Geerlings, and F. De Proft, "trans effect and trans influence: importance of metal mediated ligand–ligand repulsion," *Physical Chemistry Chemical Physics*, vol. 15, no. 40, p. 17354, 2013.

[146] B. J. Coe and S. J. Glenwright, "Trans-effects in octahedral transition metal complexes," *Coordination Chemistry Reviews*, vol. 203, pp. 5–80, jun 2000.

[147] J. Qiao, Y. Liu, F. Hong, and J. Zhang, "A review of catalysts for the electroreduction of carbon dioxide to produce low-carbon fuels," *Chemical Society Reviews*, vol. 43, no. 2, pp. 631–675, 2014.

[148] D. den Boer, M. Li, T. Habets, P. Iavicoli, A. E. Rowan, R. J. M. Nolte, S. Speller, D. B. Amabilino, S. De Feyter, and J. A. A. W. Elemans, "Detection of different oxidation states of individual manganese porphyrins during their reaction with oxygen at a solid/liquid interface," *Nature Chemistry*, vol. 5, pp. 621–627, jun 2013.

[149] R. Gutzler, S. Stepanow, D. Grumelli, M. Lingenfelder, and K. Kern, "Mimicking enzymatic active sites on surfaces for energy conversion chemistry," *Accounts of Chemical Research*, vol. 48, pp. 2132–2139, jun 2015.

[150] T. G. Gopakumar, F. Matino, H. Naggert, A. Bannwarth, F. Tuczek, and R. Berndt, "Electron-induced spin crossover of single molecules in a bilayer on gold," *Angewandte Chemie International Edition*, vol. 51, pp. 6262–6266, may 2012.

[151] S. Jiang, R. Cheng, X. Wang, T. Xue, Y. Liu, A. Nel, Y. Huang, and X. Duan, "Real-time electrical detection of nitric oxide in biological systems with sub-nanomolar sensitivity," *Nature Communications*, vol. 4, jul 2013.

[152] L. Floreano, A. Cossaro, R. Gotter, A. Verdini, G. Bavdek, F. Evangelista, A. Ruocco, A. Morgante, and D. Cvetko, "Periodic arrays of Cu-phthalocyanine chains on Au(110)," *The Journal of Physical Chemistry C*, vol. 112, pp. 10794–10802, jun 2008.

[153] W. Auwärter, K. Seufert, F. Klappenberger, J. Reichert, A. Weber-Bargioni, A. Verdini, D. Cvetko, M. Dell'Angela, L. Floreano, A. Cossaro, G. Bavdek, A. Morgante, A. P. Seitsonen, and J. V. Barth, "Site-specific electronic and geometric interface structure of Co-tetraphenyl-porphyrin layers on Ag(111)," *Physical Review B*, vol. 81, jun 2010.

[154] C. Wäckerlin, K. Tarafder, D. Siewert, J. Girovsky, T. Hählen, C. Iacovita, A. Kleibert, F. Nolting, T. A. Jung, P. M. Oppeneer, and N. Ballav, "On-surface coordination chemistry of planar molecular spin systems: novel magnetochemical effects induced by axial ligands," *Chemical Science*, vol. 3, no. 11, p. 3154, 2012.

[155] C. Isvoranu, B. Wang, E. Ataman, K. Schulte, J. Knudsen, J. N. Andersen, M.-L. Bocquet, and J. Schnadt, "Ammonia adsorption on iron phthalocyanine on Au(111): influence on adsorbate–substrate coupling and molecular spin," *The Journal of Chemical Physics*, vol. 134, p. 114710, mar 2011.

[156] C. J. Fisher, R. Ithin, R. G. Jones, G. J. Jackson, D. P. Woodruff, and B. C. C. Cowie, "Non-dipole photoemission effects in X-ray standing wavefield determination of surface structure," *Journal of Physics: Condensed Matter*, vol. 10, pp. L623–L629, sep 1998.

[157] L. A. Rochford, D. S. Keeble, O. J. Holmes, G. J. Clarkson, and T. S. Jones, "Controlling templating effects at the organic/inorganic interface using (111) oriented copper iodide," *Journal of Materials Chemistry C*, vol. 2, no. 30, pp. 6056–6060, 2014.

[158] S. C. Bobaru, E. Salomon, J.-M. Layet, and T. Angot, "Structural properties of iron phtalocyanines on Ag(111): from the submonolayer to monolayer range," *The Journal of Physical Chemistry C*, vol. 115, pp. 5875–5879, mar 2011.

[159] N. Papageorgiou, Y. Ferro, E. Salomon, A. Allouche, J. M. Layet, L. Giovanelli, and G. Le Lay, "Geometry and electronic structure of lead phthalocyanine: quantum calculations *via* density-functional theory and photoemission measurements," *Physical Review B*, vol. 68, p. 235105, dec 2003.

[160] A. L. Schwaner, E. D. Pylant, and J. M. White, "Electron-induced surface chemistry: synthesis of NH_x fragments on Ag(111)," *Journal of Vacuum Science & Technology A: Vacuum, Surfaces, and Films*, vol. 14, pp. 1453–1456, may 1996.

[161] G. Kresse and J. Furthmüller, "Efficient iterative schemes for *ab initio* total-energy calculations using a plane-wave basis set," *Physical Review B*, vol. 54, pp. 11169–11186, oct 1996.

[162] J. P. Perdew, K. Burke, and M. Ernzerhof, "Generalized gradient approximation made simple," *Physical Review Letters*, vol. 77, pp. 3865–3868, oct 1996.

[163] P. E. Blöchl, "Projector augmented-wave method," *Physical Review B*, vol. 50, pp. 17953–17979, dec 1994.

[164] G. Kresse and D. Joubert, "From ultrasoft pseudopotentials to the projector augmented-wave method," *Physical Review B*, vol. 59, pp. 1758–1775, jan 1999.

[165] S. Grimme, J. Antony, S. Ehrlich, and H. Krieg, "A consistent and accurate *ab initio* parametrization of density functional dispersion correction (DFT-D) for the 94 elements H-Pu," *The Journal of Chemical Physics*, vol. 132, p. 154104, apr 2010.

[166] S. Grimme, S. Ehrlich, and L. Goerigk, "Effect of the damping function in dispersion corrected density functional theory," *Journal of Computational Chemistry*, vol. 32, pp. 1456–1465, mar 2011.

[167] J. Klimeš, D. R. Bowler, and A. Michaelides, "Chemical accuracy for the van der Waals density functional," *Journal of Physics: Condensed Matter*, vol. 22, p. 022201, dec 2009.

[168] J. Klimeš, D. R. Bowler, and A. Michaelides, "Van der Waals density functionals applied to solids," *Physical Review B*, vol. 83, may 2011.

[169] J. V. Barth, "Fresh perspectives for surface coordination chemistry," *Surface Science*, vol. 603, pp. 1533–1541, jun 2009.

[170] U. Schlickum, R. Decker, F. Klappenberger, G. Zoppellaro, S. Klyatskaya, M. Ruben, I. Silanes, A. Arnau, K. Kern, H. Brune, and J. V. Barth, "Metal-organic honeycomb nanomeshes with tunable cavity size," *Nano Letters*, vol. 7, pp. 3813–3817, dec 2007.

[171] A. P. Seitsonen, M. Lingenfelder, H. Spillmann, A. Dmitriev, S. Stepanow, N. Lin, K. Kern, and J. V. Barth, "Density functional theory analysis of carboxylate-bridged diiron units in two-dimensional metal-organic grids," *Journal of the American Chemical Society*, vol. 128, pp. 5634–5635, may 2006.

[172] J. Shen, R. Kortlever, R. Kas, Y. Y. Birdja, O. Diaz-Morales, Y. Kwon, I. Ledezma-Yanez, K. J. P. Schouten, G. Mul, and M. T. M. Koper, "Electrocatalytic reduction of carbon dioxide to carbon monoxide and methane at an immobilized cobalt protoporphyrin," *Nature Communications*, vol. 6, sep 2015.

[173] K. Diller, A. C. Papageorgiou, F. Klappenberger, F. Allegretti, J. V. Barth, and W. Auwärter, "*In vacuo* interfacial tetrapyrrole metallation," *Chemical Society Reviews*, vol. 45, no. 6, pp. 1629–1656, 2016.

[174] C. Isvoranu, B. Wang, E. Ataman, J. Knudsen, K. Schulte, J. N. Andersen, M.-L. Bocquet, and J. Schnadt, "Comparison of the carbonyl and nitrosyl complexes formed by adsorption of CO and NO on monolayers of iron phthalocyanine on Au(111)," *The Journal of Physical Chemistry C*, vol. 115, pp. 24718–24727, nov 2011.

[175] C. Wäckerlin, D. Siewert, T. A. Jung, and N. Ballav, "On-surface coordination chemistry: direct imaging of the conformational freedom of an axial ligand at room temperature," *Physical Chemistry Chemical Physics*, vol. 15, no. 39, pp. 16510–16514, 2013.

[176] T. Lukasczyk, K. Flechtner, L. R. Merte, N. Jux, F. Maier, J. M. Gottfried, and H.-P. Steinrück, "Interaction of cobalt(II) tetraarylporphyrins with a Ag(111) surface studied with photoelectron spectroscopy," *The Journal of Physical Chemistry C*, vol. 111, pp. 3090–3098, feb 2007.

[177] F. Bischoff, K. Seufert, W. Auwärter, S. Joshi, S. Vijayaraghavan, D. Écija, K. Diller, A. C. Papageorgiou, S. Fischer, F. Allegretti, D. A. Duncan, F. Klappenberger, F. Blobner, R. Han, and J. V. Barth, "How surface bonding and repulsive interactions cause phase transformations: ordering of a prototype macrocyclic compound on Ag(111)," *ACS Nano*, vol. 7, pp. 3139–3149, mar 2013.

[178] K. Diller, F. Klappenberger, F. Allegretti, A. C. Papageorgiou, S. Fischer, A. Wiengarten, S. Joshi, K. Seufert, D. Écija, W. Auwärter, and J. V. Barth, "Investigating the molecule-substrate interaction of prototypic tetrapyrrole compounds: adsorption and self-metalation of porphine on Cu(111)," *The Journal of Chemical Physics*, vol. 138, p. 154710, apr 2013.

[179] I. Kröger, B. Stadtmüller, and C. Kumpf, "Submonolayer and multilayer growth of titaniumoxide-phthalocyanine on Ag(111)," *New Journal of Physics*, vol. 18, p. 113022, nov 2016.

[180] K. Schönauer, S. Weiss, V. Feyer, D. Lüftner, B. Stadtmüller, D. Schwarz, T. Sueyoshi, C. Kumpf, P. Puschnig, M. G. Ramsey, F. S. Tautz, and S. Soubatch, "Charge transfer and symmetry reduction at the CuPc/Ag(110) interface studied by photoemission tomography," *Physical Review B*, vol. 94, p. 205144, nov 2016.

[181] G. A. Somorjai and J. Y. Park, "Molecular factors of catalytic selectivity," *Angewandte Chemie International Edition*, vol. 47, pp. 9212–9228, nov 2008.

[182] E. Gross, J. H.-C. Liu, F. D. Toste, and G. A. Somorjai, "Control of selectivity in heterogeneous catalysis by tuning nanoparticle properties and reactor residence time," *Nature Chemistry*, vol. 4, pp. 947–952, sep 2012.

[183] J. C. Love, L. A. Estroff, J. K. Kriebel, R. G. Nuzzo, and G. M. Whitesides, "Self-assembled monolayers of thiolates on metals as a form of nanotechnology," *Chemical Reviews*, vol. 105, pp. 1103–1170, apr 2005.

[184] M. Halik, H. Klauk, U. Zschieschang, G. Schmid, C. Dehm, M. Schütz, S. Maisch, F. Effenberger, M. Brunnbauer, and F. Stellacci, "Low-voltage organic transistors with an amorphous molecular gate dielectric," *Nature*, vol. 431, pp. 963–966, oct 2004.

[185] L.-W. Chong, Y.-L. Lee, T.-C. Wen, and T.-F. Guo, "Self-assembled monolayer-modified Ag anode for top-emitting polymer light-emitting diodes," *Applied Physics Letters*, vol. 89, p. 233513, dec 2006.

[186] L. Y. Yang, X. Z. Chen, H. Xu, D. Q. Ye, H. Tian, and S. G. Yin, "Surface modification of indium tin oxide anode with self-assembled monolayer modified Ag film for improved OLED device characteristics," *Applied Surface Science*, vol. 254, pp. 5055–5060, jun 2008.

[187] J.-P. Hong, A.-Y. Park, S. Lee, J. Kang, N. Shin, and D. Y. Yoon, "Tuning of Ag work functions by self-assembled monolayers of aromatic thiols for an efficient hole injection for solution processed triisopropylsilylethynyl pentacene organic thin film transistors," *Applied Physics Letters*, vol. 92, p. 143311, apr 2008.

[188] N. Padma, S. Sen, S. N. Sawant, and R. Tokas, "A study on threshold voltage stability of low operating voltage organic thin-film transistors," *Journal of Physics D: Applied Physics*, vol. 46, p. 325104, jul 2013.

[189] Y. Xie, S. Cai, Q. Shi, S. Ouyang, W.-Y. Lee, Z. Bao, J. R. Matthews, R. A. Bellman, M. He, and H. H. Fong, "High performance organic thin film transistors using chemically modified bottom contacts and dielectric surfaces," *Organic Electronics*, vol. 15, pp. 2073–2078, sep 2014.

[190] P. Maheshwari, S. Mukherjee, D. Bhattacharya, S. Sen, R. B. Tokas, Y. Honda, S. Basu, N. Padma, and P. K. Pujari, "Probing molecular packing at engineered interfaces in organic field effect transistor and its correlation with charge carrier mobility," *ACS Applied Materials & Interfaces*, vol. 7, pp. 10169–10177, may 2015.

[191] S. Casalini, C. A. Bortolotti, F. Leonardi, and F. Biscarini, "Self-assembled monolayers in organic electronics," *Chemical Society Reviews*, vol. 46, no. 1, pp. 40–71, 2017.

[192] D. Liu and Q. Miao, "Recent progress in interface engineering of organic thin film transistors with self-assembled monolayers," *Materials Chemistry Frontiers*, vol. 2, no. 1, pp. 11–21, 2018.

[193] H. Yamada, H. Imahori, Y. Nishimura, I. Yamazaki, T. K. Ahn, S. K. Kim, D. Kim, and S. Fukuzumi, "Photovoltaic properties of self-assembled monolayers of porphyrins and porphyrin-fullerene dyads on ITO and gold surfaces," *Journal of the American Chemical Society*, vol. 125, pp. 9129–9139, jul 2003.

[194] Y.-J. Cho, T. K. Ahn, H. Song, K. S. Kim, C. Y. Lee, W. S. Seo, K. Lee, S. K. Kim, D. Kim, and J. T. Park, "Unusually high performance photovoltaic cell based on a [60]fullerene metal cluster-porphyrin dyad SAM on an ITO electrode," *Journal of the American Chemical Society*, vol. 127, pp. 2380–2381, mar 2005.

[195] Th. Wink, S. J. van Zuilen, A. Bult, and W. P. van Bennekom, "Self-assembled monolayers for biosensors," *The Analyst*, vol. 122, no. 4, pp. 43R–50R, 1997.

[196] D. G. Wu, D. Cahen, P. Graf, R. Naaman, A. Nitzan, and D. Shvarts, "Direct detection of low-concentration NO in physiological solutions by a new GaAs-based sensor," *Chemistry – A European Journal*, vol. 7, pp. 1743–1749, apr 2001.

[197] W. Senaratne, L. Andruzzi, and C. K. Ober, "Self-assembled monolayers and polymer brushes in biotechnology: current applications and future perspectives," *Biomacromolecules*, vol. 6, pp. 2427–2448, sep 2005.

[198] X.-L. Zhang, L.-G. Chen, P. Lv, H.-Y. Gao, S.-J. Wei, Z.-C. Dong, and J. G. Hou, "Fluorescence decay of quasimonolayered porphyrins near a metal surface separated by short-chain alkanethiols," *Applied Physics Letters*, vol. 92, p. 223118, jun 2008.

[199] D. A. Offord, S. B. Sachs, M. S. Ennis, T. A. Eberspacher, J. H. Griffin, C. E. D. Chidsey, and J. P. Collman, "Synthesis and properties of metalloporphyrin monolayers and stacked multilayers bound to an electrode *via* site specific axial ligation to a self-assembled monolayer," *Journal of the American Chemical Society*, vol. 120, pp. 4478–4487, may 1998.

[200] F. Da Cruz, K. Driaf, C. Berthier, J.-M. Lameille, and F. Armand, "Study of a self-assembled porphyrin monomolecular layer obtained by metal complexation," *Thin Solid Films*, vol. 349, pp. 155–161, jul 1999.

[201] Z. Zhang, S. Hou, Z. Zhu, and Z. Liu, "Preparation and characterization of a porphyrin self-assembled monolayer with a controlled orientation on gold," *Langmuir*, vol. 16, pp. 537–540, jan 2000.

[202] Z. Zhang, R. Hu, and Z. Liu, "Formation of a porphyrin monolayer film by axial ligation of protoporphyrin IX zinc to an amino-terminated silanized glass surface," *Langmuir*, vol. 16, pp. 1158–1162, feb 2000.

[203] G. Kalyuzhny, A. Vaskevich, G. Ashkenasy, A. Shanzer, and I. Rubinstein, "UV/Vis spectroscopy of metalloporphyrin and metallophthalocyanine monolayers self-assembled on ultrathin gold films," *The Journal of Physical Chemistry B*, vol. 104, pp. 8238–8244, aug 2000.

[204] Z. Zhang, T. Imae, H. Sato, A. Watanabe, and Y. Ozaki, "Surface-enhanced raman scattering and surface-enhanced infrared absorption spectroscopic studies of a metalloporphyrin monolayer film formed on pyridine self-assembled monolayer-modified gold," *Langmuir*, vol. 17, pp. 4564–4568, jul 2001.

[205] D. Li, L. W. Moore, and B. I. Swanson, "Formation of metal clusters on the surfaces of covalently bound self-assembled ligand monolayers," *Langmuir*, vol. 10, pp. 1177–1185, apr 1994.

[206] A. V. Naumkin, A. Kraut-Vass, S. W. Gaarenstroom, and C. J. Powell, *NIST X-ray Photoelectron Spectroscopy Database, NIST Standard Reference Database Number 20, Version 4.1.* National Institute of Standards and Technology, Gaithersburg MD, 20899 (2000), doi:10.18434/T4T88K, (retrieved in October 2018).

[207] D. L. Adams and J. N. Andersen, *FitXPS Version 2.12.* Institute of Physics and Astronomy, University of Aarhus, DK-8000 Aarhus C, Denmark, 2001.

[208] M. Himmelhaus, I. Gauss, M. Buck, F. Eisert, Ch. Wöll, and M. Grunze, "Adsorption of docosanethiol from solution on polycrystalline silver surfaces: an XPS and NEXAFS study," *Journal of Electron Spectroscopy and Related Phenomena*, vol. 92, pp. 139–149, may 1998.

[209] T. Laiho, J. A. Leiro, M. H. Heinonen, S. S. Mattila, and J. Lukkari, "Photoelectron spectroscopy study of irradiation damage and metal–sulfur bonds of thiol on silver and copper surfaces," *Journal of Electron Spectroscopy and Related Phenomena*, vol. 142, pp. 105–112, feb 2005.

[210] K. Heister, M. Zharnikov, M. Grunze, and L. S. O. Johansson, "Adsorption of alkanethiols and biphenylthiols on Au and Ag substrates: a high-resolution X-ray photoelectron spectroscopy study," *The Journal of Physical Chemistry B*, vol. 105, pp. 4058–4061, may 2001.

[211] F. Bensebaa, Y. Zhou, Y. Deslandes, E. Kruus, and T. H. Ellis, "XPS study of metal–sulfur bonds in metal–alkanethiolate materials," *Surface Science*, vol. 405, pp. L472–L476, 1998.

[212] G. Xue, M. Ma, J. Zhang, Y. Lu, and K. T. Carron, "SERS and XPS studies of the molecular orientation of thiophenols from the gaseous state onto silver," *Journal of Colloid and Interface Science*, vol. 150, pp. 1–6, apr 1992.

[213] F. Blobner, P. N. Abufager, R. Han, J. Bauer, D. A. Duncan, R. J. Maurer, K. Reuter, P. Feulner, and F. Allegretti, "Thiolate-bonded self-assembled monolayers on Ni(111): bonding strength, structure, and stability," *The Journal of Physical Chemistry C*, vol. 119, pp. 15455–15468, jun 2015.

[214] C. Kodama, T. Hayashi, and H. Nozoye, "Decomposition of alkanethiols adsorbed on Au(111) at low temperature," *Applied Surface Science*, vol. 169-170, pp. 264–267, jan 2001.

[215] C. Kim, J. H. Sim, X.-M. Yan, and J. M. White, "Thermal reactions of 2-naphthalenethiol adsorbed on Ag(111)," *Langmuir*, vol. 18, pp. 3159–3166, apr 2002.

[216] K. L. Wong, X. Lin, K.-Y. Kwon, G. Pawin, B. V. Rao, A. Liu, L. Bartels, S. Stolbov, and T. S. Rahman, "Halogen-substituted thiophenol molecules on Cu(111)," *Langmuir*, vol. 20, pp. 10928–10934, dec 2004.

[217] P. Jiang, K. Deng, D. Fichou, S.-S. Xie, A. Nion, and C. Wang, "STM imaging *ortho*- and *para*-fluorothiophenol self-assembled monolayers on Au(111)," *Langmuir*, vol. 25, pp. 5012–5017, may 2009.

[218] C. Schmidt, A. Witt, and G. Witte, "Tailoring the Cu(100) work function by substituted benzenethiolate self-assembled monolayers," *The Journal of Physical Chemistry A*, vol. 115, pp. 7234–7241, jun 2011.

[219] J. Y. Gui, D. A. Stern, D. G. Frank, F. Lu, D. C. Zapien, and A. T. Hubbard, "Adsorption and surface structural chemistry of thiophenol, benzyl mercaptan, and alkyl mercaptans. Comparative studies at Ag(111) and Pt(111) electrodes by means of Auger spectroscopy, electron energy loss spectroscopy, low-energy electron diffraction and electrochemistry," *Langmuir*, vol. 7, pp. 955–963, may 1991.

[220] M. Yu, D. P. Woodruff, C. J. Satterley, R. G. Jones, and V. R. Dhanak, "Structural investigation of the interaction of molecular sulfur with Ag(111)," *The Journal of Physical Chemistry C*, vol. 111, pp. 3152–3162, jan 2007.

[221] M. Yu, D. P. Woodruff, N. Bovet, C. J. Satterley, K. Lovelock, R. G. Jones, and V. Dhanak, "Structure investigation of Ag(111)($\sqrt{7} \times \sqrt{7}$)R19°-SCH_3 by X-ray standing waves: a case of thiol-induced substrate reconstruction," *The Journal of Physical Chemistry B*, vol. 110, pp. 2164–2170, feb 2006.

[222] M. Yu, D. P. Woodruff, C. J. Satterley, R. G. Jones, and V. R. Dhanak, "Structure of the pentylthiolate self-assembled monolayer on Ag(111)," *The Journal of Physical Chemistry C*, vol. 111, pp. 10040–10048, jul 2007.

[223] I. Kröger, B. Stadtmüller, C. Stadler, J. Ziroff, M. Kochler, A. Stahl, F. Pollinger, T.-L. Lee, J. Zegenhagen, F. Reinert, and C. Kumpf, "Submonolayer growth of copper-phthalocyanine on Ag(111)," *New Journal of Physics*, vol. 12, p. 083038, aug 2010.

[224] Y. Bai, F. Buchner, M. T. Wendahl, I. Kellner, A. Bayer, H.-P. Steinrück, H. Marbach, and J. M. Gottfried, "Direct metalation of a phthalocyanine monolayer on Ag(111) with coadsorbed iron atoms," *The Journal of Physical Chemistry C*, vol. 112, pp. 6087–6092, apr 2008.

[225] M. Schmid, J. Zirzlmeier, H.-P. Steinrück, and J. M. Gottfried, "Interfacial interactions of iron(II) tetrapyrrole complexes on Au(111)," *The Journal of Physical Chemistry C*, vol. 115, pp. 17028–17035, aug 2011.

[226] L. Massimi, M. Angelucci, P. Gargiani, M. G. Betti, S. Montoro, and C. Mariani, "Metal-phthalocyanine ordered layers on Au(110): metal-dependent adsorption energy," *The Journal of Chemical Physics*, vol. 140, p. 244704, jun 2014.

[227] H. Peisert, M. Knupfer, T. Schwieger, J. M. Auerhammer, M. S. Golden, and J. Fink, "Full characterization of the interface between the organic semiconductor copper

phthalocyanine and gold," *Journal of Applied Physics*, vol. 91, pp. 4872–4878, apr 2002.

[228] H. Peisert, D. Kolacyak, and T. Chassé, "Site-specific charge-transfer screening at organic/metal interfaces," *The Journal of Physical Chemistry C*, vol. 113, pp. 19244–19250, oct 2009.

[229] A. C. Papageorgiou, S. Fischer, S. C. Oh, Ö. Sağlam, J. Reichert, A. Wiengarten, K. Seufert, S. Vijayaraghavan, D. Écija, W. Auwärter, F. Allegretti, R. G. Acres, K. C. Prince, K. Diller, F. Klappenberger, and J. V. Barth, "Self-terminating protocol for an interfacial complexation reaction *in vacuo* by metal-organic chemical vapor deposition," *ACS Nano*, vol. 7, pp. 4520–4526, may 2013.

[230] A. C. Papageorgiou, K. Diller, S. Fischer, F. Allegretti, F. Klappenberger, S. C. Oh, Ö. Sağlam, J. Reichert, A. Wiengarten, K. Seufert, W. Auwärter, and J. V. Barth, "*In vacuo* porphyrin metalation on Ag(111) *via* chemical vapor deposition of $Ru_3(CO)_{12}$: mechanistic insights," *The Journal of Physical Chemistry C*, vol. 120, pp. 8751–8758, apr 2016.

[231] M. Weston, T. J. Reade, A. J. Britton, K. Handrup, N. R. Champness, and J. N. O'Shea, "A single centre water splitting dye complex adsorbed on rutile TiO_2(110): photoemission, X-ray absorption, and optical spectroscopy," *The Journal of Chemical Physics*, vol. 135, p. 114703, sep 2011.

[232] A. Weber-Bargioni, W. Auwärter, F. Klappenberger, J. Reichert, S. Lefrançois, T. Strunskus, C. Wöll, A. Schiffrin, Y. Pennec, and J. V. Barth, "Visualizing the frontier orbitals of a conformationally adapted metalloporphyrin," *ChemPhysChem*, vol. 9, pp. 89–94, jan 2008.

[233] E. Ito, H. Ito, H. Kang, T. Hayashi, M. Hara, and J. Noh, "Influence of surface morphology and substrate on thermal stability and desorption behavior of octanethiol self-assembled monolayers: Cu, Ag, and Au," *The Journal of Physical Chemistry C*, vol. 116, pp. 17586–17593, aug 2012.

[234] T. Hayashi, K. Wakamatsu, E. Ito, and M. Hara, "Effect of steric hindrance on desorption processes of alkanethiols on Au(111)," *The Journal of Physical Chemistry C*, vol. 113, pp. 18795–18799, sep 2009.

[235] G. E. Poirier, "Butanethiol self-assembly on Au(001): the 1×4 Au missing row, c(2×8) molecular lattice," *Journal of Vacuum Science & Technology B: Microelectronics and Nanometer Structures Processing, Measurement, and Phenomena*, vol. 14, pp. 1453–1460, mar 1996.

[236] X.-L. Zhou, J. M. White, and B. E. Koel, "Chemisorption of atomic hydrogen on clean and Cl-covered Ag(111)," *Surface Science*, vol. 218, pp. 201–210, aug 1989.

[237] G. Lee, P. T. Sprunger, M. Okada, D. B. Poker, D. M. Zehner, and E. W. Plummer, "Chemisorption of hydrogen on the Ag(111) surface," *Journal of Vacuum Science & Technology A: Vacuum, Surfaces, and Films*, vol. 12, pp. 2119–2123, jul 1994.

[238] G. Lee and E. W. Plummer, "Interaction of hydrogen with the Ag(111) surface," *Physical Review B*, vol. 51, pp. 7250–7261, mar 1995.

[239] J. L. Lin and B. E. Bent, "Formation of methyl radicals during the oxidative addition of iodomethane to a single-crystal copper surface," *Journal of the American Chemical Society*, vol. 115, pp. 2849–2853, apr 1993.

[240] H. Kondoh, C. Kodama, and H. Nozoye, "Structure-dependent change of desorption species from n-alkanethiol monolayers adsorbed on Au(111): desorption of thiolate radicals from low-density structures," *The Journal of Physical Chemistry B*, vol. 102, pp. 2310–2312, mar 1998.

[241] H. Kondoh, C. Kodama, H. Sumida, and H. Nozoye, "Molecular processes of adsorption and desorption of alkanethiol monolayers on Au(111)," *The Journal of Chemical Physics*, vol. 111, pp. 1175–1184, jul 1999.

[242] D. Zerulla and T. Chassé, "X-ray induced damage of self-assembled alkanethiols on gold and indium phosphide," *Langmuir*, vol. 15, pp. 5285–5294, aug 1999.

[243] A. Gölzhäuser, S. Panov, and Ch. Wöll, "Determination of molecular orientation in ultrathin films of aminophenylthiolate on Cu(100) prepared by vapour phase deposition," *Surface Science*, vol. 314, pp. L849–L856, jul 1994.

[244] S. Karthe, R. Szargan, and E. Suoninen, "Oxidation of pyrite surfaces: a photoelectron spectroscopic study," *Applied Surface Science*, vol. 72, pp. 157–170, oct 1993.

[245] J. Repp, G. Meyer, S. M. Stojković, A. Gourdon, and C. Joachim, "Molecules on insulating films: scanning-tunneling microscopy imaging of individual molecular orbitals," *Physical Review Letters*, vol. 94, p. 026803, jan 2005.

[246] L. Gross, F. Mohn, N. Moll, P. Liljeroth, and G. Meyer, "The chemical structure of a molecule resolved by atomic force microscopy," *Science*, vol. 325, pp. 1110–1114, aug 2009.

[247] C. Wäckerlin, F. Donati, A. Singha, R. Baltic, S. Rusponi, K. Diller, F. Patthey, M. Pivetta, Y. Lan, S. Klyatskaya, M. Ruben, H. Brune, and J. Dreiser, "Giant hysteresis of single-molecule magnets adsorbed on a nonmagnetic insulator," *Advanced Materials*, vol. 28, pp. 5195–5199, may 2016.

[248] P. Erler, P. Schmitt, N. Barth, A. Irmler, S. Bouvron, T. Huhn, U. Groth, F. Pauly, L. Gragnaniello, and M. Fonin, "Highly ordered surface self-assembly of Fe_4 single molecule magnets," *Nano Letters*, vol. 15, pp. 4546–4552, jun 2015.

[249] S. Joshi, F. Bischoff, R. Koitz, D. Écija, K. Seufert, A. P. Seitsonen, J. Hutter, K. Diller, J. I. Urgel, H. Sachdev, J. V. Barth, and W. Auwärter, "Control of molecular organization and energy level alignment by an electronically nanopatterned boron nitride template," *ACS Nano*, vol. 8, pp. 430–442, dec 2013.

[250] M. Schwarz, D. A. Duncan, M. Garnica, J. Ducke, P. S. Deimel, P. K. Thakur, T.-L. Lee, F. Allegretti, and W. Auwärter, "Quantitative determination of a model organic/insulator/metal interface structure," *Nanoscale*, vol. 10, no. 46, pp. 21971–21977, 2018.

[251] V. C. Zoldan, R. Faccio, C. Gao, and A. A. Pasa, "Coupling of cobalt–tetraphenylporphyrin molecules to a copper nitride layer," *The Journal of Physical Chemistry C*, vol. 117, pp. 15984–15990, jul 2013.

[252] X. Yang, I. Krieger, D. Lüftner, S. Weiß, T. Heepenstrick, M. Hollerer, P. Hurdax, G. Koller, M. Sokolowski, P. Puschnig, M. G. Ramsey, F. S. Tautz, and S. Soubatch, "On the decoupling of molecules at metal surfaces," *Chemical Communications*, vol. 54, no. 65, pp. 9039–9042, 2018.

[253] Q. Wang, A. Franco-Cañellas, P. Ji, C. Bürker, R.-B. Wang, K. Broch, P. K. Thakur, T.-L. Lee, H. Zhang, A. Gerlach, L. Chi, S. Duhm, and F. Schreiber, "Bilayer formation *vs* molecular exchange in organic heterostructures: strong impact of subtle changes in molecular structure," *The Journal of Physical Chemistry C*, vol. 122, pp. 9480–9490, apr 2018.

[254] A. L. Linsebigler, G. Lu, and J. T. Yates, "Photocatalysis on TiO_2 surfaces: principles, mechanisms, and selected results," *Chemical Reviews*, vol. 95, pp. 735–758, may 1995.

[255] F. Haag, "Spectroscopic study of on–surface reactions on model metal and metal oxide surfaces," Master's thesis, Technical University of Munich, Department of Physics, 2017.

[256] S. R. Hatch, X.-Y. Zhu, J. M. White, and A. Campion, "Surface photochemistry 15: on the role of substrate excitation," *The Journal of Chemical Physics*, vol. 92, pp. 2681–2682, feb 1990.

[257] V. A. Ukraintsev, T. J. Long, T. Gowl, and I. Harrison, "Photoinduced dissociative electron attachment of CH_3Br on Pt(111): the role of the local work function," *The Journal of Chemical Physics*, vol. 96, pp. 9114–9121, jun 1992.

[258] St. J. Dixon-Warren, E. T. Jensen, and J. C. Polanyi, "Photochemistry of adsorbed molecules. XI. Charge-transfer photodissociation and photoreaction in chloromethanes on Ag(111)," *The Journal of Chemical Physics*, vol. 98, pp. 5938–5953, apr 1993.

[259] J. Lee, S. Ryu, J. S. Ku, and S. K. Kim, "Charge transfer photodissociation of phenol on Ag(111)," *The Journal of Chemical Physics*, vol. 115, no. 22, pp. 10518–10524, 2001.

[260] J. Lee, S. Ryu, J. Chang, S. Kim, and S. K. Kim, "Direct observation of an intermediate state for a surface photochemical reaction initiated by hot electron transfer," *The Journal of Physical Chemistry B*, vol. 109, no. 30, pp. 14481–14485, 2005.

[261] P. Avouris and B. N. J. Persson, "Excited states at metal surfaces and their nonradiative relaxation," *The Journal of Physical Chemistry*, vol. 88, pp. 837–848, mar 1984.

[262] R. Gutzler, L. Cardenas, J. Lipton-Duffin, M. E. Garah, L. E. Dinca, C. E. Szakacs, C. Fu, M. Gallagher, M. Vondráček, M. Rybachuk, D. F. Perepichka, and F. Rosei, "Ullmann-type coupling of brominated tetrathienoanthracene on copper and silver," *Nanoscale*, vol. 6, no. 5, pp. 2660–2668, 2014.

[263] J. Eichhorn, T. Strunskus, A. Rastgoo-Lahrood, D. Samanta, M. Schmittel, and M. Lackinger, "On-surface Ullmann polymerization *via* intermediate organometallic networks on Ag(111)," *Chemical Communications*, vol. 50, no. 57, pp. 7680–7682, 2014.

[264] Y.-J. Wu, W.-H. Wang, and C.-M. Chiang, "Identification of surface allenyl and its transformation into propargyl with C_3H_3Br adsorption by RAIRS on Ag(111)," *Langmuir*, vol. 18, pp. 1449–1452, mar 2002.

[265] M. Zharnikov, W. Geyer, A. Gölzhäuser, S. Frey, and M. Grunze, "Modification of alkanethiolate monolayers on Au-substrate by low energy electron irradiation: alkyl chains and the S/Au interface," *Physical Chemistry Chemical Physics*, vol. 1, no. 13, pp. 3163–3171, 1999.

[266] K. Heister, M. Zharnikov, M. Grunze, L. S. O. Johansson, and A. Ulman, "Characterization of X-ray induced damage in alkanethiolate monolayers by high-resolution photoelectron spectroscopy," *Langmuir*, vol. 17, pp. 8–11, jan 2001.

[267] U. Diebold and T. E. Madey, "TiO_2 by XPS," *Surface Science Spectra*, vol. 4, pp. 227–231, jul 1996.

[268] T. L. Thompson and J. T. Yates, "Surface science studies of the photoactivation of TiO_2 – new photochemical processes," *Chemical Reviews*, vol. 106, pp. 4428–4453, oct 2006.

[269] T. J. Lerotholi, E. A. Kröger, M. J. Knight, W. Unterberger, K. Hogan, D. C. Jackson, C. L. A. Lamont, and D. P. Woodruff, "Adsorption structure of glycine on TiO_2(110): a photoelectron diffraction determination," *Surface Science*, vol. 603, pp. 2305–2311, aug 2009.

[270] U. Diebold, "The surface science of titanium dioxide," *Surface Science Reports*, vol. 48, pp. 53–229, jan 2003.

[271] F. Allegretti, J. P. W. Treacy, and R. Lindsay, "Visibility of TiO_2(110)(1×1) bridging oxygen in core level photoelectron spectroscopy," *Physical Review B*, vol. 85, p. 205422, may 2012.

[272] R. A. Bennett, S. Poulston, P. Stone, and M. Bowker, "STM and LEED observations of the surface structure of TiO_2(110) following crystallographic shear plane formation," *Physical Review B*, vol. 59, pp. 10341–10346, apr 1999.

[273] J. N. Wilson, R. M. Dowler, and H. Idriss, "Adsorption and reaction of glycine on the rutile TiO_2(011) single crystal surface," *Surface Science*, vol. 605, pp. 206–213, jan 2011.

Acknowledgements

I have to thank a lot of people for their extraordinary support, their encouragement and their contributions to this work. Without their help, the presented doctoral thesis would not have been possible! I deeply enjoyed working together with all of them and in the following lines they are gratefully acknowledged.

Firstly, I would like to greatly thank my doctoral advisor Prof. Dr. Johannes Barth who gave me the opportunity to perform my thesis at his chair. I deeply enjoyed the past years of doing science at E20. Secondly, I would like to thank Dr. Francesco Allegretti for his professional guidance, assistance, supervision and help in all aspects of science and everyday academic life. He is largely responsible for my education as a surface scientist. Specifically I have to thank him for repeatedly revising, correcting and improving all my drafts, specifically this doctoral thesis. Thirdly, I would like to thank Prof. Dr. Peter Feulner for his extraordinary help and his scientific and experimental guidance. The utilized UHV chamber (on campus) and a substantial part of the applied measurement devices were designed and constructed by him. As just one example, both the underlying electronics of the applied bolometer and the electronics that allowed to record the presented 2D-TPD spectra were his design. Furthermore, he provided great support for the concept, design and realization of the LED-based re-entrant light source. But most importantly, if you had questions, or a problem to be solved, his door was always open. I also want to thank David Duncan, who, together with Francesco Allegretti, introduced me to the field of surface science. I have to thank him for all his help, advice and guidance, and for having a lot of pleasant and successful beamtimes.

I especially want to thank Felix Haag and Johannes Küchle for their extraordinary help in the lab. It was always a great pleasure and fun to work with them. Notably, I have to thank Felix for helping me with a lot of experiments and especially for his contributions to the presented measurements on glycine adsorbed on TiO_2 and BTPA on Ag(111). In this regard, I also have to thank Guillaume Médard for providing the 6-bromo-N-(p-tolyl)pyridin-2-amine (BTPA).

Furthermore, I have to thank all the people involved in and contributing to the work on the "Direct quantitative identification of the "surface *trans*-effect"", specifically Reda M. Bababrik, Bin Wang and Marie-Laure Bocquet for doing the theoretical calculations and making the corresponding images. I also want to thank the staff of the I09 beamline at the Diamond Light Source, in particular, for the help provided by Tien-Lin Lee, Pardeep

Kumar Thakur and Dave McCue.

I also need to thank all the people involved in and contributing to the work on "Bisphenol A and Diethylstilbestrol on Cu(111): on-surface polymerization initiated by hydroxy-directed *ortho* C-H bond activation". Especially I have to thank Li Jiang, Julian A. Lloyd, Seung Cheol Oh, Sybille Fischer, Özge Sağlam, Anthoula C. Papageorgiou and Joachim Reichert for the STM investigations. Moreover, I have to thank Karolina Stoiber and Hartmut Schlichting for the quantitative analysis of the temperature programmed desorption data.

I also want to thank Luke Rochford for purifying and providing the iron phthalocyanine powder utilized throughout the presented investigations.

Special thanks go to the staff of our chair, setting the stage and being the basis of our work! I like to thank Karl Eberle for all his technical help and advice, for repairing broken evaporators, defective pumps and, especially, for always providing a helping hand. I want to thank Reinhold Schneider for the repair, the construction, installation and the assembly of the required electronic devices, the repair of vacuum pumps and for taking care of the safety and functioning of all our electronic devices. He also soldered the wires on the applied LEDs. It also deserves special acknowledgement that Karl Eberle and Reinhold Schneider always repaired the things we broke. Furthermore, I want to thank Viktoria Blaschek for the support and help in all administrative manners and, especially, for organizing the various E20 activities like the E20-retreats, hikes, Christmas parties, etc. I also have to thank Max Glanz, specifically, for taking care of our safety and for providing us computers and software to record and analyze our data. Moreover, I want to thank all the people from the workshop of the physics department for realizing our drafts.

I also want to thank the whole E20 team and my office colleagues for the pleasant and familiar working atmosphere, for exciting discussions and the great time I had.

Finally, I have to thank my family for their never ending support and encouragement over the past few years of my studies and, in particular, my wife, for accompanying me "through thick and thin" and for always being there for me.